GENERATION OF SHORT AND INTENSE ATTOSECOND PULSES

by

SABIH UD DIN KHAN

B.Sc., University of Engineering and Technology Lahore, 2002
M.S., Pakistan Institute of Engineering and Applied Science, 2004

AN ABSTRACT OF A DISSERTATION

submitted in partial fulfillment of the requirements for the degree

DOCTOR OF PHILOSOPHY

Department of Physics
College of Arts & Sciences

KANSAS STATE UNIVERSITY
Manhattan, Kansas

2012

Abstract

Extremely broad bandwidth attosecond pulses (which can support 16as pulses) have been demonstrated in our lab based on spectral measurements, however, compensation of intrinsic chirp and their characterization has been a major bottleneck. In this work, we developed an attosecond streak camera using a multi-layer Mo/Si mirror (bandwidth can support ~100as pulses) and position sensitive time-of-flight detector, and the shortest measured pulse was 107.5as using DOG, which is close to the mirror bandwidth. We also developed a PCGPA based FROG-CRAB algorithm to characterize such short pulses, however, it uses the central momentum approximation and cannot be used for ultra-broad bandwidth pulses. To facilitate the characterization of such pulses, we developed PROOF using Fourier filtering and an evolutionary algorithm. We have demonstrated the characterization of pulses with a bandwidth corresponding to ~20as using synthetic data. We also for the first time demonstrated single attosecond pulses (SAP) generated using GDOG with a narrow gate width from a multi-cycle driving laser without CE-phase lock, which opens the possibility of scaling attosecond photon flux by extending the technique to peta-watt class lasers.

Further, we generated intense attosecond pulse trains (APT) from laser ablated carbon plasmas and demonstrated ~9.5 times more intense pulses as compared to those from argon gas and for the first time demonstrated a broad continuum from a carbon plasma using DOG.

Additionally, we demonstrated ~100 times enhancement in APT from gases by switching to 400 nm (blue) driving pulses instead of 800 nm (red) pulses. We measured the ellipticity dependence of high harmonics from blue pulses in argon, neon and helium, and developed a simple theoretical model to numerically calculate the ellipticity dependence with good agreement with experiments. Based on the ellipticity dependence, we proposed a new scheme of blue GDOG which we predict can be employed to extract intense SAP from an APT driven by blue laser pulses. We also demonstrated compression of long blue pulses into >240 μJ broad-bandwidth pulses using neon filled hollow core fiber, which is the highest reported pulse energy of short blue pulses. However, compression of phase using chirp mirrors is still a technical challenge.

GENERATION OF SHORT AND INTENSE ATTOSECOND PULSES

by

SABIH UD DIN KHAN

B.Sc., University of Engineering and Technology Lahore, 2002
M.S., Pakistan Institute of Engineering and Applied Science, 2004

A DISSERTATION

submitted in partial fulfillment of the requirements for the degree

DOCTOR OF PHILOSOPHY

Department of Physics
College of Arts and Sciences

KANSAS STATE UNIVERSITY
Manhattan, Kansas

2012

Approved by:

Co-major Professor
Zenghu Chang

Approved by:

Co-major Professor
Brett D. DePaola

Abstract

Extremely broad bandwidth attosecond pulses (which can support 16as pulses) have been demonstrated in our lab based on spectral measurements, however, compensation of intrinsic chirp and their characterization has been a major bottleneck. In this work, we developed an attosecond streak camera using a multi-layer Mo/Si mirror (bandwidth can support ~100as pulses) and position sensitive time-of-flight detector, and the shortest measured pulse was 107.5as using DOG, which is close to the mirror bandwidth. We also developed a PCGPA based FROG-CRAB algorithm to characterize such short pulses, however, it uses the central momentum approximation and cannot be used for ultra-broad bandwidth pulses. To facilitate the characterization of such pulses, we developed PROOF using Fourier filtering and an evolutionary algorithm. We have demonstrated the characterization of pulses with a bandwidth corresponding to ~20as using synthetic data. We also for the first time demonstrated single attosecond pulses (SAP) generated using GDOG with a narrow gate width from a multi-cycle driving laser without CE-phase lock, which opens the possibility of scaling attosecond photon flux by extending the technique to peta-watt class lasers.

Further, we generated intense attosecond pulse trains (APT) from laser ablated carbon plasmas and demonstrated ~9.5 times more intense pulses as compared to those from argon gas and for the first time demonstrated a broad continuum from a carbon plasma using DOG.

Additionally, we demonstrated ~100 times enhancement in APT from gases by switching to 400 nm (blue) driving pulses instead of 800 nm (red) pulses. We measured the ellipticity dependence of high harmonics from blue pulses in argon, neon and helium, and developed a simple theoretical model to numerically calculate the ellipticity dependence with good agreement with experiments. Based on the ellipticity dependence, we proposed a new scheme of blue GDOG which we predict can be employed to extract intense SAP from an APT driven by blue laser pulses. We also demonstrated compression of long blue pulses into >240 μJ broad-bandwidth pulses using neon filled hollow core fiber, which is the highest reported pulse energy of short blue pulses. However, compression of phase using chirp mirrors is still a technical challenge.

Table of Contents

List of Figures

List of Tables

Acknowledgements

I would like to acknowledge my supervisor and mentor Prof. Chang for his efforts to bring out the best in me. During last five years I disturbed him at all the odd hours and always found him leaving his work and responding to my queries. He guided me through rough times and I am indebted to him for all his efforts.

I would also like to acknowledge cooperation and efforts of my supervisory committee members including Caterina Scoglio (committee chair), Brett DePaola (co-supervisor), Kevin Carnes and Shuting Lei. I am thankful to Brett with whom my interaction started in my first semester and he has mentored me in many things both in professional and private life. I am also thankful to Kevin Carnes, who is an authority in SpecTcl, the computer code we use for attosecond streak camera. He guided me through many issues, and the operation of the streak camera would not have been possible without him. I am also thankful for Shuting Lei, who is also our PI for MURI project and is an exceptional leader and I thoroughly enjoyed working under his leadership.

I feel really lucky to have worked with several gifted post-docs, including Chenquang Li, Hiroki Mashiko, Ximao Feng, Shouyuan Chen, Kun Zhao and Baozhen Zhao. For the attosecond streak camera I spend most of my time working with Ximao Feng and learned a lot from him. For DOG/GDOG I worked with Hiroki Mashiko, and I learnt MARS laser maintenance and operation from Shouyuan Chen. In the last two years, I had the pleasure of working with Kun Zhao and Baozhen Zhao for 400 nm driven harmonics. Kun Zhao is a very gifted scientist and an excellent manager. With his leadership we were able to survive in Kansas when Prof. Chang and the rest of the team moved to Florida. And I owe a lot to Baozhen from whom I learned a lot about lasers. During last six months the MARS laser died several times and we almost lost hope but thanks to Baozhen's efforts and creative ideas we were able to fix it and currently it is running without issues.

I was fortunate to have exceptionally cooperative and professional fellow students in our group. Wang He convinced me to join this group and have learned a lot from him. For the attosecond streak camera I mostly worked with Steve Gilbertson and have always found him one step ahead of everybody. He is a very energetic and hard working person and a very good friend. Yi Wu and Mike Chini joined the lab at exactly the same time as I did and I had a great time with

them. I am thankful to Yi for his help and guidance in the operation of KLS laser system. I worked with Wang He and Mike Chini for attosecond reconstruction algorithms and with our team effort we were able to develop FROG-CRAB and PROOF and I am very thankful for their efforts and cooperation. I am proud to have collaborated with Zhang Qi and Kun Zhao while developing Magnetic Bottle based attosecond streak camera with which they recently measured 77as single attosecond pulse. During my last two years, I worked with Yan Cheng on 400nm driven harmonics and had an exceptional experience with him and would like to thank him for all the efforts and wish him good luck for his future research in Florida.

I am thankful to Tsuneyuki Ozaki and his team at ALLS, INRS, Montreal, Canada including Yoann Pertot and Luc Elouga Bom, for many helpful discussions and our two experimental campaigns during 2010 and 2011. I hope our collaboration on high harmonics from laser ablated carbon plasmas continues in the future. I found them very cooperative and professional.

I am also thankful to Max Moller from Institut für Optik und Quantenelektronik, Friedrich-Schiller-Universität, Jena, Germany, a visiting student from Gerhard Paulus group for helping us with the semi-classical theory for the ellipticity dependence of high harmonics.

I would also like to acknowledge efforts of Kevin Carnes and his extra ordinary team of technicians, who worked hard to turn our ideas into reality. I work the majority of my time with Al Rankin for almost all the projects and without him my research would not have been possible. I am also thankful to Vince Needham for his help in computing and software issues. He saved our beamtime from getting wasted many times by fixing IT issues in time. I am also thankful to Mike Wells for his help in Vacuum technology. Many times he went out of the way to make things work for me. I am also thankful to Scott Chaney for his help with electronics and going out of the way to help me in my research. I am also thankful to Russ Reynolds and Bryan Merritt for their help in machining. Russ is an excellent teacher and I have learned a lot from him in operating various machines in the machine shop. I am also thankful to Bob Krause for his help and cooperation in many issues within JRM Lab.

In the end, I would like to thank my wife and son for their cooperation and understanding, as without their cooperation it was not possible to spend many nights and odd hours in the lab doing experiments.

Dedication

Dedicated to Abu Ali al-Hasan ibn al-Hasan ibn al-Haytham (Alhazen, born 965 A.D. Basra) for laying the foundation of modern optics by introducing the ray tracing technique for reflection and refraction.

Chapter 1 - Generation of attosecond pulses

Introduction

Pump-probe is a powerful spectroscopic technique in atomic and molecular physics that can study extremely fast temporal events using a relatively slower detector. The idea is motivated from a conventional photographic camera, in which an event in time (for example when we pose for the camera) is probed by the light coming from the flash of the camera and imaged by the photographic film or an image sensor like CCD, CMOS, etc. In the pump-probe technique, an atomic or molecular transition is initiated by a pump pulse and allowed to evolve. After some time a probe pulse is sent to extract some information (like the spectrum of the emitted electrons) about the evolved state of the system. The resolution of the pump-probe method is determined by the FWHM of both the pump and probe pulses. In 1999, the Nobel prize in chemistry was awarded to Ahmed Zewail for employing this pump-probe technique using femtosecond duration laser pulses to study vibrations and rotations in molecules and study chemical reactions with the highest resolution possible [1], which led to the exciting field of femto-chemistry. The pump-probe technique was later extended to the attosecond regime by employing attosecond pulse trains from high harmonic generation as the pump and driving femtosecond pulses as the probe. However, due to the train of attosecond pulses, many starting points of the transition led to poor resolution and limited utilization. In 2001, with the demonstration of single isolated attosecond pulses by Ferenc Krausz and his team [2], and later by Nisoli [3] and Chang's team [4, 5], the pump-probe technique entered the realm of attosecond science. However, to date the highest reported photon flux of attosecond pulses is still limited to a few nJ [6,7], which is not enough to split the pulses and use them for attosecond pump-attosecond probe experiments, which is currently the holy grail of attosecond science. Consequently, current experiments are limited to attosecond pump-femtosecond probe, which are used to study electron dynamics within atoms and molecules. In the last few years, our group has been successful in setting up a number of experimental setups involving the attosecond pump-femtosecond probe technique using electron time-of-flight [4, 5, 8, 9], velocity-map-imaging and transient absorption [10,11] detectors and studied a number of atomic processes with the highest achieved time resolution [12 , 11]. However, we aim to eventually evolve this research into

attosecond pump-attosecond probe experiments. In this thesis, we give an overview of our efforts to achieve shorter (107.5 as pulses with attosecond streak camera) and more intense attosecond pulses. Based on our experiences from this work our team has been able to setup an MBEES (Magnetic bottle electron emission spectrometer) based attosecond streak camera which measured 77 as pulses [9](according to Guinness Book of World Records the shortest attosecond pulse is 80 as [13]). Our main focus in this thesis, however, is the generation of more intense attosecond pulses, which can not only be used in attosecond pump-attosecond probe experiments but also be used to demonstrate non-linear attosecond processes.

In the first two chapters of this thesis, an overview of high harmonic generation and gating techniques to extract single attosecond pulses is given. In the end of the second chapter, we discuss our efforts to increase the photon flux of attosecond pulse trains by ~9.5 times by generating high harmonics in laser-ablated carbon plasmas instead of noble gases. We also discuss the first demonstration of broad-continuum from high harmonics in carbon plasmas by optical gating, which hints at the extraction of single attosecond pulses. In the third chapter, we focus on our efforts to develop an attosecond streak camera and the algorithms FROG-CRAB and PROOF to retrieve single attosecond pulses from traces obtained from the attosecond streak camera. Additionally, in the end of the third chapter we discuss an experiment which demonstrated for the first time that single attosecond pulses can be produced with multi-cycle pulses without carrier-envelope phase lock. These are powerful results as they open the possibility of using such a technique on peta-watt class lasers and achieving higher photon flux. Based on these findings our group is developing a 10 Hz, 100-200 mJ laser at the University of Central Florida in an attempt to generate micro-joule level attosecond pulses.

In the fourth chapter, we explore yet another method to scale up attosecond photon flux by switching from 800 nm to 400 nm. We demonstrate an increase of 2 orders of magnitude in the photon flux of attosecond pulse trains and have made the first experimental measurement of the ellipticity dependence of 400 nm pulses, which is a critical parameter to design optical gating techniques to extract single attosecond pulses from a pulse train. In the fifth chapter, we summarize our efforts to compress 55 fs, 400 nm pulses into sub-10 fs pulses using self phase modulation in a hollow core fiber and demonstrate the highest reported energy of ~250 μJ after the fiber. We also discuss our design of self-diffraction FROG to characterize such pulses and issues with phase compensation, which is still a technical challenge. In Chapter 6, we propose a

new optical gating technique for 400 nm based on our measurement of the ellipticity dependence, which we term blue GDOG. However, due to the non-availability of phase compensated, intense, sub-10 fs pulses, we could not experimentally demonstrate the technique.

3-step model & high harmonics generation

High harmonic generation is an important non-linear process. When a laser with intensity $<10^{12}$ W/cm^2 is focused in a gas medium high order harmonics of the laser frequency are observed, but intensity of each order rapidly decreases with increasing order. This is termed perturbative high harmonic generation. Only odd harmonics are observed due to the centro-symmetric potential of the gas atoms. In 1987-88 [14, 15] it was observed that at an intensity of 10^{14} W/cm^2, harmonic intensity rapidly decreases for the first few harmonic orders, but a plateau is observed up to tens or even hundreds of orders, and then rapidly decreases at a point termed the cutoff. This is termed non-perturbative high harmonic generation [15].

The plateau and cutoff can be explained by a semi-classical model proposed by Corkum [16] in 1993, called the 3-step model. At high enough intensities of around 10^{14} W/cm^2, the laser field at the peaks is comparable to the atomic Coulomb potential and is modified into a potential barrier due to the superposition of the laser field and the Coulomb potential. Consequently, near the field maxima electron can tunnel out from this barrier into the continuum, which is the first step (tunneling). The freed electron moves classically in the laser field governed by Newton's equations (second step, acceleration) and returns back when the laser field flips direction. In the third step (re-collision), the returning electron may re-collide with the parent atom, emitting any excess energy which it gained in the laser field during its return as packets of photons. Interestingly, the packets of photons are extremely short bursts of energy with pulse durations of a few tens to hundreds of attoseconds. Since there are two field maxima in a laser period, two attosecond pulses are produced every laser period corresponding to odd harmonic orders in the spectral domain, which can be explained easily by a simple Fourier transform of a train of attosecond pulses separated in time by a half optical period. Single attosecond pulses can be extracted from these attosecond pulse trains by suitable gating techniques, a topic discussed in detail in Chapter 2. From a quantum mechanical point-of-view, a part of the wavefunction tunnels out from the atom during first step, which evolves during propagation and on return

quantum mechanically interferes with the original wavefunction, emitting photon wavepackets as a result.

Coming back to the semi-classical model, consider a linearly polarized laser field in two dimensions in atomic units

$$\vec{F}(t) = F\,cos(\omega t)\,\hat{x}. \quad 1.1$$

During the second step, the free electron is accelerated in the laser field, which is governed by Newton's second law, and the acceleration of the freed electron is given as

$$a(t) = \frac{d^2x}{dt^2} = -Fcos(\omega t). \quad 1.2$$

Integrating with respect to time to get velocity gives:

$$v(t) = \frac{dx}{dt} = -F\int cos(\omega t')dt', \quad 1.3$$

$$v(t) = -F\frac{sin(\omega t)}{\omega} + c_1. \quad 1.4$$

where c_1 is a constant of integration and depend on initial conditions. From the initial condition $v(t = t_0) = v_0$, we get

$$v(t) = -\frac{F}{\omega}[sin(\omega t) - sin(\omega t_0)] + v_0. \quad 1.5$$

Integration again with respect to time yields

$$x(t) = \int\left\{-\frac{F}{\omega}[sin(\omega t') - sin(\omega t_0)] + v_0\right\}dt' \quad 1.6$$

$$x(t) = \frac{F}{\omega^2}cos(\omega t) + t\frac{F}{\omega}sin(\omega t_0) + v_0 + c_2, \quad 1.7$$

where c_2 is also a constant of the integration and depends on initial conditions. From the initial condition $x(t = t_0) = x_0$, where t_0 is the time of the birth of the electron, we get

$$x(t) = \frac{F}{\omega^2}[cos(\omega t) - cos(\omega t_0) + \omega(t - t_0)\,sin(\omega t_0)] + (t - t_0)v_0 + x_0. \quad 1.8$$

When $x_0 = 0$, assuming the parent atom to be at the origin, this becomes

$$x(t) = \frac{F}{\omega^2}[cos(\omega t) - cos(\omega t_0) + \omega(t - t_0)\,sin(\omega t_0)] + (t - t_0)v_0. \quad 1.9$$

During the third step, when the accelerated electron returns to the parent atom for re-collision, $x(t = t_r) = 0$, where t_r is the time of re-collision, and

$$\frac{F}{\omega^2}[cos(\omega t_r) - cos(\omega t_0) + \omega(t_r - t_0)\,sin(\omega t_0)] + (t_r - t_0)v_0 = 0, \quad 1.10$$

which is also called the return condition. The numerical solution of equation 1.10 for a monochromatic linearly polarized pulse with frequency ω_0 in the domain $\omega_0 t_0 = \left[0, \frac{\pi}{2}\right]$ and

$v_0 = 0$ is presented in Figure 1-1. The kinetic energy can be calculated from equation 1.5 and is plotted in Figure 1-2 in units of $U_p = \frac{{E_0}^2}{4{\omega_0}^2}$ also called the pondermotive potential and in general $U_p = \frac{(e\,E_0)^2}{4m{\omega_0}^2}$, where e and m are the charge and mass of the electron, respectively, and $E_0 = F$ is the electric field amplitude:

$$K(t_r) = 2\,U_p[sin(\omega t_r) - sin(\omega t_0)]^2. \qquad 1.11$$

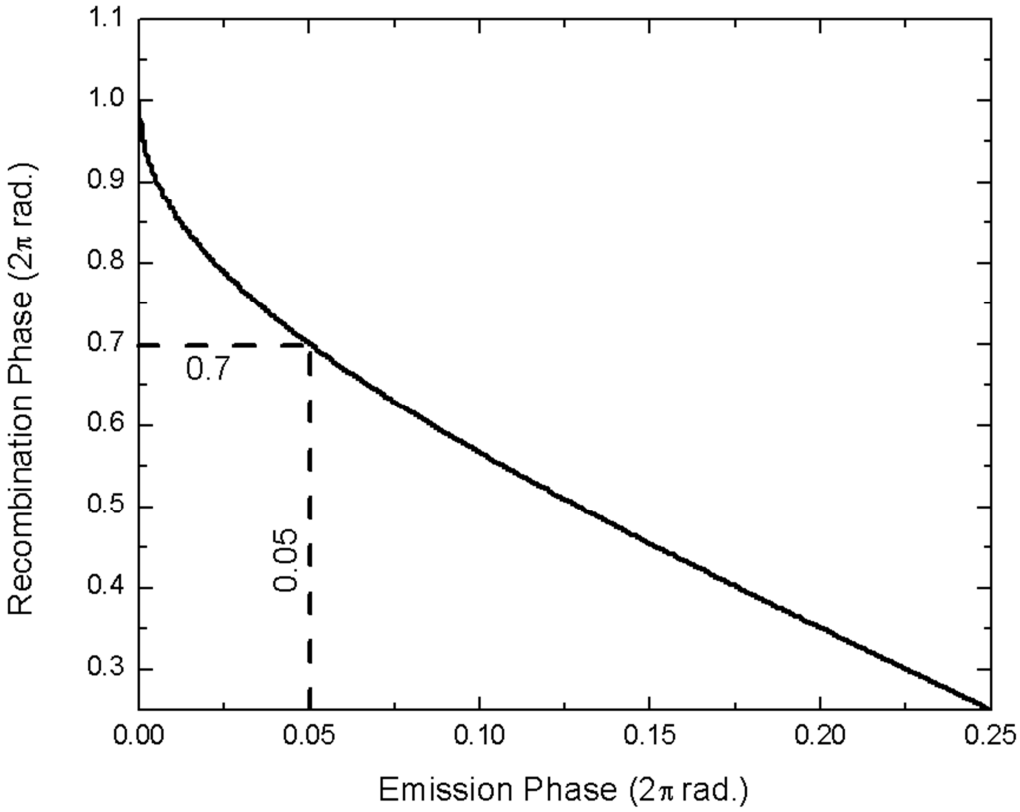

Figure 1-1 Return phase as a function of emission phase calculated using equation 1.10.

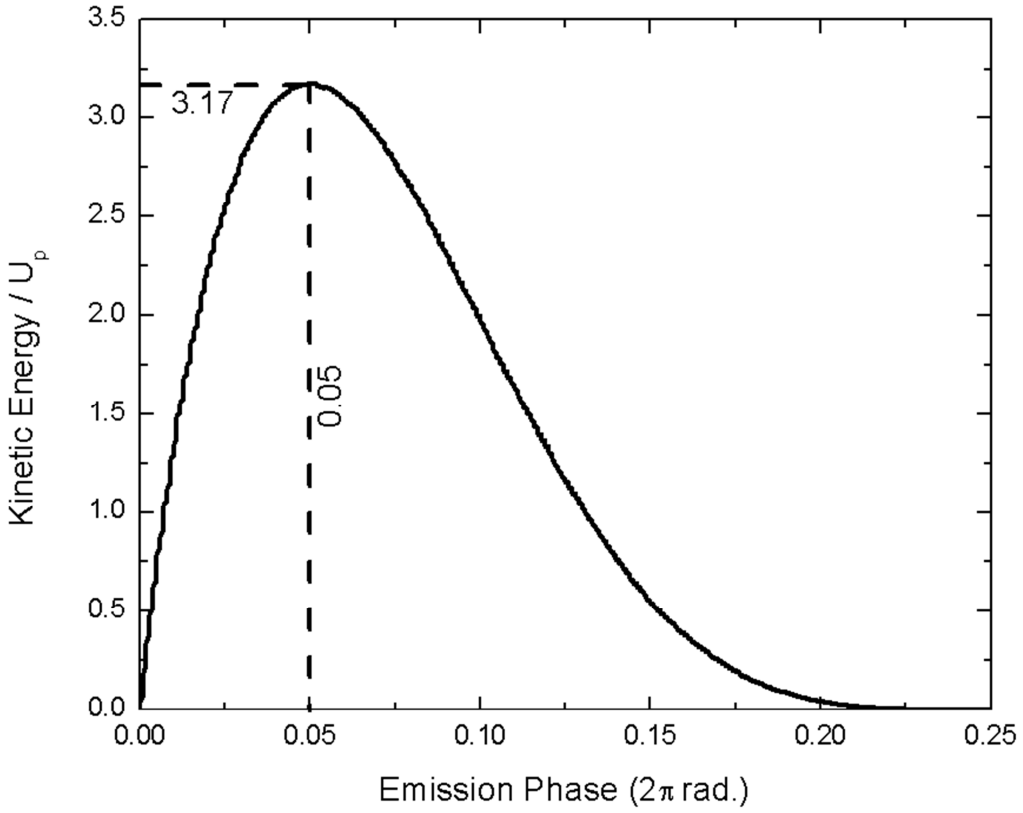

Figure 1-2 Kinetic energy as a function of emission phase calculated using equation 1.11.

It can be noticed from Figure 1-2, that the maximum kinetic energy is $3.17\ U_p$ at $\omega t_0 = 0.05 * 2\pi$ and $\omega t_r = 0.7 * 2\pi$. Thus the maximum photon energy that can be generated from re-collision is

$$E_{max} = I_p + 3.17\ U_p, \qquad 1.12$$

which is also called the cutoff energy and defines the cutoff point of the high harmonic spectrum. Additionally, it can be seen in Figure 1-2 that an electron released at $t_r < 0.05T_0$ and $t_r > 0.05T_0$ can have the same kinetic energy. As seen in Figure 1-1, an electron released before $0.05T_0$ will return later in time than an electron released after $0.05T_0$. Hence, the former electron will have a longer trajectory than the latter. The electron released before $0.05T_0$ is termed "the long-trajectory electron", while the one released later is termed "the short-trajectory electron".

Intrinsic chirp in attosecond pulses

From equation 1.11, it can be observed that the kinetic energy of the electron depends on the return time and hence, the photon energy also changes as a function of time, which is the origin of the intrinsic chirp in attosecond pulses. The kinetic energy as a function of the

recombination phase is presented in figure 1-3, which is calculated from equation 1.10 and 1.11. In atomic units, the chirp C can be defined as

$$\frac{1}{C} = \frac{d\omega_x(t)}{dt} \propto \frac{dK(t)}{dt}. \quad 1.13$$

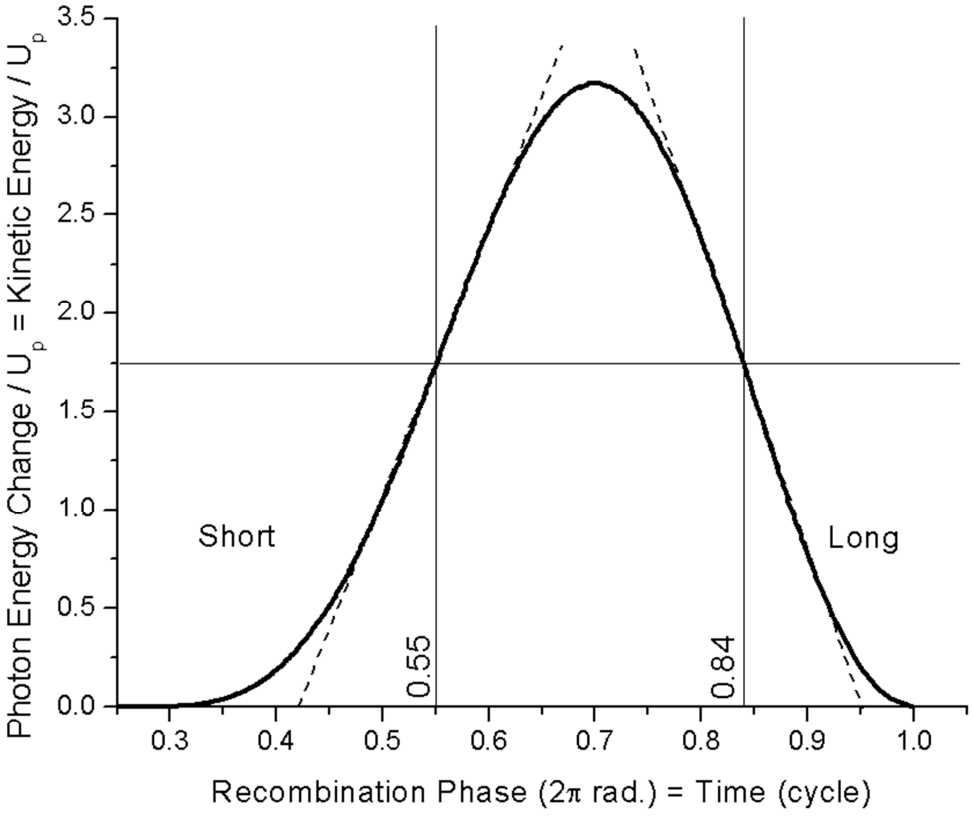

Figure 1-3 Origin of chirp in attosecond pulses.

It can be seen from Figure 1-3 that short trajectories have a positive slope meaning positively chirped and long trajectories have a negative slope and hence are negatively chirped. Additionally, for short trajectories $t_r \approx 0.55 * 2\pi = 0.55T_0$ (where T_0 is the laser period) and for long trajectories $t_r \approx 0.85 * 2\pi = 0.85T_0$, which corresponds to the birth time $t_0 \approx 0.107T_0$ and $t_0 \approx 0.0123T_0$ respectively.

Chirp can be derived by taking the derivative of equation 1.11 with respect to time as

$$C(t_r, t_0) = -\frac{T_0}{U_p} \frac{\omega_0(t_r - t_0)}{8\pi[sin(\omega t_r) - sin(\omega t_0)][sin(\omega t_r) - sin(\omega t_0) - cos(\omega t_r)\omega_0(t_r - t_0)]}, \quad 1.14$$

which is plotted as a function of kinetic energy in Figure 1-4. For short trajectories, setting $t_r \approx 0.55 * 2\pi$ and $t_0 \approx 0.107 * 2\pi$ in equation 1.14 leads to

$$C(t_r = 0.55 * 2\pi, t_0 = 0.107 * 2\pi) = 0.069 \frac{T_0}{U_p} = 24.65 \times 10^{14} \frac{1}{I_0 \lambda_0}, \quad 1.15$$

where I_0 is in W/cm^2 and λ_0 is in μm, while the chirp is in units of as/eV. Also C[as^2]=C[as/eV]/1.516x10^{-3}.

For long trajectories, setting $t_r \approx 0.85 * 2\pi$ and $t_0 \approx 0.0123 * 2\pi$ in equation 1.14 leads to

$$C(t_r = 0.85 * 2\pi, t_0 = 0.0123 * 2\pi) = -0.059 \frac{T_0}{U_p} = -21.08 \times 10^{14} \frac{1}{I_0 \lambda_0}, \quad 1.16$$

where I_0 is in W/cm^2 and λ_0 is in μm, while chirp is in units of as/eV. Intrinsic chirp as a function of laser intensity for long and short trajectories is plotted in figure 1-4 using equation 1.15 and 1.16 for 800nm wavelength. It can be seen that the chirp reduces with increasing intensity, thus intensity can be used as an experimental knob to control attosecond chirp.

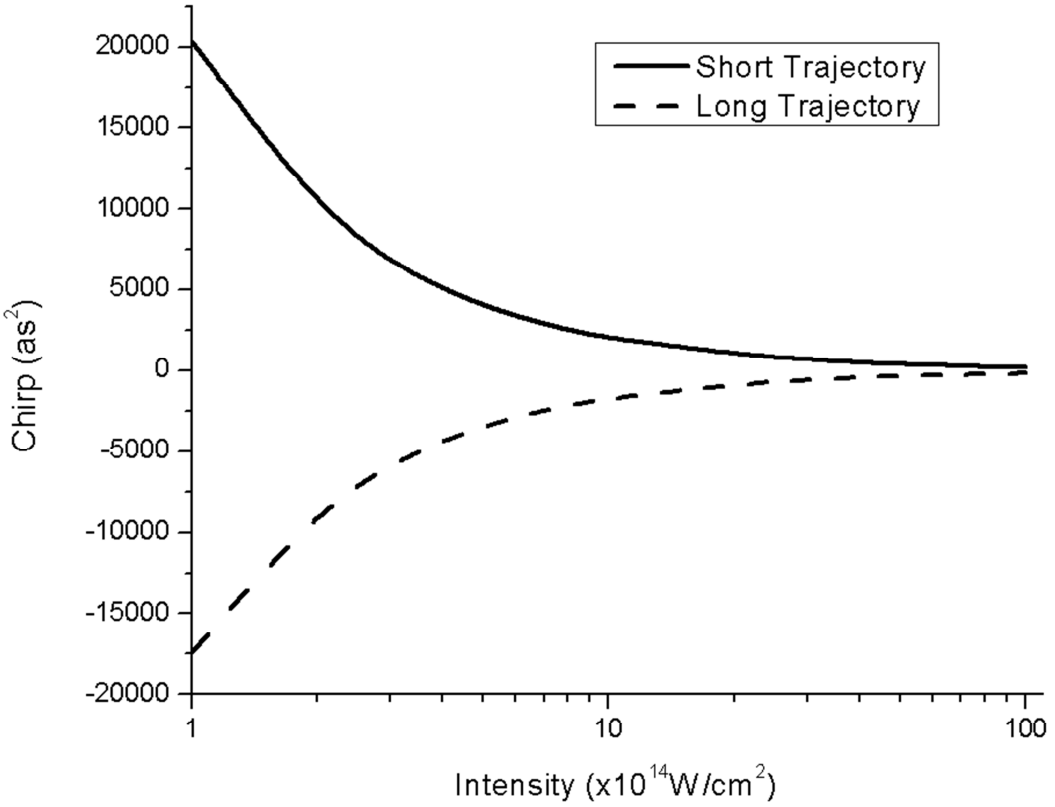

Figure 1-4 Intrinsic Chirp in attosecond pulses for short and long trajectories as a function of laser intensity.

References

[1] A. H. Zewail, "Femtochemistry. Past, present, and future", Pure Appl. Chem., 72, 12, 2219 (2000).

[2] M. Hentschel, R. Kienberger, Ch. Spielmann, G.A. Reider, N.Milosevic, T. Brabec, P. Corkum, U. Heinzmann, M. Drescher, F. Krausz, "Attosecond metrology", Nature 414, 509 (2001).

[3] G. Sansone, E. Benedetti, F. Calegari, C. Vozzi, L. Avaldi, R. Flammini, L. Poletto, P. Villoresi, C. Altucci, R. Velotta, S. Stagira, S. De Silvestri and M. Nisoli, "Isolated Single-Cycle Attosecond Pulses", Science 314, 443 (2006).

[4] X. Feng, S. Gilbertson, H. Mashiko, H. Wang, S. D. Khan, M. Chini, Y. Wu, K. Zhao, and Z. Chang, "Generation of isolated attosecond pulses with 20 to 28 femtosecond lasers," Phys. Rev. Lett. 103, 183901 (2009).

[5] S. Gilbertson, Y. Wu, S. D. Khan, M. Chini, K. Zhao, X. Feng, and Z. Chang, "Isolated attosecond pulse generation using multicycle pulses directly from a laser amplifier," Phys. Rev. A 81, 043810 (2010).

[6] F. Ferrari, F. Calegari, M. Lucchini, C. Vozzi, S. Stagira, G. Sansone, and M. Nisoli, "High-energy isolated attosecond pulses generated by above-saturation few-cycle fields", Nat. Photonics 4, 875 (2010).

[7] H. Mashiko, S. Gilbertson, C. Li, E. Moon, and Z. Chang, "Optimizing the photon flux of double optical gated high-order harmonic spectra", Phys. Rev. A, 77, 063423 (2008).

[8] Q. Zhang, K. Zhao, and Z. Chang, "Determining time resolution of microchannel plate detectors for electron time-of-flight spectrometer," Rev. Sci. Instrum. 81, 073112 (2010).

[9] K. Zhao, Q. Zhang, M. Chini, S. Gilbertson, S. D. Khan and Z. Chang, "Broadband Isolated Attosecond Pulse Generation and Characterization", App. Phys. Lett. (submitted).

[10] M. Chini, H. Mashiko, H. Wang, S. Chen, C. Yun, S. Scott, S. Gilbertson, and Z. Chang, "Delay control in attosecond pump-probe experiments," Opt. Express 17, 21459-21464 (2009).

[11] H. Wang, M. Chini, S. Chen, C.-H. Zhang, F. He, Y. Cheng, Y. Wu, U. Thumm, and Z. Chang, "Attosecond Time-Resolved Autoionization of Argon," Phys. Rev. Lett. 105, 143002 (2010).

[12] S. Gilbertson, M. Chini, X. Feng, S. Khan, Y. Wu, and Z. Chang, “Monitoring and Controlling the Electron Dynamics in Helium with Isolated Attosecond Pulses,” Phys. Rev. Lett. 105, 263003 (2010).
[13] http://www.guinnessworldrecords.com/records-1000/shortest-flash-of-light/
[14] A. McPherson, G. Gibson, H. Jara, U. Johann, T. S. Luk, I. A. McIntyre, K. Boyer, and C. K. Rhodes, "Studies of multiphoton production of vacuum-ultraviolet radiation in the rare gases", JOSA B, Vol. 4, Issue 4, pp. 595-601 (1987)
[15] M. Ferray, A. L'Huillier, X. F. Li, L. A. Lompre, G. Mainfray and C. Manus, "Multiple-harmonic conversion of 1064 nm radiation in rare gases", J. Phys. B: At. Mol. Opt. Phys., 21, L31 (1988)
[16] P. B. Corkum, “Plasma perspective on strong field multiphoton ionization”, Phys. Rev. Lett. 71, 1994 (1993).

Chapter 2 - Generating single attosecond pulses

In this chapter, we will provide an overview of gating techniques to extract single attosecond pulses from a train of attosecond pulses. When ultrashort pulses from a Ti:Sapphire laser are focused in a noble gas medium like argon, neon, helium, etc., attosecond pulses are produced at every half optical cycle and the generation can be explained by the semi-classical 3-step model as discussed in the previous chapter. An optical gating technique is required to allow attosecond pulses to be produced only once rather than at every half optical cycle. For a typical output of Ti:Sapphire lasers, the half optical cycle is 1.33 fs (for 800 nm wavelength), which means that extremely short gate widths are desirable for generation of single attosecond pulses. Such short gate widths are quite challenging but luckily several optical gating techniques have been successfully demonstrated to extract single attosecond pulses from a pulse train. These optical gating techniques can be classified as temporal and spectral gating.

Overview of gating techniques

Amplitude gating

The single attosecond pulses were first demonstrated in 2001 by Hentschel et al. [1] using a technique termed amplitude gating, which is basically spectral gating. They demonstrated that at zero carrier envelope phase (CE-phase), single cycle pulses lead to high harmonic generation containing a continuous portion near the cut-off, which has a majority contribution from the recollision at the peak of the electric field. This continuous portion is spectrally filtered from the rest by using an appropriate spectral filter (like a zirconium filter and/or a Mo/Si multi-layer mirror). This method requires single cycle pulses and very good CE-phase stability. Since development of high power single-cycle pulses with CE-phase lock is a technical challenge, such techniques are very limited in the generation of intense single attosecond pulses. The shortest attosecond pulse of 80 as was demonstrated by Goulielmakis et al. [2] using amplitude gating from sub-4 fs pulses.

Polarization gating

Single attosecond pulses were also produced successfully by another technique called polarization gating (PG), which is a type of temporal gating. In PG, an elliptically dependent

pulse is produced by combining left and right circularly polarized pulses separated in time. The leading portion of one combines with the trailing portion of the other, resulting in a very short linearly polarized region. Since the efficiency of high harmonic generation is a strong function of ellipticity, the attosecond pulses are only produced in this linear region, which defines the gate width of the PG pulse. In contrast to amplitude gating, this gate width depends not only on the pulse duration of both circular pulses τ_p, but also on the delay between them defined by T_d. This relaxes the constraint on the pulse duration and even multi-cycle pulses can be used, but CE-phase locking is still required. Sansone et al. [3] demonstrated 130 as single attosecond pulses using PG in 2006. However since attosecond pulses are produced every half optical cycle, the gate width should be less than this. For 800 nm pulses the maximum gate width can be 1.33 fs. Additionally, if the pulse duration τ_p is too long, then it may be possible that the leading circular part depletes all the gas atoms and no atoms are left in the linear part to ionize, and hence no attosecond pulses are created. Due to these two constraints, namely half cycle gate width and gas depletion, PG is still limited and difficult to implement in many labs.

The PG pulse is a combination of left and right circularly polarized pulses, which may be given as [4]:

$$\vec{E}_l(t) = E_0 e^{-2\,ln(2)\left(\frac{t-\frac{T_d}{2}}{\tau_p}\right)^2} [\hat{x}\,cos(\omega t+\varphi) + \hat{y}\,sin(\omega t+\varphi)](-1)^n \qquad 2.1$$

$$\vec{E}_r(t) = E_0 e^{-2\,ln(2)\left(\frac{t+\frac{T_d}{2}}{\tau_p}\right)^2} [\hat{x}\,cos(\omega t+\varphi) - \hat{y}\,sin(\omega t+\varphi)](-1)^n \qquad 2.2$$

Where E_0 is the peak field amplitude, τ_p is the pulse duration, ω is the carrier frequency, φ is the carrier envelope phase, T_d is the delay between left and right circular pulses and n is the number of optical periods. The combined electric field can be given as [4]:

$$\vec{E}(t) = E_0 \left\{ \hat{x} \left[e^{-2\,ln(2)\left(\frac{t-\frac{T_d}{2}}{\tau_p}\right)^2} + e^{-2\,ln(2)\left(\frac{t+\frac{T_d}{2}}{\tau_p}\right)^2} \right] cos(\omega t+\varphi) + \hat{y} \left[e^{-2\,ln(2)\left(\frac{t-\frac{T_d}{2}}{\tau_p}\right)^2} - e^{-2\,ln(2)\left(\frac{t+\frac{T_d}{2}}{\tau_p}\right)^2} \right] sin(\omega t+\varphi) \right\} (-1)^n, \qquad 2.3$$

where the ellipticity is given as the ratio of the electric field along the y and x direction as [4]

$$\varepsilon(t) = \frac{\left| e^{-2\,ln(2)\left(\frac{t-\frac{T_d}{2}}{\tau_p}\right)^2} - e^{-2\,ln(2)\left(\frac{t+\frac{T_d}{2}}{\tau_p}\right)^2} \right|}{e^{-2\,ln(2)\left(\frac{t-\frac{T_d}{2}}{\tau_p}\right)^2} + e^{-2\,ln(2)\left(\frac{t+\frac{T_d}{2}}{\tau_p}\right)^2}} = \frac{\left| 1 - e^{-4\,ln(2)\frac{T_d}{{\tau_p}^2}t} \right|}{1 + e^{-4\,ln(2)\frac{T_d}{{\tau_p}^2}t}}. \quad 2.4$$

This ellipticity is plotted in figure 2-1 (dashed curve) for $T_d = \tau_p$=10 fs. In later chapters we present experimental data showing that the harmonic efficiency drops rapidly when ellipticity increases from 0 to 0.2, so we are only interested in the narrow linear region where $4\,ln(2)\frac{T_d}{{\tau_p}^2}t \ll 1$ and equation 2.4 can be approximated by a Taylor series expansion of the exponential function, and ignoring higher orders terms

$$\varepsilon(t) \approx \left| 2\,ln(2)\frac{T_d}{{\tau_p}^2}t \right|. \quad 2.5$$

This is also plotted in figure 2.1 and compared with equation 2.4. A good match is quite evident from figure 2-1 within the small ellipticity approximation. The time interval where ellipticity is less than a certain value ε_{th} can be obtained as [4]

$$\delta t = \frac{\varepsilon_{th}}{\ln(2)}\frac{\tau_p^2}{T_d}. \quad 2.6$$

If we define ε_{th} as the ellipticity where harmonic efficiency drops by 1 order of magnitude, then δt gives the gate width of the PG field.

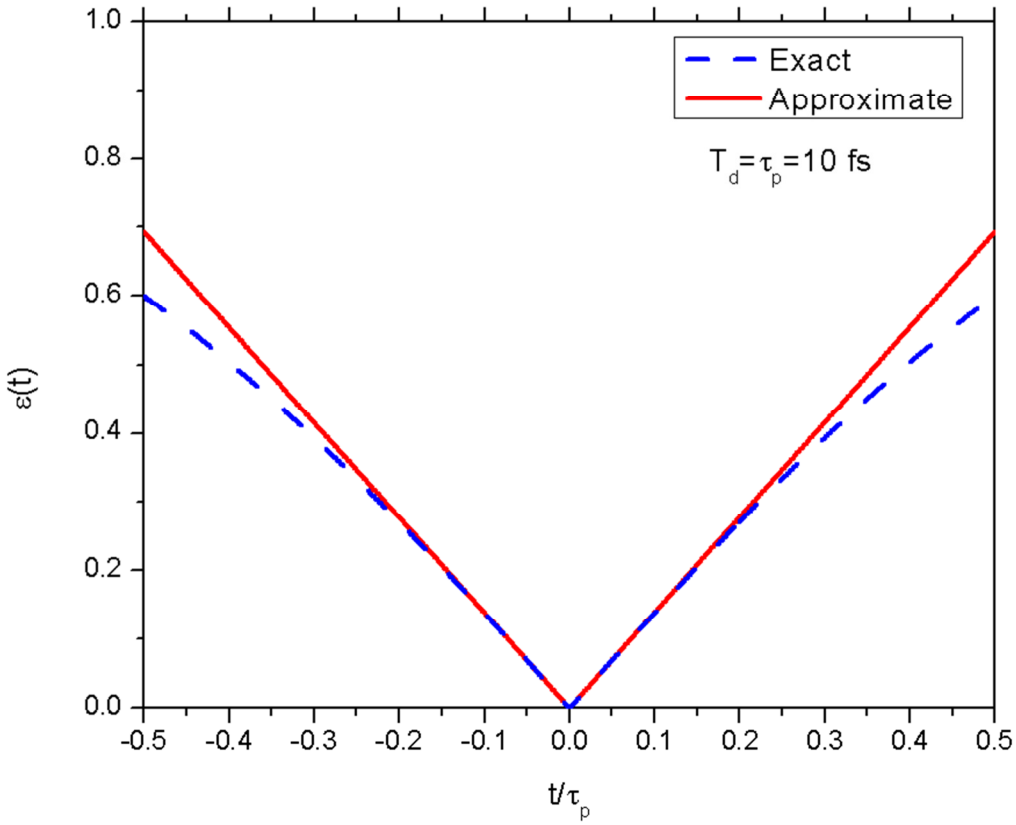

Figure 2-1 Time dependent ellipticity calculated using the exact expression in equation 2.4 (blue dash) and approximate expression in equation 2.5 (red continuous) [4].

The x and y components of equation 2.3 are plotted in figure 2-2. Here it can be seen that the y-component is zero at t=0 while the x-component is non-zero. We define the x-component as the driving field because the non-zero part within the linear region which is close to t=0 is responsible for the generation of a single attosecond pulse. Additionally, we define the y-component as the gating field because its addition in the driving field changes the ellipticity, which defines the gate width of the PG field.

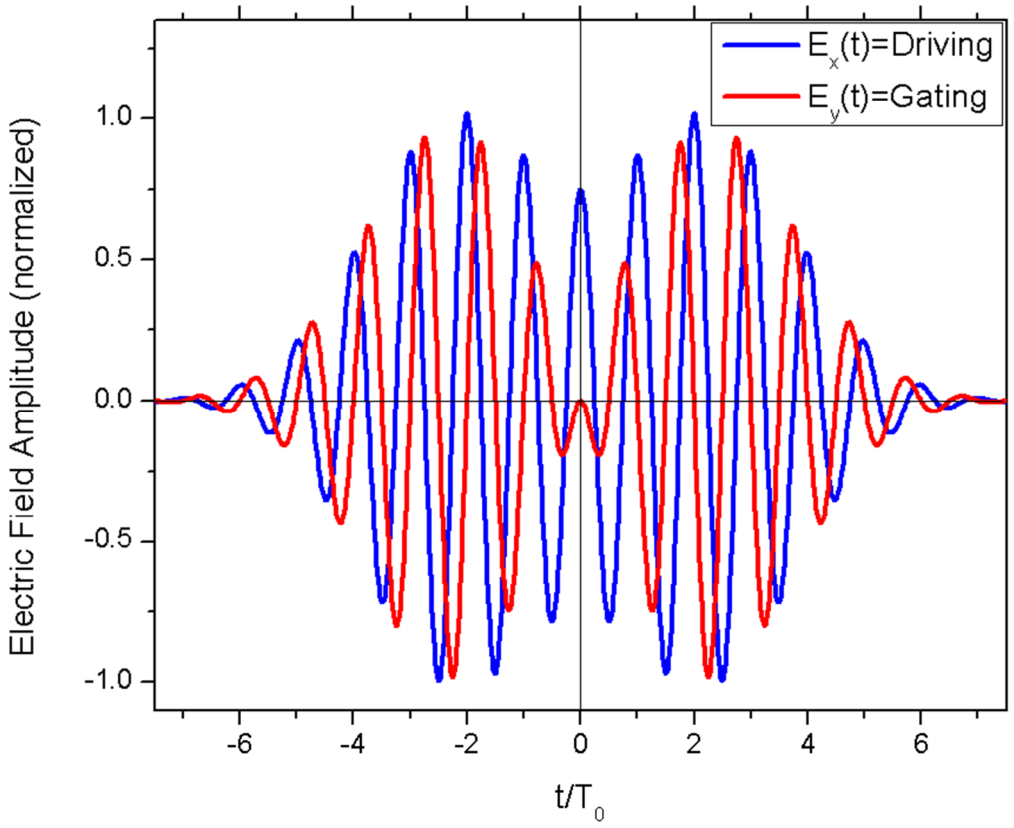

Figure 2-2 x-component (blue) and y-component (red) of PG field given by equation 2.3.

Two color gating

Since noble gases have a centro-symmetric potential the high harmonics produced from them only show odd orders. From a Fourier transform it can be seen that odd harmonics mean that pulses are produced every half optical cycle in the time domain. To see both even and odd orders (pulses every full optical cycle) the symmetry of the potential must be broken. This is usually done in non-linear optics by using crystals exhibiting non-centro-symmetric potentials, like BBO, KDP, etc. However, symmetry can also be broken by using non-symmetric electric fields. By adding a weak second harmonic to the fundamental, attosecond pulses from positive peaks of the electric field are enhanced and from negative peaks are reduced. Since high harmonic generation is a highly non-linear process, attosecond pulses are only produced at positive peaks and are suppressed at negative peaks, thus producing pulses every full optical cycle. As a result both even and odd harmonics are present in the high harmonic spectrum. This gating technique, when combined with amplitude gating or polarization gating, releases the

constraint on the pulse duration. We have termed the combination of two-color gating and polarization gating as double optical gating (DOG).

800nm double optical gating

By combining two color gating with polarization gating we introduced a new gating technique, which we termed double optical gating (DOG), which increased the maximum gate width to a full optical cycle and further reduced the constraint on pulse duration of the circular pulses. Figure 2-3(a) presents the central part of a typical 800nm long pulse. Attosecond pulses as indicated in blue are produced every half optical cycle corresponding to the maxima in the upward and downward direction. The mechanism of these bursts can be explained by the semi-classical 3-step model as already discussed in Chapter 1. By adding a weak second harmonic, we can break the symmetry of the fundamental pulses as presented in Figure 2-3(b). As a result, attosecond pulses are produced from the maxima in the upward direction only, and thus attosecond bursts are produced every full optical cycle. This, when combined with PG pulses, leads to isolated single attosecond pulses. PG pulses are presented in figure 2-3(c) with half cycle gate width, and DOG pulses are presented in figure 2-3(d). The full optical cycle gate width is quite evident in figure 2-3(d).

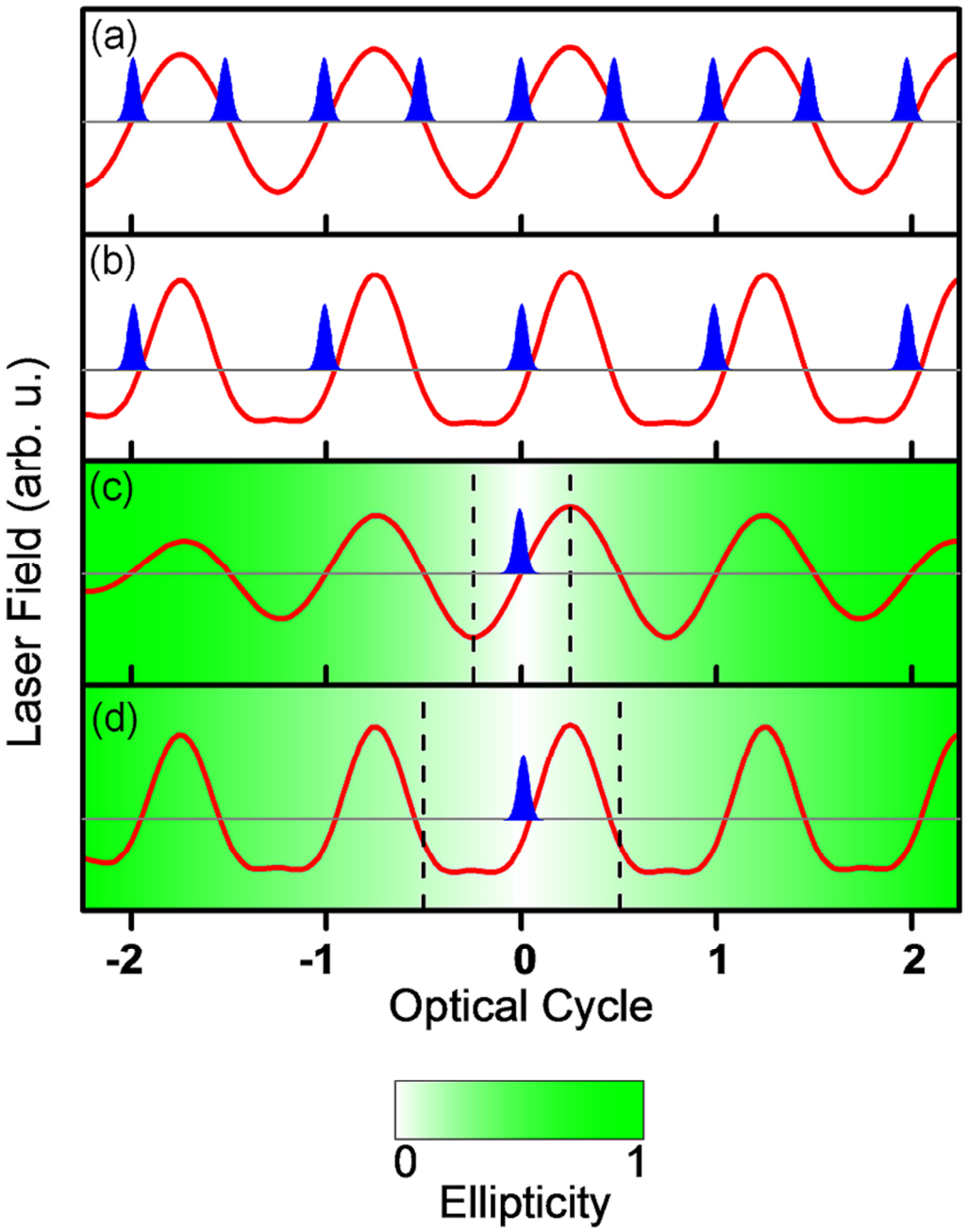

Figure 2-3 Burst of attosecond pulses generated every half optical cycle by the fundamental laser field (a), weak second harmonic added to fundamental (two-color gating) breaks the symmetry and produces attosecond pulses every full optical cycle (b), single attosecond pulse produced by PG with half cycle gate width (c) and single attosecond pulse produced by DOG with full cycle gate width (d) [5].

A DOG pulse can be produced by using two quartz waveplates and a BBO crystal. The optical arrangement is presented in Figure 2-4. The first quartz plate thickness defines the delay T_d between the left and right circularly polarized pulses and depends on the pulse duration of the input pulse. The second quartz plate and BBO crystal combine to form a quarter waveplate. Additionally the BBO produces a weak second harmonic to get the two color effect. The second quartz plate was set to $5\frac{1}{4}$ retardation and the BBO was set to -5. A linearly polarized pulse is split into two orthogonal linear pulses along the e-ray and o-ray axes with a delay T_d. The two orthogonal linear pulses are rotated by the combination of the second quartz plate and the BBO into left and right circularly polarized pulses with an additional weak second harmonic from the BBO. The retardation of the first quartz plate can be calculated from equation 2.3 by setting the gate width equal to a full cycle delay.

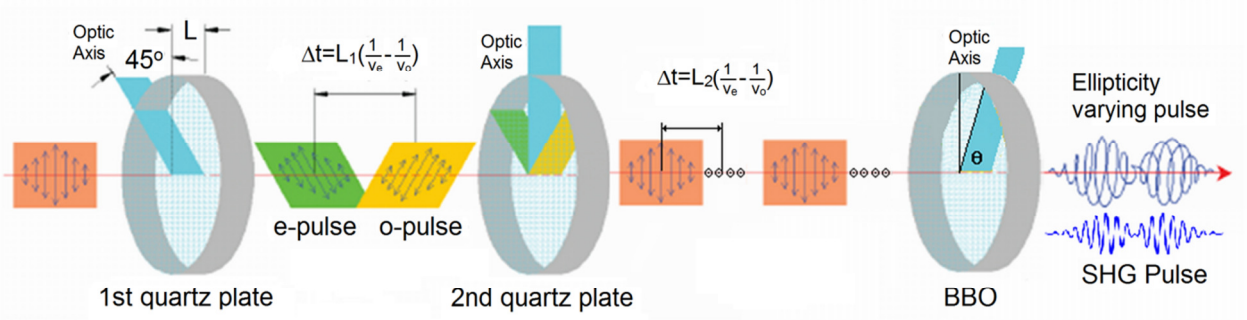

Figure 2-4 Optical arrangement of collinear DOG [5].

Setting δt to half and full optical cycles in equation 2.6 for the PG and DOG cases, respectively, we get

$$\frac{T_0}{2} = \frac{\varepsilon_{th}}{\ln(2)} \frac{\tau_p^2}{T_d^{PG}} \quad \text{and} \quad T_0 = \frac{\varepsilon_{th}}{\ln(2)} \frac{\tau_p^2}{T_d^{DOG}}, \tag{2.7}$$

where T_0 is the full cycle delay and T_d^{PG} and T_d^{DOG} are retardations for PG and DOG respectively. By comparison we get:

$$T_d^{PG} = 2T_d^{DOG} \tag{2.8}$$

Hence, the retardation T_d due to DOG is half of T_d from PG. As a result, for the same intensity within the gate a lower peak intensity of left and right circularly polarized pulses is required in DOG, which leads to less depletion of the gas due to the leading circular pulse. This is also

evident in Figure 2-5, where comparison of the gas depletion from PG and DOG pulses is presented as a function of pulse duration using ADK theory at an intensity of $1.9x10^{14}W/cm^2$ within the gate. For the case of PG the gas is fully depleted at ~8 fs, while full depletion is seen at ~16 fs in the case of DOG.

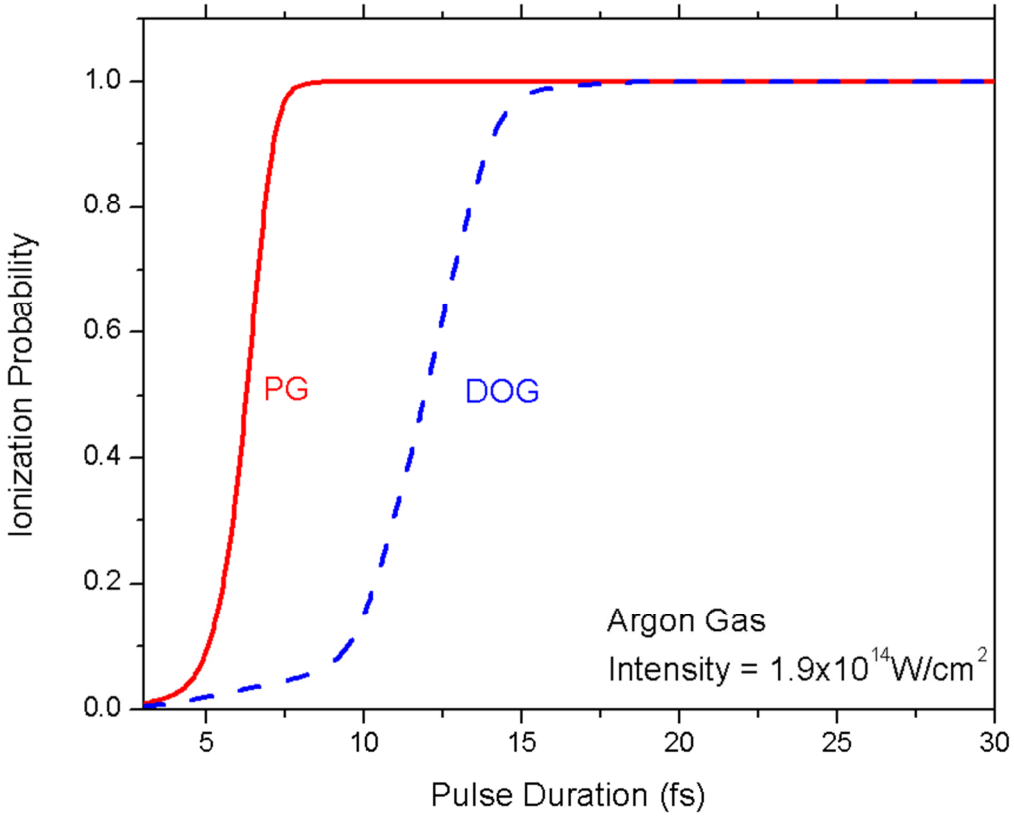

Figure 2-5 Ionization probability of Argon gas as a function of pulse duration at the intensity of $1.9x10^{14}W/cm^2$ within the gate for PG (red continuous) and DOG (blue dashed) [6].

800nm generalized double optical gating

In an attempt to reduce gas depletion further, a BK7 or fused silica window at the brewster angle can be used to reflect away some portion of the driving pulses while allowing full transmission of the gating pulse. This is presented in Figure 2-6, and we call it Generalized Double Optical Gating (GDOG). This results in elliptical leading and trailing pulses with a linear

pulse in the middle. In addition to less depletion, this further reduces the constraint on pulse duration due to the introduction of a factor of 0.5 in equation 2.6, which is

$$\delta t = 0.5\frac{\varepsilon_{th}}{\ln(2)}\frac{\tau_p^2}{T_d}. \qquad 2.9$$

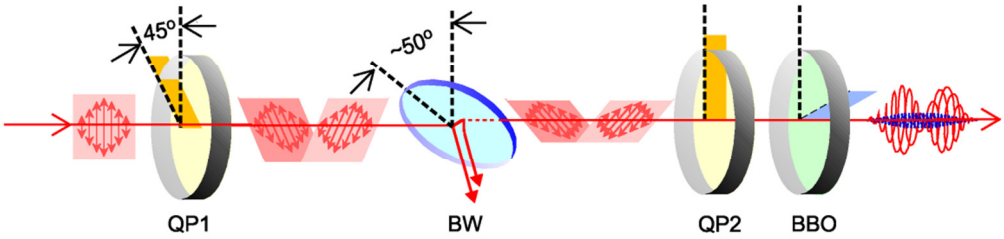

Figure 2-6 Optical arrangement of collinear GDOG. A brewster window is introduced between the 1st and 2nd quartz plates [5].

Setting δt to the full optical cycle in equation 2.6 for DOG and in equation 2.9 for the GDOG cases, we get

$$T_0 = \frac{\varepsilon_{th}}{\ln(2)}\frac{\tau_p^2}{T_d^{DOG}} \quad \text{and} \quad T_0 = \frac{1}{2}\frac{\varepsilon_{th}}{\ln(2)}\frac{\tau_p^2}{T_d^{GDOG}}, \qquad 2.10$$

where T_d^{DOG} and T_d^{GDOG} are retardations for DOG and GDOG respectively. By comparison we get:

$$T_d^{GDOG} = \frac{1}{2}T_d^{DOG} \qquad 2.11$$

Additionally, by comparison with equation 2.8, we get:

$$T_d^{GDOG} = \frac{1}{2}T_d^{DOG} = \frac{1}{4}T_d^{PG} \qquad 2.12$$

Thus for the same intensity within the gate, the peak intensity of the leading and trailing elliptical pulses is smaller than those in DOG and PG. Figure 2-7(a) and 2-7(b) illustrates the gating field (blue dashed), driving field (red continuous) and ellipticity (green dot-dash) of DOG and GDOG pulses with the same intensity within the gate. The smaller trailing and leading pulses are quite evident. The depletion of gas is also evident from Figure 2-8, where gas depletion as a function of pulse duration is presented for intensity within the gate of $1.9\text{x}10^{14}\text{W/cm}^2$, calculated using

ADK theory for PG, DOG and GDOG. It can be clearly seen that the gas is fully depleted at a pulse duration >25fs, which is much higher than PG and DOG.

GDOG can be used to generate single attosecond pulses directly from a Ti:sapphire amplifier without the requirement of hollow core fiber and chirped mirror compression, which is demonstrated by Gilbertson et al. [6].

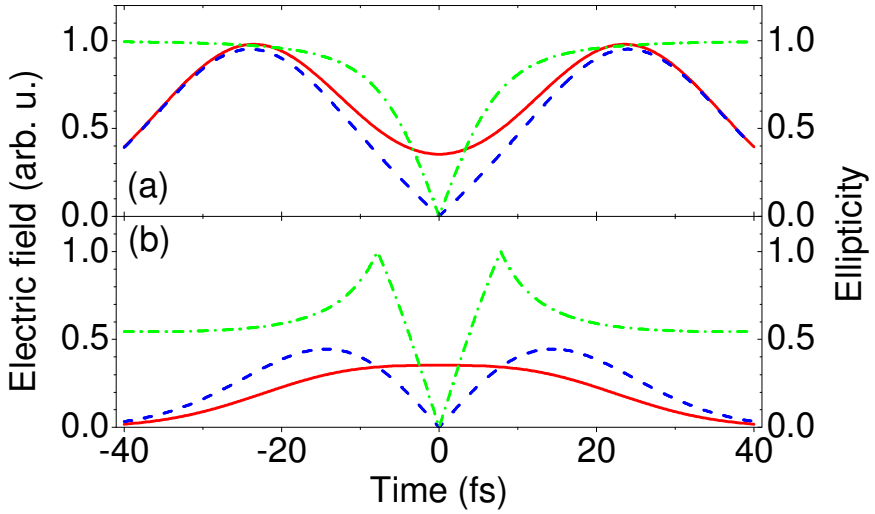

Figure 2-7 Comparison between ellipticity (green dot-dash), driving (red continuous) and gating field (blue dash) for DOG (a) and GDOG (b) with the same intensity within the gate [7].

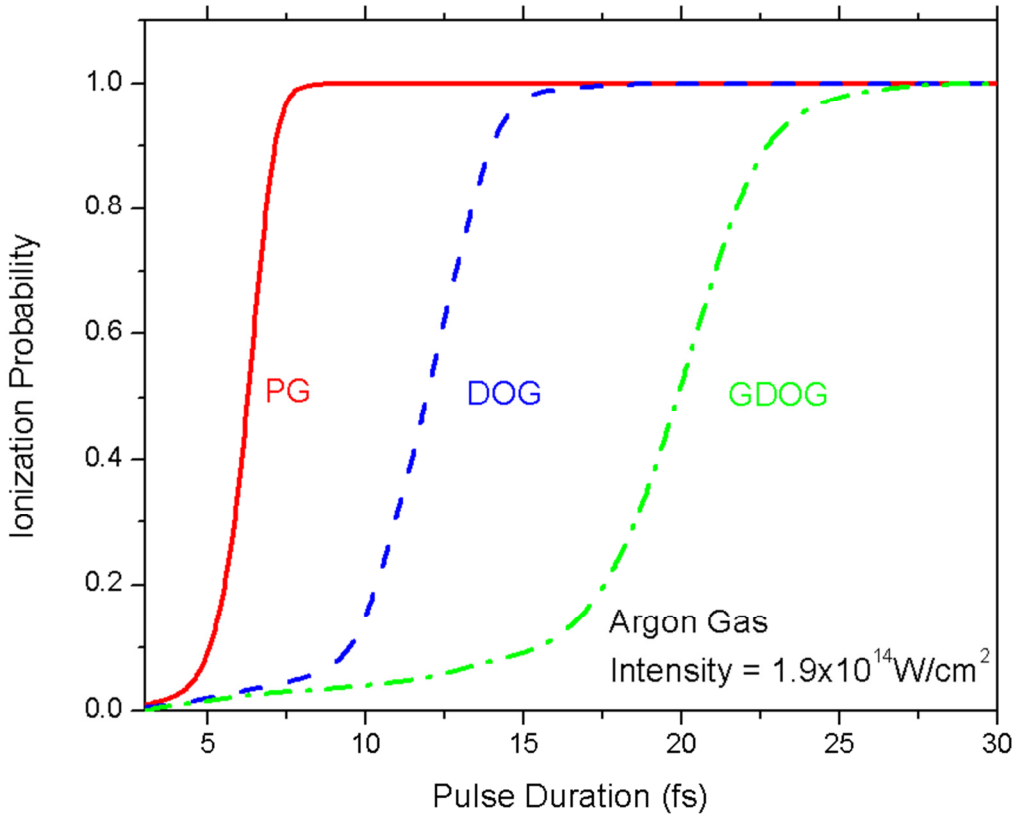

Figure 2-8 Ionization probability of Argon gas as a function of pulse duration at the intensity of 1.9×10^{14}W/cm^2 within the gate for PG (red continuous), DOG (blue dashed) and GDOG (green dot-dash) [6].

High harmonic generation from solid targets

In addition to rare gases, high harmonics have also been demonstrated from ionized species in laser ablated plasmas [8]. Elouga Bom et al. [9] demonstrated high harmonics in carbon plasmas with flux as high as a few μJ. The exact mechanism of high harmonic generation from such plasmas is still a question of debate and is under investigation, but roughly speaking it can be explained by the semi-classical 3-step model as discussed in Chapter 1. The electrons are removed from the ionized or neutral species in a laser ablated plasma by tunnel ionization, then propagate in the medium and return back when the electric field switches direction possibly re-colliding with the parent ions. Several advantages have been attributed to this method including the extension of the cutoff energy due to higher ionization potentials and higher flux. Neutral nanoclusters of carbon have been speculated to be the source of such intense harmonics [9],

although work is in progress to find explicit evidence to support this hypothesis. During the Fall of 2010 we collaborated with the ALLS team at INRS and modified our laser to carry out these experiments and make a direct comparison with rare gases under similar conditions. This was the first direct comparison of high harmonic generation from rare gases and from laser ablated carbon plasmas. Based on experimental findings at ALLS, carbon targets were used to produce such plasmas, since the main object was to obtain the highest flux. The laser consists of a Ti:sapphire dispersion compensated oscillator (FemtoLasers's Rainbow Oscillator) and a two stage Ti:sapphire chirped pulse amplifier (Coherent's Legend Duo Elite, 1kHz repetition rate). The amplifier consists of a grating based stretcher, Ti:sapphire regenerative amplifier (13 to 14 round trips), single pass Ti:sapphire amplifier and a grating based compressor. The amplified stretched pulse after the single pass amplifier was split using a 50/50 beam splitter and only 50% was sent to the compressor, while the other 50% was used as an ablation pulse. The pulse duration of the uncompressed and compressed beam was 120 ps and 30 fs respectively. In the experimental setup, presented in Figure 2-9, a carbon target was glued to a gas cell, which made switching between gases and plasmas easy. The uncompressed pre-pulse from the laser came first and was focused on the target, which produced plasma by ablation. The surface of the target was perpendicular to the pre-pulse. To stabilize the plasma and harmonics the repetition rate of the pre-pulse was reduced to 10 Hz by employing a mechanical shutter.

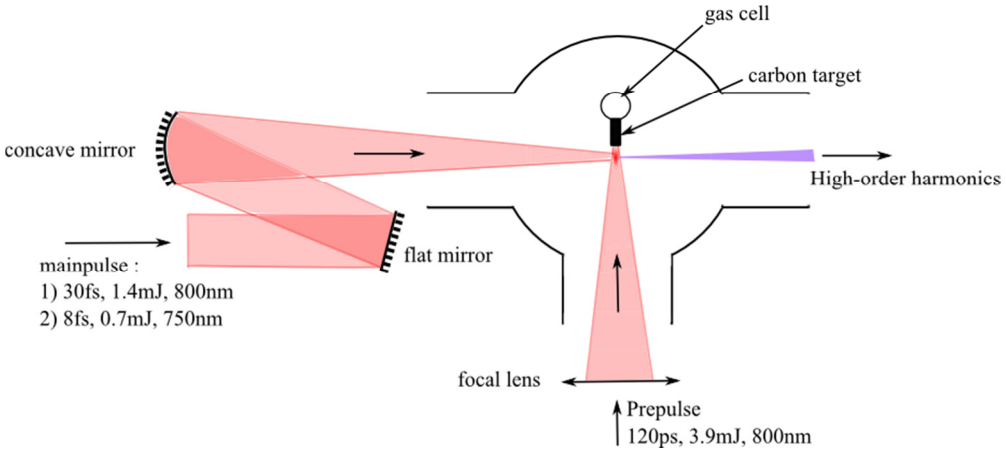

Figure 2-9 Schematic of experimental setup for high harmonic generation from laser ablated carbon plasma [10].

The high harmonic spectra obtained from the argon and carbon targets is presented in Figure 2-10. It was demonstrated that 9.5 times more intense harmonics were produced from

carbon plasmas as compared to argon by using a flux measurement by an XUV photodiode (AXUV100 from Optodiode Corporation). The harmonics were produced at the phase matching position in both cases. However, the overall conversion efficiency was observed to be 1.8×10^{-6}, which is two orders of magnitude smaller than the conversion efficiency measured at ALLS [9]. This reduction in conversion efficiency was attributed to the lower energy of the femtosecond generation pulses. Additionally, the generation pulse was compressed to 8fs with a neon filled hollow core fiber and chirped mirrors, and high harmonic efficiency was compared between argon and carbon plasmas using short pulses. The high harmonic spectra for argon and carbon plasmas are presented in Figure 2-11.

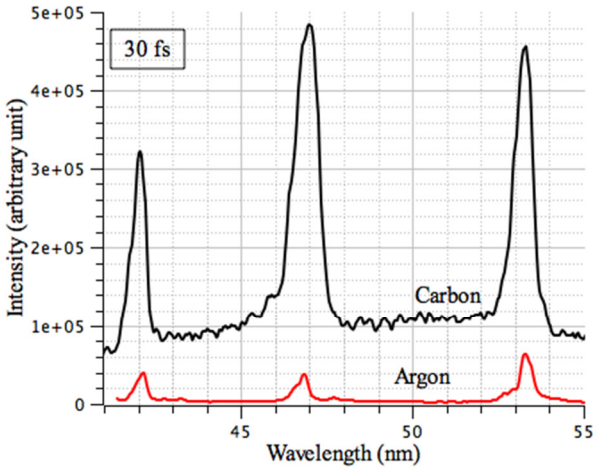

Figure 2-10 High harmonics generated from laser ablated carbon plasma (black) and argon gas (red) driven by 30 fs pulses [10].

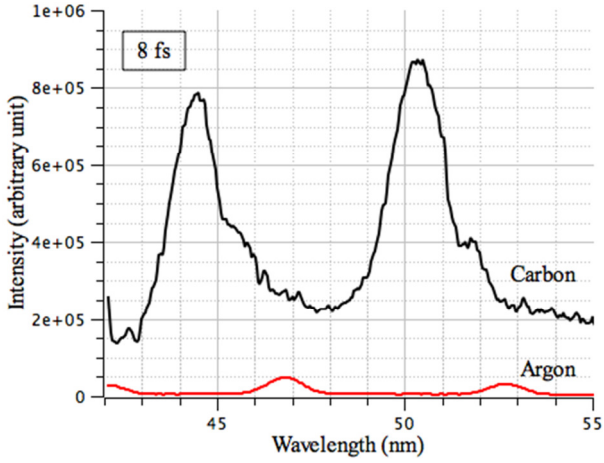

Figure 2-11 High harmonics generated from laser ablated carbon plasma (black) and argon gas (red) driven by 8 fs pulses [10].

Furthermore, we added DOG optics to the short pulses and gated the high harmonics to extract isolated single attosecond pulses. Figure 2-12 presents the spectra with and without gating and a broad continuum is clearly evident. Although a CE-phase scan or attosecond streaking is required to prove single attosecond pulses, such techniques could not be used here as the high harmonics from carbon plasmas were very unstable and of short duration. This was the first demonstration of continuum generation from carbon plasmas and demonstrates the superiority of DOG technique.

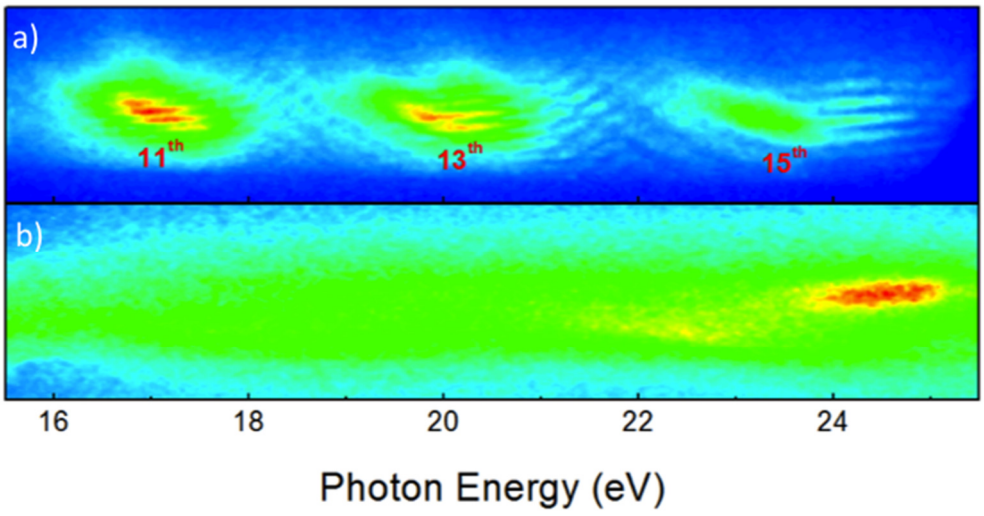

Figure 2-12 (a) Attosecond pulse train generated from laser ablated carbon plasma using an 8 fs linearly polarized laser pulse; 11th to 15th harmonics are evident, (b) High harmonic continuum generated from laser ablated carbon plasma using 8 fs DOG pulse. The color scale of (a) and (b) are normalized [10].

References

[1] M. Hentschel, R. Kienberger, Ch. Spielmann, G. A. Reider, N. Milosevic, T. Brabec, P. Corkum, U. Heinzmann, M. Drescher and F. Krausz, "Attosecond metrology", Nature, 414, 509 (2001).

[2] E. Goulielmakis, M. Schultze, M. Hofstetter, V. S.Yakovlev, J. Gagnon, M. Uiberacker, A. L. Aquila, E. M. Gullikson, D. T. Attwood, R. Kienberger, F. Krausz and U. Kleineberg, "Single-Cycle Nonlinear Optics", Science 320, 1614 (2008).

[3] G. Sansone, E. Benedetti, F. Calegari, C. Vozzi, L. Avaldi, R. Flammini, L. Poletto, P. Villoresi, C. Altucci, R. Velotta, S. Stagira, S. De Silvestri, M. Nisoli, "Isolated Single-Cycle Attosecond Pulses", Science, 314, 443 (2006).

[4] Z. Chang, "Single attosecond pulse and xuv supercontinuum in the high-order harmonic plateau", PRA, 70, 043802 (2004).

[5] S. Chen, S. Gilbertson, H. Wang, M. Chini, K. Zhao, S. D. Khan, Y. Wu and Z. Chang, "Chapter 4 - ATTOSECOND PULSE GENERATION, CHARACTERIZATION AND APPLICATION", Advances in Multi-Photon Processes and Spectroscopy, Vol. 20, World Scientific, ISBN: 978-981-4343-98-5 (2011).

[6] S. Gilbertson, Y. Wu, S. D. Khan, M. Chini, K. Zhao, X. Feng, and Z. Chang, "Isolated attosecond pulse generation using multicycle pulses directly from a laser amplifier", Phys. Rev. A 81, 043810 (2010).

[7] X. Feng, S. Gilbertson, H. Mashiko, H. Wang, S. D. Khan, M. Chini, Y. Wu, K. Zhao, and Z. Chang, "Generation of Isolated Attosecond Pulses with 20 to 28 Femtosecond Lasers", Phys. Rev. Lett., 103, 183901 (2009).

[8] L. Elouga Bom, J-C. Kieffer, R. Ganeev, M. Suzuki, H. Kuroda, and T. Ozaki, "Influence of the main pulse and prepulse intensity on high-order harmonic generation in silver plasma ablation", PRA, 75, 3, 033804 (2007).

[9] L. B. Elouga Bom, Y. Pertot, V. R. Bhardwaj, and T. Ozaki, "Multi-μJ coherent extreme ultraviolet source generated from carbon using the plasma harmonic method", Optics Express, 19, 4, 3077 (2011).

[10] Y. Pertot, S. Chen, S. D. Khan, L. B. Elouga Bom, T. Ozaki, and Z. Chang, "Generation of Continuum High-Order Harmonics from Carbon Plasma using Double Optical Gating", J. Phys. B (submitted).

Chapter 3 - Measurement of single attosecond pulses

Basics of attosecond streaking

In a conventional streak camera the temporal profile of the light pulse is converted into a spatial image on the detector (typically a micro channel plate with phosphor screen). This is achieved by deflecting the electrons across the detector by applying a time-varying electric field. The photons hit on a photo-cathode and are converted into electrons, which are deflected by applying a time-varying electric field between two metallic plates. The deflected electrons are imaged by a micro channel plate and phosphor screen. The electrons arriving first hit the detector at a different position than the electrons arriving last. The resulting streaking image can be used to measure pulse duration and other temporal properties.

Extending the idea of a streak camera to the attosecond regime, a portion of the IR field employed to generate single attosecond pulses is used as a time-varying electric field to deflect the attosecond electron wavepacket along the energy axis. This is termed an Attosecond Streak Camera. It can be used to characterize both the intensity and phase of the attosecond pulse. The challenge of the measurement can be seen from the fact that an attosecond pulse is measured by electronics whose best time resolution is no better than a few nanoseconds, a difference of nine orders of magnitude. This is the superiority of attosecond streak camera.

The attosecond pulse (XUV pulse) is converted into an electron wavepacket by focusing it onto a noble gas with a suitable ionization potential. The IR streaking field focused at the same spot applies a momentum shift to the electron wavepacket proportional to the vector potential of the streaking field. A spectrogram is obtained by varying the delay between the attosecond pulse and the IR pulse. Intensity can be obtained from the spectrogram when the delay is very large between the attosecond pulse and the IR pulse, while phase is encoded in the spectrogram and can be extracted using FROG-CRAB or PROOF.

The experimental setup of the attosecond streak camera we developed at KLS is presented in Figure 3-1. A 780 nm, ~8 fs, 850 μJ pulse from the KLS laser system compressed by a neon filled hollowcore fiber is split into 80% and 20% using a thin broadband beamsplitter, termed the XUV leg and the IR leg, respectively. The 80% beam in the XUV leg is focused into a 1mm long gas cell by a 375 mm focal length silver concave mirror after passing through DOG/GDOG optics. A single attosecond pulse is produced due to the elliptically varying

DOG/GDOG pulse, a process discussed in much detail in Chapter 2. A 200 nm aluminum filter is used to filter the driving IR pulse from the attosecond pulse, which after passing through a hole in the mirror is focused by an inner broadband Mo/Si multi-layer mirror (developed by NTT-AT Japan, reflectivity can support ~100 as pulse) with a 250 mm focal length onto a 50 μm diameter metallic gas jet. In the IR leg, 20% of the beam, after going through a delay stage, passes through a 400 nm focal length fused silica lens on a 5-axis pico motor stage, which can be used for fine spatial overlap of the IR leg and can change the astigmatism by tilting the lens. The divergence of the IR beam is made identical to the divergence of the beam in the XUV leg. The IR beam is reflected from the holed mirror and made concentric with the attosecond beam i.e. the inner part is the attosecond beam and the outer annular part is the IR beam. The outer IR beam shines on an annular silver concave mirror with a 250 mm focal length and is focused on the same spot as the attosecond pulse on the gas jet. A 45^{o} mirror with PZT (lead zirconate titanate) is used after the beamsplitter to introduce fine delay in the XUV leg, and a delay stage after the beamsplitter is used to introduce a coarse delay in the IR leg. To keep the delay between the two legs constant and stable, a green beam from a pump laser is co-propagated with the IR beam and is used to generate fringes in a Mach-Zehnder interferometer.

The attosecond pulse is converted into an electron wavepacket at the gas jet and is momentum shifted by the IR streaking beam. The momentum shifted electron wavepacket is collected by a conical electrode into an electron time-of-flight setup and the energy of the electron wavepacket is analyzed. The delay between the streaking pulse and the attosecond pulse is controlled by a three-axis PZT stack (manufactured by PI) on which the Mo/Si mirror is mounted. The voltages on the three axes of pzt stack are applied separately to make sure that the XUV spot stays overlapped with the IR spot. Both beams after focusing at the gas jet are collected by a mirror and refocused using a 50.8 mm diameter 201 mm focal length lens and imaged by a CCD camera with a microscope objective. To calibrate the 3-axis pzt movement, a weak IR beam is shone on the Mo/Si mirror and the beam spot is monitored on the CCD camera while voltage is applied to all the three axes separately. Three polynomials are fitted with the z-position of the XUV spot as the x-axis and the applied voltage on the PZT axis as y-axis.

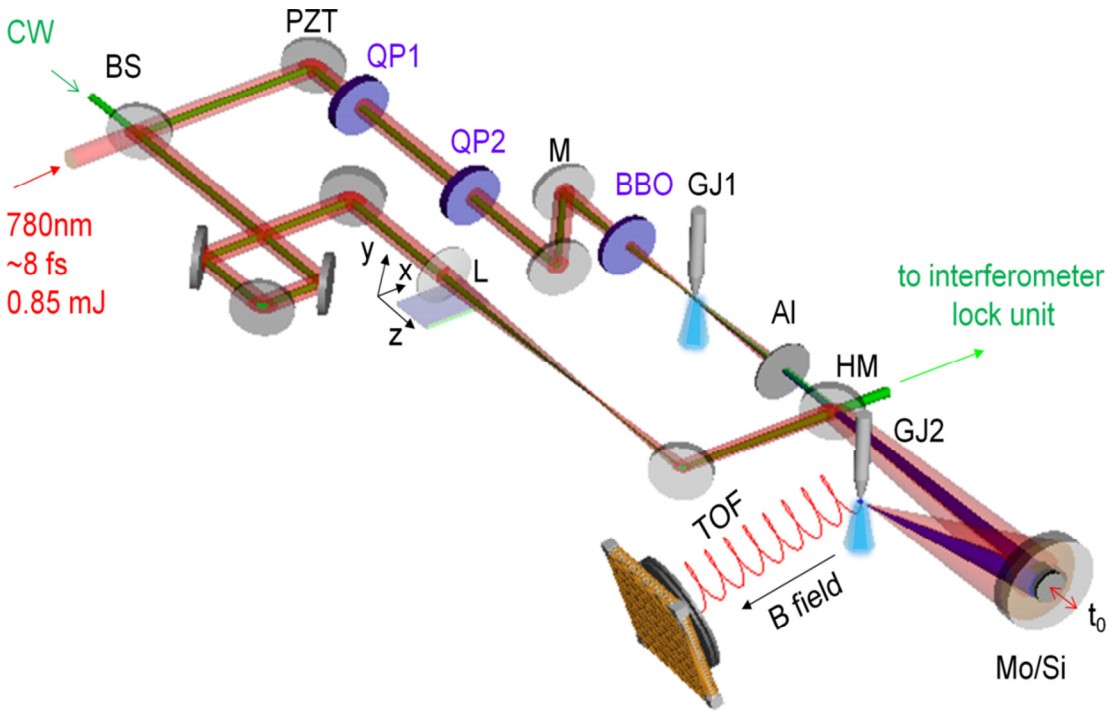

Figure 3-1 Schematic of the attosecond streak camera setup. The incoming laser beam is split into XUV and IR legs by an 80/20 broadband beamsplitter(BS). 80% goes in the XUV leg and reflects off a 45^{o} mirror with PZT, then passes through the 1st (QP1) and 2nd (QP2) quartz plates. It is focused by a 375 mm focal length concave mirror (M), passes through a BBO to generate weak SHG and then focused in a 1 mm long gas cell (GJ1) to produce a single attosecond pulse. The pulse is filtered from the driving laser by a 200 nm aluminum filter (Al) and transmited through the hole of a holed mirror (HM) and focused by a 250 mm focal length Mo/Si mirror into a gas jet (GJ2). 20% from the beamsplitter goes through a delay stage and is focused by a lens (L) to match the divergence with the attosecond pulse is reflected from the holed mirror (HM) to become concentric with the attosecond pulse in the XUV leg and focused into gas jet (GJ2) by a 250 mm focal length silver coated annular outer mirror. The electron wavepacket produced at the gas jet is collected and analyzed by a position sensitive time-of-flight electron spectrometer [1].

The green beam is combined with the IR beam in the beamsplitter, and after passing through the same optics, it separates from the IR beam at the holed mirror. The setup of the interferometer lock unit is presented in Figure 3-2. Another holed mirror (HM) is used to separate the inner and outer beams from the IR and XUV legs, respectively. Since the green beam in the XUV leg passes through several waveplates (DOG/GDOG optics) and its polarization is rotated arbitrarily, a halfwave plate is used to match the polarization with that of the IR leg. Additionally, the intensity of the IR leg is adjusted using a variable ND-filter (VND) to balance it with that of the XUV leg. The two beams are combined at the beamsplitter (BS) and circular fringes in the overlapping region are magnified by a lens. A combination of an adjustable slit and photodiode (PD) is used to generate the feedback signal for the interferometric lock. A PID controller with suitable P and I gain is used to generate a control signal from the feedback signal and is fed to the PZT on the 45^{o} mirror in the attosecond streak camera after the beamsplitter in the XUV leg.

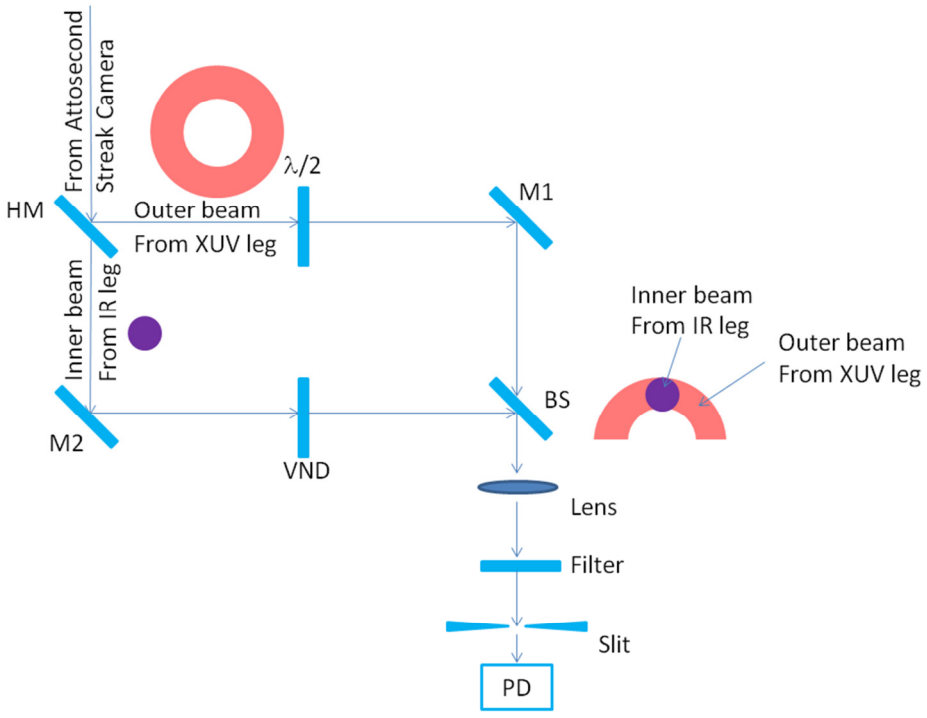

Figure 3-2 Schematic of Mach-Zehnder interferometer to lock the delay between the IR and XUV legs in the attosecond streak camera.

Mo/Si multilayer mirror

A broadband Mo/Si multi-layer mirror is used to focus the attosecond pulse at the gas jet. It consists of very thin alternate layers of Mo and Si, with the thickness of each layer between 10 and 20 nm. Intensive numerical calculations were made using a genetic algorithm prior to manufacturing by NTT-AT in Japan to adjust the thickness of each layer to give us a custom reflectivity and phase. The main object is to achieve maximum bandwidth, and the chromosome of the genetic algorithm was the thickness of each layer. The mirror when manufactured in 2006 was state of the art and supported ~100 as pulses. The reflectivity and phase of the mirror is presented in figure 3-3. This puts an upper limit on the pulse duration that could be characterized by this setup. Another mirror with bandwidth to support ~55 as was later manufactured by NTT-AT in 2009 and we plan to use it in our future experiments.

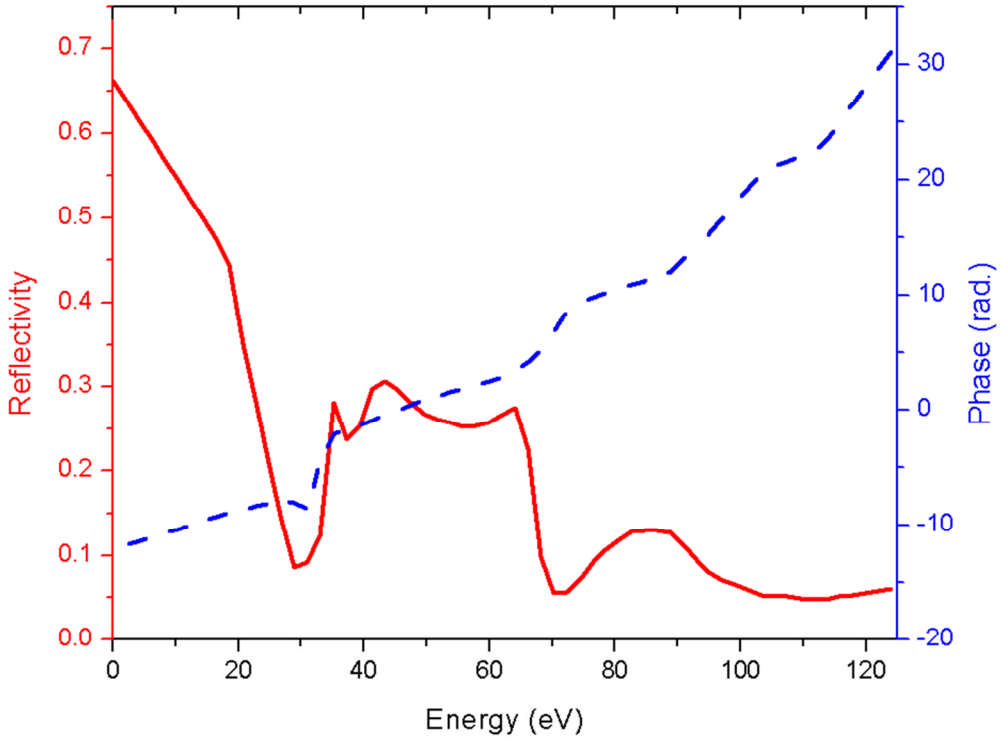

Figure 3-3 Reflectivity (red solid) and phase (blue dashed) of the Mo/Si mirror provided by the manufacturer NTT-AT Japan.

Compensation of attosecond chirp

The intrinsic chirp of the attosecond pulse was compensated by the phase of the transmission from the aluminum mirror and reflection from the Mo/Si mirror. The thickness of the aluminum mirror and the Mo/Si layer thickness were the knobs which were used to achieve nearly flat phase of the attosecond pulse at the gas jet. However, still limited by the technology involved in the manufacture of the Mo/Si mirror, a perfectly flat phase was not achieved. Luckily, the intensity of the driving laser was used to control the intrinsic chirp, which provided a further knob, but put a constraint on the maximum flux of the attosecond pulse. Figure 3-4 presents the phase of the aluminum filter and the Mo/Si mirror. The phase of the aluminum mirror was calculated from scattering factors obtained from LBL [2], while the phase of the Mo/Si mirror was obtained from NTT-AT. Note that within the transmission band (as indicated in figure 3-4) of the aluminum filter, the phase from aluminum is negative, while the Mo/Si mirror phase switches sign at ~45 eV.

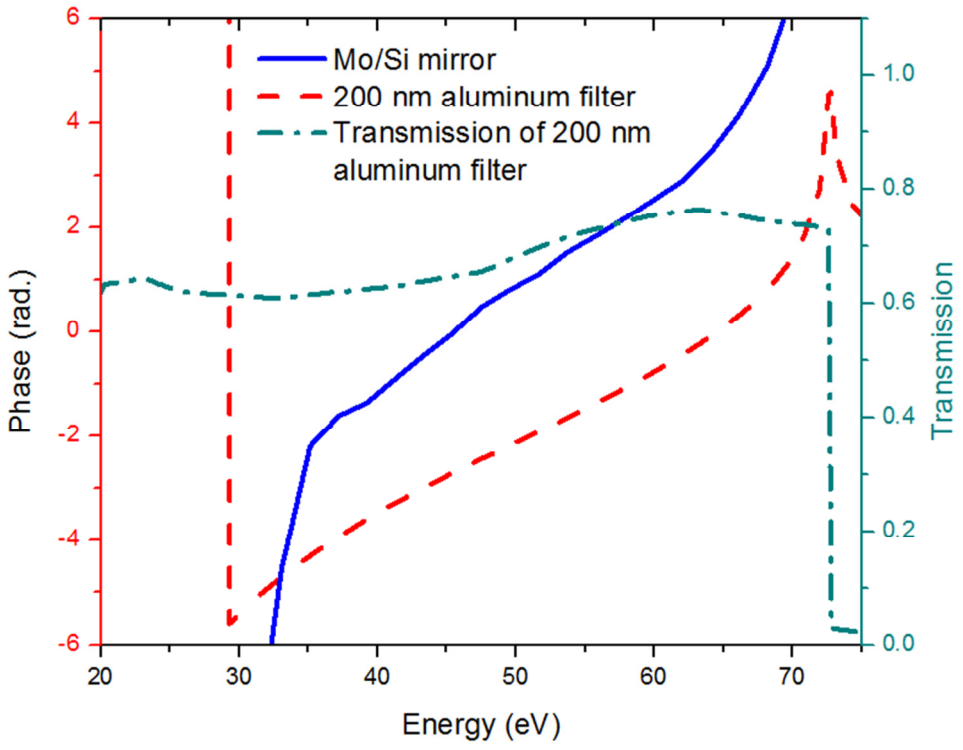

Figure 3-4 Phase from the Mo/Si mirror (blue solid) and the aluminum filter (red dashed), and transmission (cyan dot-dashed) of the aluminum filter. Data for the Mo/Si mirror

provided by NTT-AT, while the phase and transmission for the aluminum filter is calculated from the scattering factors provided by Henke et al. [2].

Temporal and spatial overlap in attosecond streak camera

To obtain spatial overlap between the XUV and IR spot focused at the gas jet, the aluminum filter is removed and the IR beam is shone on both the inner and outer mirrors. Special care is taken to keep the IR beam weak to prevent the Mo/Si mirror from being damaged. The Mo/Si mirror is fixed on a 3-axis pzt stack, which is mounted on a 3-axis pico-motor actuated kinematic mount. Prior to spatial overlap, the inner beam was blocked and the vector position of the outer streaking beam was adjusted so as to achieve minimum astigmatism. This step is critical to get optimum spatial overlap. For coarse spatial overlap, both beams were observed by the CCD camera and their position was adjusted by moving the pico-motors.

Once coarse overlap was achieved, for coarse time overlap the delay stage in the IR leg was scanned until circular fringes were observed on the CCD camera. The IR beam was then blocked and the XUV beam was used to generate an attosecond pulse train (by setting the DOG/GDOG optics to the linear position) in the gas cell and high harmonics were obtained by the electron time-of-flight setup, as presented in Figure 3-5(a). For fine time overlap, the IR beam is then unblocked and the delay stage in the IR leg is scanned until sidebands appear between the harmonic peaks with 50% of the height of the harmonic peaks. Sidebands are shown in Figure 3-5(b). The intensity of the IR leg is reduced slightly using a variable ND filter in the IR leg and sidebands are again made 50% of the peak height by adjusting the delay stage. The process is repeated iteratively until the IR beam is the weakest below which sidebands can no longer be made 50%. This is done to overlap the peak of the attosecond pulse with the peak of the IR pulse. For fine spatial overlap, the IR beam intensity is further reduced and pico-motors in the 5-axis stage were scanned until the sidebands become 50%. This process is also repeated iteratively until the IR beam is the weakest below which sidebands can no longer be 50%. To get good streaking, fine adjustment of temporal and spatial overlap is extremely critical.

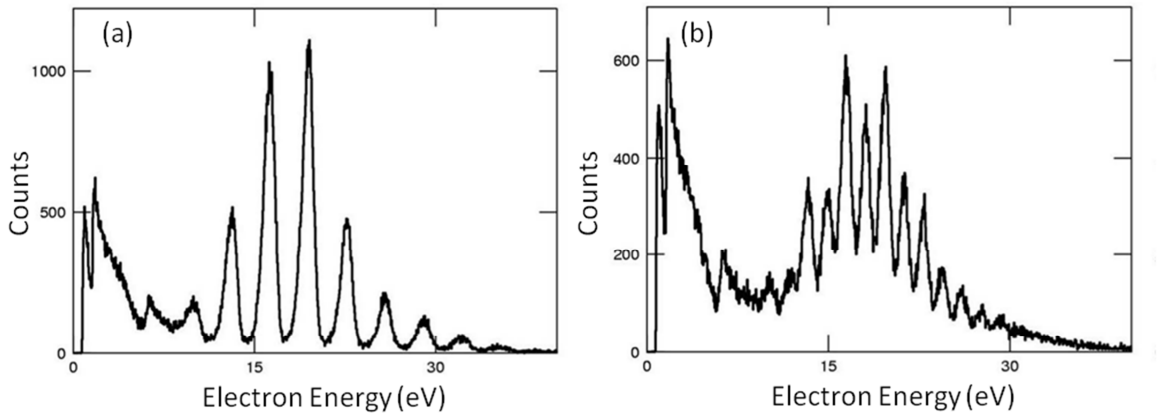

Figure 3-5 (a) Odd orders of high harmonics generated by the electron time-of-fight spectrometer in the attosecond streak camera from the XUV leg only. (b) Sidebands generated between odd order harmonics by the momentum shift provided by the streaking laser in the IR leg.

Side band generation & RABITT trace

Once temporal and spatial overlap is achieved the delay between the IR and XUV leg is scanned using the 3-axis pzt, and electron time-of-flight spectra are obtained with the CE-phase of the laser locked. The sidebands show an oscillating behavior, and the phase of the pulse train can be retrieved from the spectrogram by using the RABITT algorithm.

Generation of attosecond streaking

The RABITT spectrogram is the minimum condition for streaking. However, since it's a single photon process and streaking is a multi-photon process, it does not guarantee streaking. To get streaking we need the best CE-phase lock, interferometer lock, and spatial and temporal overlap.

To get streaking, the IR leg is first blocked and the DOG/GDOG optics are switched from the linear position to the gating position. This is done by rotating the 1st quartz plate to the 45^{o} position. A transition from discrete harmonic peaks to very broad overlapping peaks is observed in the electron time-of-flight spectra. The BBO angle is then finely tuned until a broad and smooth continuum is obtained in the spectra. The IR leg is then unblocked and the delay between the IR and XUV pulses is scanned using the 3-axis pzt. To improve streaking quality, the position of the IR beam may be slightly adjusted using 5-axis pico-motors. However, a complete

coarse and fine spatial overlap along with minimization of astigmatism may be required sometimes to get the best streaking. A good CE-phase and interferometric lock is a necessary condition to get streaking.

Electron time of flight and data acquisition setup

Time of flight setup

The electron time-of-flight setup consists of a collection cone, a 300 mm long electric field free propagation region, and a position sensitive detector. A schematic of the setup is presented in Figure 3-6. The whole setup is under a known uniform magnetic field generated using a pair of Helmholtz coils and measured using a Hall probe. The detector consists of a mesh, two large area micro channel plates (MCP) in a chevron configuration, and a position sensitive delay line detector. The cone, walls of the propagation region and the mesh are set at ground potential, while the front of the MCP is set to 300 V to reject any incoming ions and provide pre-acceleration. The electrons collected by the cone are allowed to propagate in the electric field free drift region, with the slow electrons laging behind and the fast electrons leading. The electrons are pre-accelerated between the mesh and the front of the MCP and then hit the walls of the tiny holes in the MCP producing secondary electrons. Pre-acceleration increases the likelihood of secondary electron generation. The secondary electrons are accelerated towards the MCP back and in the process hit the walls of the MCP multiple times creating an avalanche of electrons at the MCP back. The electron avalanche then hits the x and y-wires of the delay line detector and electron position is deduced by the time of arrival of pulses from the electron avalanche on the four terminals of the delay line detector. The time-of-flight is obtained from the pulse obtained from the MCP front.

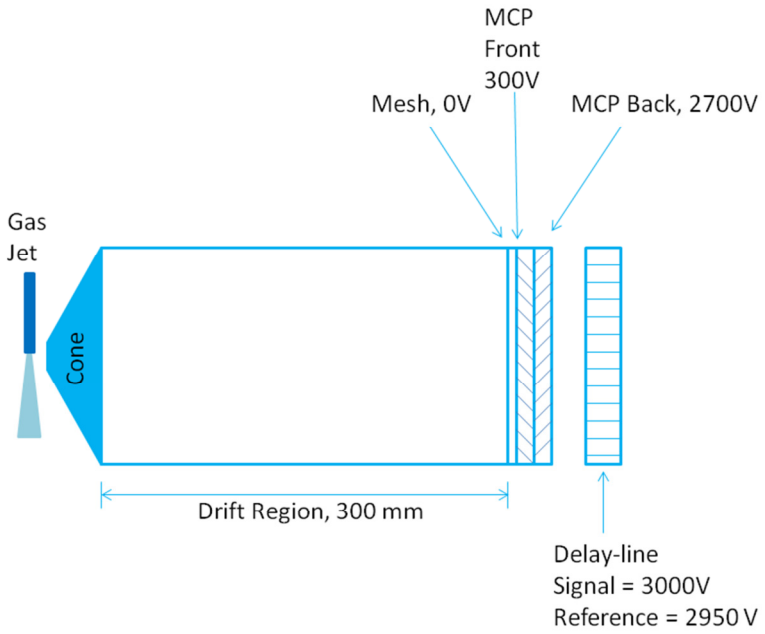

Figure 3-6 Schematic diagram of the electron time-of-fight spectrometer.

Position sensitive delay line detector

A schematic diagram of the position sensitive detector is presented in Figure 3-7(a). It consists of two copper coils orthogonal to each other. There is an air gap between the coils to prevent them from short circuiting. The entire assembly with mesh, MCPs and delay lines is presented in Figure 3-7(b).The electron avalanche from the back of the MCPs hits the coils and causes an electron pulse to flow in both directions in each coil. Depending on the position of the avalanche on the coil, the time of arrival is different on the terminals of the coil. The position of the avalanche can be determined from the difference of time of arrival on the two terminals and a gain factor which depends on the transverse velocity of electrons in the conductors. To enable efficient and noise free collection of electrons, two conductors are wound parallel instead of a single conductor. One conductor is kept slightly more positive than the other. As a result, all electrons hit on the positive conductor, which is called the signal, and the other is called the reference.

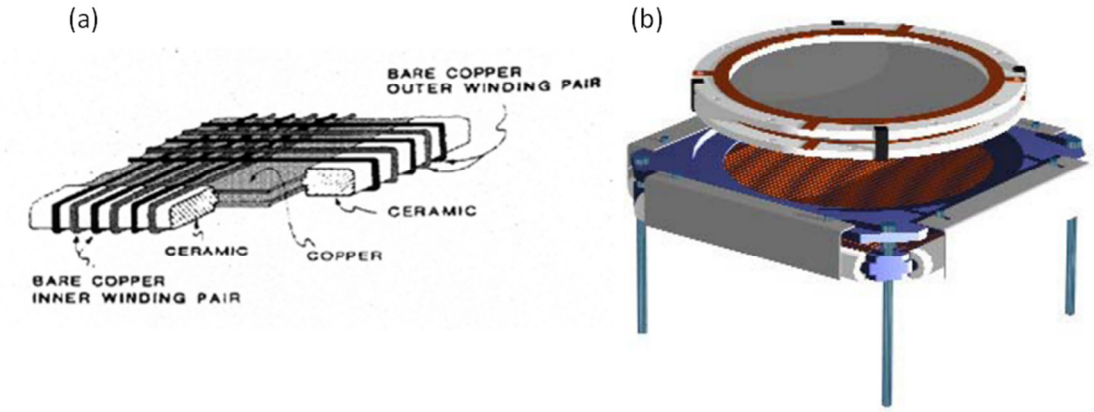

Figure 3-7 (a) Schematic diagram of the delay line detector [3]. (b) Schematic diagram of the position sensitive detector assembly with front mesh, two MCPs and delay-line detector [3].

Delay line amplifier and detection electronics

The electron pulses from the terminals of the delay line detector are amplified by quad 3-stage differential amplifiers (20+20+15 dB gain, 3mV in, 1.68 V out) after separation from the high voltage lines using capacitors and rf transformers. The delay line amplifier was designed and developed by the Electronic Design Lab at Kansas State University. The electron pulses from the MCP front are amplified by a low noise, fast timing pre-amplifier (Ortec VT-120). Four delay line and one MCP signals are converted into fast NIM pulses by five high resolution constant fraction discriminators. Additionally, the time of arrival of the laser pulse is detected by a photodiode which picks off a reflection from the 1st quartz plate. The photodiode signal is also converted into a NIM pulse by a high resolution constant fraction discriminator. This signal is called the start signal indicating the arrival of the laser pulse. The start signal is delayed by 500 ns by a delay gate generator to create the stop signal.

Time to digital converter

The start signal, MCP signal, and four position signals are digitized by a 25 ps resolution time-to-digital convertor (TDC) (CAEN V1290N). Figure 3-8 presents the timing sequence of signals. The TDC is triggered by the stop signal delayed 500 ns from the start signal (PD). All MCP and position signals are collected in between the start and stop signals.

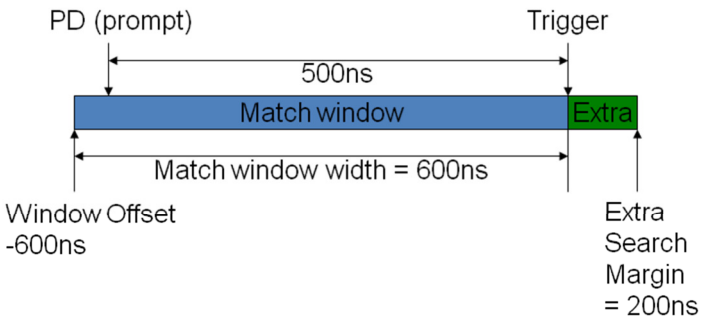

Figure 3-8 Timing diagram of the TDC trigger and settings of various TDC parameters.

The data from the TDC is transferred to an eight core computer by fiber optics. The TDC is triggered by a common stop signal, however, to increase the resolution of the data the start signal is used as a reference. This removes the delay jitter introduced by the delay generator and the TDC trigger electronics. Using this method, the only devices which contribute towards the time resolution of the system are the pre-amplifier, delay line amplifier, and constant fraction discriminator, in addition to the TDC. This results in a resolution of less than 1 ns, which is currently state of the art. Additionally, since the pair resolution of the TDC is 1 ns, two events separated by less than 1 ns are detected as a single event, which is taken care of by our resorting algorithm. The schematic of the TDC circuit is presented in Figure 3-9, which consists of delay-lines (not displayed), TDC chips, a series of buffers, ATMEGA16 microcontroller and a VME readout interface.

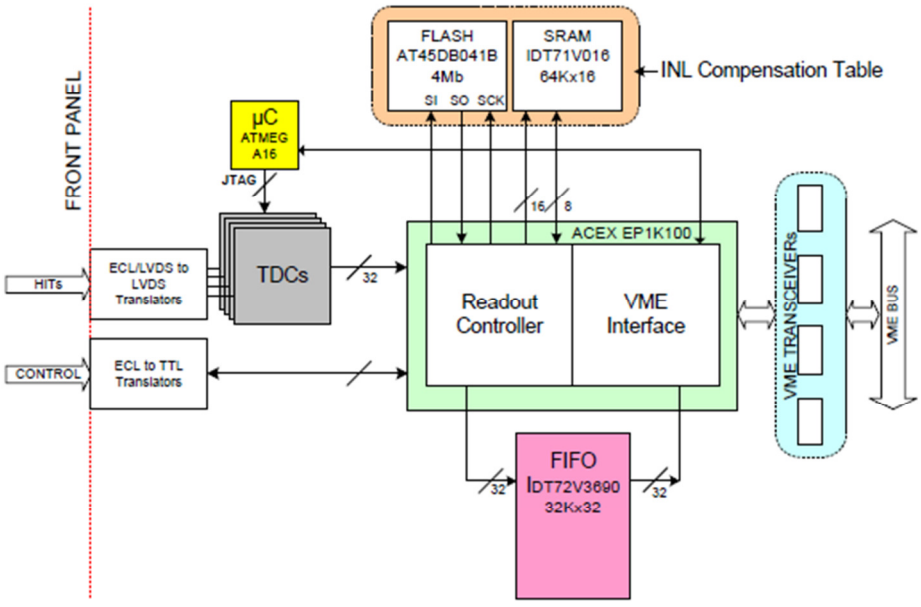

Figure 3-9 Schematic diagram of Time to digital convertor [4].

SpecTcl & sorting of data (resorting)

For processing the data, the NSCL (National Superconducting Cyclotron Laboratory) Readout and SpecTcl codes were customized. An eight core computer with a Debian Linux operating system was used. The readout code deals with the communication with the TDC over a fiber optic connection and downloads digitized data. The downloaded data are transferred into a shared memory area in the Linux operating system, which acts as a FIFO (first in first out). However, the data is read as LIFO (last in first out) from the TDC in the SpecTcl code. SpecTcl reads the data from the shared memory area and processes it into physical parameters in real time. SpecTcl can run in online and offline modes. In online mode, 70% to 90% of the data is processed and displayed in realtime. The fraction of data processed depends on the amount of resources available and the data load. In offline mode, 100% of the data is processed and data is not displayed in realtime. Both computer codes were developed by Michigan State University at NSCL for beamlines at their cyclotron facility. The codes were developed as an application framework in C/C++ and a large array of built-in functions can be overloaded to introduce customization. TCL/TK and SpecTcl scripting languages were used in these codes for further customization at the user level. For data display, the Xamine code is used within the SpecTcl framework. The application framework was customized for our needs by Kevin Carnes and our developmental effort provided significant feedback to the code developer Ron Fox at Michigan State University. I developed two versions of the readout code to communicate with a LeCroy 3377 TDC (500 ps resolution) and a CAEN V1290N (25 ps resolution). I configured the readout code to work in slave mode by remote TCP/IP connection by developing a TCL script ReadoutCallout.tcl. This script works as a server from a communications point of view. Readout can be remotely started, stopped, paused and resumed. A schematic diagram of the communication process is given in Figure 3-10(a). We developed several versions of SpecTcl code to deal with the two TDC's and introduced several other features including a display of the streaking trace. It can also be remote controlled by TCP/IP connection from the LabView program. The code works in a multi-hit mode, meaning it can process up to 8 nearly simultaneous hits on the MCP and delay line detector. This is accomplished by using a complex resorting algorithm developed primarily by Itzik Ben-Itzhak's research group. I spent a

significant part of my time in understanding the resorting process and testing it with dummy and real data event by event to develop a complete picture of the inner workings of the resorting code.

The 3-axis PZT controlling the delay between the IR and XUV pulses is controlled by a Windows based computer through a LabView program. The 3-axis PZT works in a closed loop configuration and each PZT has a built-in position sensor and an external servo controller. This results in a linear PZT response, and hysteresis is completely removed. The three servo controllers are given external setpoints by three 16-bit digital-to-analog converters from the LabView program. The LabView program logs in as a client to the readout code, but assumes full control and acts as a master. For a typical streaking spectrogram, readout code is triggered and configured to save data to a specific file for offline processing. The LabView program moves the delay stage to first delay position and starts the readout by sending a start command over TCP/IP. Each dataset is tagged with a position number provided by the LabView program. The format of a typical data packet from the TDC is presented in Figure 3-10(b). The position tag is inserted between the packet size and the header by the readout code. After a preset integration time, the LabView program pauses the readout and moves the PZT to the next position by changing the setpoint of the servo controller, readout is then resumed with a new position tag. The process is repeated until all positions are scanned. SpecTcl code processes the data from readout and sorts it into a spectrogram based on its position tag and displays a streaking spectrogram in realtime.

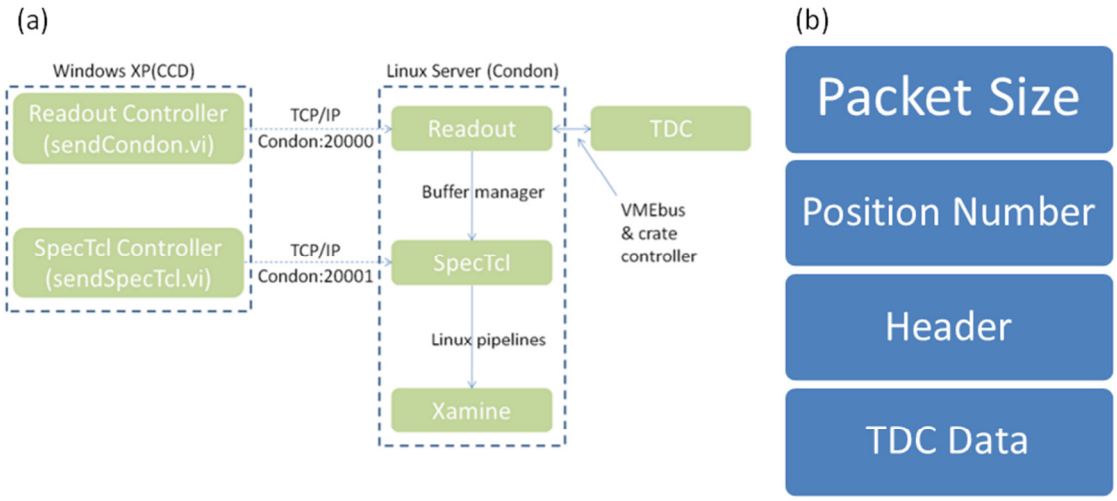

Figure 3-10 (a) Flow diagram of various software modules used to control the attosecond streak camera and transfer data to the computer. (b) Schematic of a typical data packet transfered between readout and SpecTcl via the shared memory pipeline.

The readout code negotiates with the TDC and issues commands to download data event by event. All the communication is stored in a shared memory area in the Linux which is termed a pipeline in Linux vocabulary. Within SpecTcl an Event Decoder function is fired at every trigger of the TDC. The Event Decoder extracts the MCP (t_{MCP}) and four position signals (x_1, x_2, y_1 and y_2) in units of nanosecond and subtracts the start signal (t_{start}) to give real time based on the time of arrival of the laser. This is termed as unpacking the TDC. A typical sequence of signals is presented in Figure 3-11. The time scale is reversed as the TDC is triggered by the common stop signal and data is read as LIFO (last in first out). The photodiode (PD), MCP, delay line up (U), down (D), left (L) and right (R) signals are converted into time signals with units in ns as follows:

$$t_{MCP} = MCP - t_{PD}, \quad 3.1(a)$$

$$t_U = U - t_{PD}, \quad 3.1(b)$$

$$t_D = D - t_{PD}, \quad 3.1(c)$$

$$t_L = L - t_{PD}, \quad 3.1(d)$$

$$t_R = R - t_{PD}. \quad 3.1(e)$$

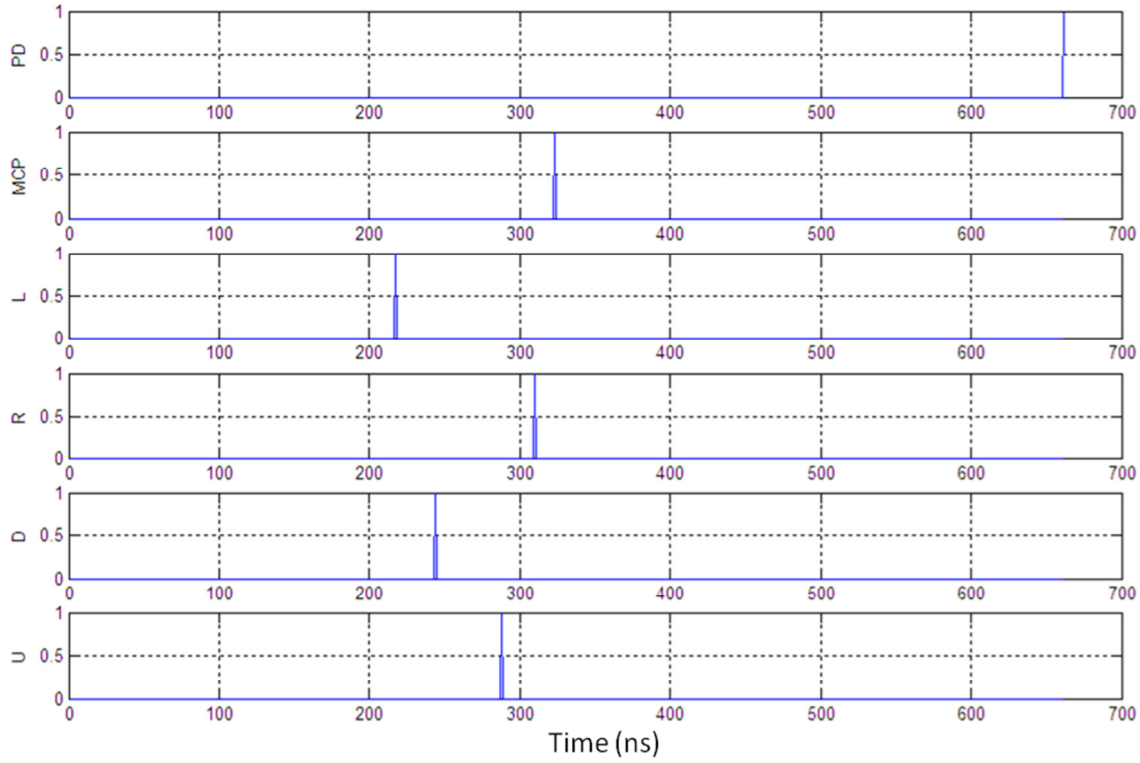

Figure 3-11 Timing diagram showing a typical sequence of signals downloaded from the TDC by Readout and SpecTcl. The data read by SpecTcl from the shared memory pipeline are last in first out (LIFO).

We define a parameter timesum, which is the time required by an electron pulse to go from one terminal of the coil to the other:

$$t_{sumx} = (t_{MCP} - t_L) + (t_{MCP} - t_R) = 2t_{MCP} - t_L - t_R, \quad 3.2(a)$$

$$t_{sumy} = (t_{MCP} - t_D) + (t_{MCP} - t_U) = 2t_{MCP} - t_D - t_U. \quad 3.2(b)$$

Ideally this should be a fixed number, but it varies due to self and/or mutual inductive and capacitive impedance of the coils. However, this variance is typically small and can be considered fixed within small standard deviations x_{SD} and y_{SD} for x and y respectively. We use this fact to our advantage and use it to sort our timing signals and reconstruct missing signals. The fixed timesum t_{xesum} and t_{yesum} is provided by the user for x and y respectively. If only one electron hits the detector at a time, it is easy to associate the position signals with the MCP signal. However, in a multi-hit scenario multiple electrons hit the detector at multiple positions in a very short period of time and it becomes very difficult to associate the four position signals with the MCP signal. The resorting code takes care of this problem for up to 8 hits at a time. All permutations are created for the MCP and position signals and they are checked against a

criteria. If a certain permutation satisfies the criteria it is accepted otherwise, it is rejected. Firstly, all the signals are tested against the XYsd test and the detector area test. The XYsd test is as follows:

$$(t_L + t_R + t_{xesum}) - (t_U + t_D + t_{yesum}) < (x_{SD} + y_{SD}). \quad 3.3$$

From equation 3.2(a) and (b), we get:

$$(2t_{MCP} - t_{sumx} + t_{xesum}) - (2t_{MCP} - t_{tsumy} + t_{yesum}) < (x_{SD} + y_{SD}), \quad 3.4$$

$$(t_{xesum} - t_{sumx}) - (t_{yesum} - t_{tsumy}) < (x_{SD} + y_{SD}). \quad 3.5$$

Thus XYsd tests the signal and makes sure the actual timesum is close to the user supplied timesum within the standard deviation. Figure 3-12 plots t_{sumy} as a function of t_{sumx} and all the data is checked if it is within the rectangle defined by x_{SD} and y_{SD}.

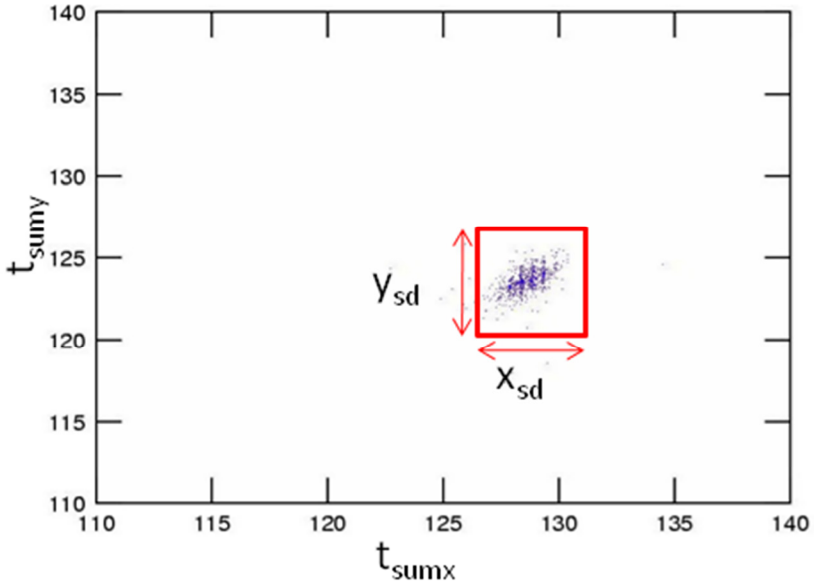

Figure 3-12 Histogram of data points captured during a typical electron time-of-fight operation. Data points within the red box satisfy the XYsd criterion, while data outside the red box is rejected.

The second test checks if the position of the event is on the detector area and is as follows:

$$(t_L - t_R)^2 + (t_U - t_D)^2 < 4\left(\frac{r_{det}}{Min(G_x, G_y)}\right)^2, \quad 3.6$$

where r_{det} is the detector radius, and G_x and G_y are the transverse electron velocities along the x and y coils. Next, the timesum of the permutations is checked against user supplied timesum, and x_{SD} and y_{SD}. These are called the Xsd and Ysd tests and are given as:

$$|t_{xesum} - t_{sumx}| < x_{SD}, \quad 3.7(a)$$

$$|t_{yesum} - t_{sumy}| < y_{SD}. \quad 3.7(b)$$

In Figure 3-13 (a) and (b) t_{sumx} and t_{sumy} are plotted as a function of x and y, respectively, and data points are checked within the regions defined by t_{xesum} & x_{sd} and t_{yesum} & y_{sd}.

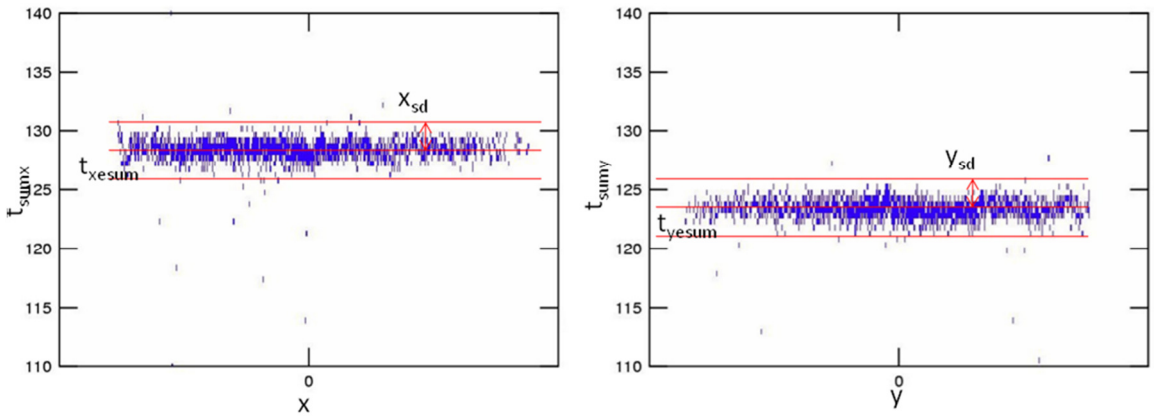

Figure 3-13 Timesum as a function of detector position. The data points within the region defined by timesum and its standard deviation satisfy the Xsd and Ysd tests.

Next, an attempt is made to recover signals that satisfy the XYsd and detector area tests, but fail the Xsd and Ysd tests, by taking one of the missing signals and reconstructing it with the user supplied timesum and its standard deviation, called 1-missing reconstruction. First, the MCP signal is assumed missing and is reconstructed as follows:

$$t_{MCP} = \frac{[(t_L+t_R+t_{xesum})+(t_U+t_D+t_{yesum})]}{4}. \quad 3.8$$

Next, position signals are attempted one by one. They are reconstructed as follows:

$$t_L = (t_{MCP} - t_R - t_{xesum}) + \frac{(t_U+t_D+t_{yesum})}{2}, \quad 3.9(a)$$

$$t_R = (t_{MCP} - t_L - t_{xesum}) + \frac{(t_U+t_D+t_{yesum})}{2}, \quad 3.9(b)$$

$$t_D = (t_{MCP} - t_U - t_{yesum}) + \frac{(t_L+t_R+t_{xesum})}{2}, \quad 3.9(c)$$

$$t_U = (t_{MCP} - t_D - t_{yesum}) + \frac{(t_L+t_R+t_{xesum})}{2}. \quad 3.9(d)$$

After resort all the position signals are associated with time signals and the position is calculated in units of millimeters as:

$$x = G_x\left(\frac{t_R-t_L}{2} - t_{x0}\right), \quad 3.10(a)$$

$$y = G_y\left(\frac{t_U - t_D}{2} - t_{y0}\right), \quad 3.10(b)$$

where G_x and G_y are transverse velocities of the electrons along the x and y coils, and t_{x0} and t_{y0} are calibration parameters used to make events centered on the detector origin. If the events are not centered on the detector origin the energy resolution is reduced. The time of flight is calculated in units of nanoseconds as follows:

$$t_{tof} = t_{MCP} - t_0, \quad 3.11$$

where t_0 is initial time and is used as an energy calibration parameter. Spatial momenta in atomic units are calculated as:

$$p_x = \frac{10^6}{p_{au}} m\omega\left(\frac{x/c - y}{2}\right), \quad 3.12(a)$$

$$p_y = \frac{10^6}{p_{au}} m\omega\left(\frac{y/c - x}{2}\right), \quad 3.12(b)$$

where ω is the angular frequency of the electron gyration in the magnetic field and is calculated from the applied magnetic field by Helmholtz coils; p_{au} is a constant to convert momentum into atomic units and is equal to 1.993×10^{-24} ; m is the mass of electron, and the constant $c = tan\left(\frac{\omega\, t_{tof}}{2}\right)$. More important parameters are the perpendicular (transverse) and parallel (longitudinal) component of momentum, which are calculated in atomic units as:

$$p_\perp = \frac{10^6}{p_{au}} m\omega\left(\frac{r}{\left|2\, sin\left(\frac{\omega\, t_{tof}}{2}\right)\right|}\right), \quad 3.13(a)$$

$$p_\parallel = -\frac{10^9}{p_{au}}\frac{m\, S}{t_{tof}}, \quad 3.13(b)$$

where $= \sqrt{x^2 + y^2}$, which is the position of the event in cylindrical coordinates and S is the length of the electric field-free drift region between the cone and the mesh in front of the MCP. We typically use S as an energy calibration parameter. The total momentum in atomic units and energy in eV are given as:

$$p = \sqrt{{p_\perp}^2 + {p_\parallel}^2}, \quad 3.14$$

$$E = 27.2\ \frac{p^2}{2} - E_0, \quad 3.15$$

where E_0 is the energy calibration parameter. The final timesum as a function of x and y position is presented in Figure 3-14 (a) and (b), respectively, and the timesum for x and y as a function of energy is presented in Figure 3-14 (c) and (d), respectively. In Figure 3-14 (a) and (b), it is

evident that the timesum is not constant along the entire area of the detector. This is due to self and/or mutual inductive and capacitive impedance of the coils as mentioned earlier. To correct this, a multiorder polynomial is fitted from experimental data and the timesum is corrected by adding this correction polynomial to the timesum before the resorting algorithm. The amount of rejected data is reduced by the timesum correction, however its effect on energy spectra is negligible.

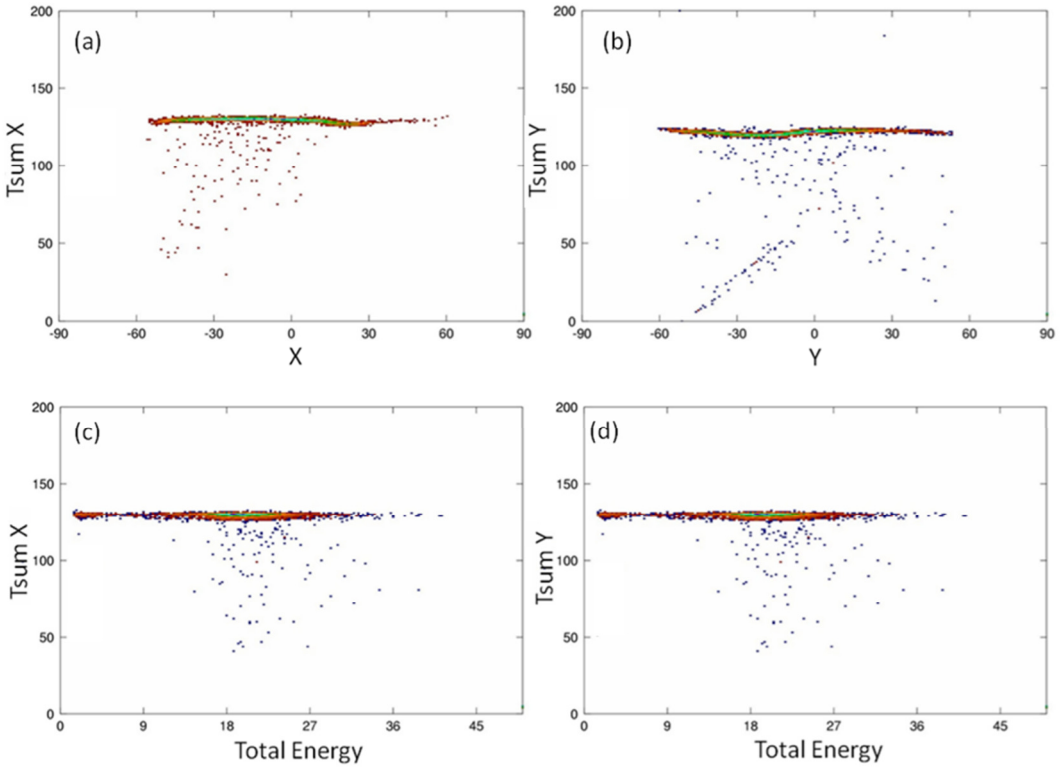

Figure 3-14 (a) and (b) timesum as a function of detector position. (c) and (d) timesum as a function of energy.

In Figure 3-15, $p_{\perp}$ is plotted as a function of $p_{\parallel}$ for high harmonics generated from neon gas and is called the wiggles spectrum. The high harmonics from 27th to 41st order are indicated. Lower orders were hard to see due to magnetic field nodes, and the half collection angle is indicated in degrees. It can be seen that the 25th harmonic has the highest half collection angle of 23^{o}, and the 25th and 39th orders have half collection angles of 18.29^{o} and 14.35^{o}, respectively.

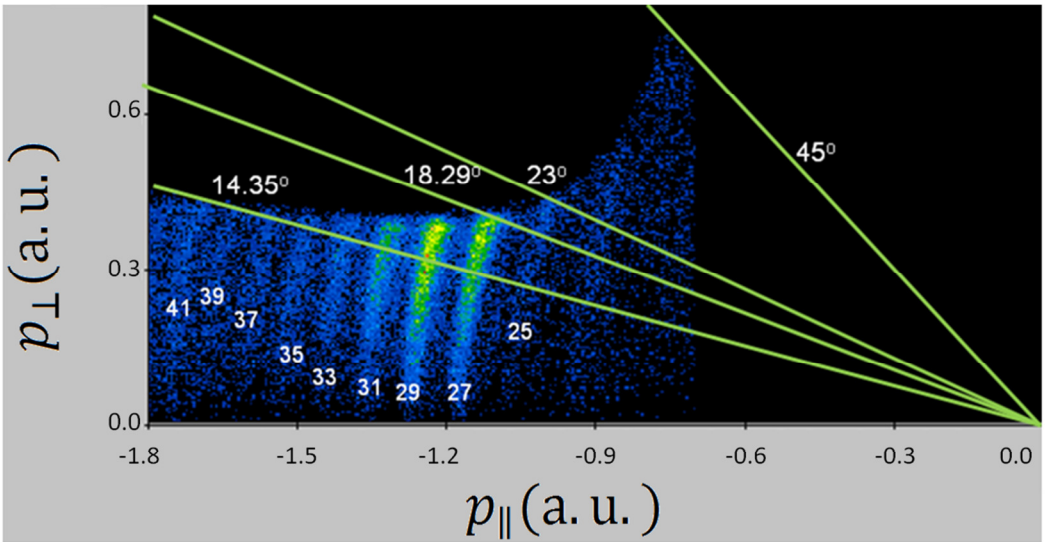

Figure 3-15 Measurement of collection angle from the parallel and perpendicular components of momenta in atomic units of the high harmonics generated from neon gas.

The wiggles spectra of various harmonic orders should be concentric with their center at zero perpendicular and parallel momentum. This concentricity depends on several parameters including t_{x0}, t_{y0} and ω, since t_{x0} and t_{y0} are used to center events on the detector and ω is used to make wiggles spectra concentric. The peak locations of the high harmonics in the energy spectra are used to calibrate energy using t_0, S and E_0. The following fitting equation is used in non-linear curve fitting in Origin for calibration:

$$S = \frac{(t_{tof} - t_0)}{1.686}\sqrt{E - E_0}, \qquad 3.16$$

where E is the energy of the high harmonic order in eV, t_{tof} is the actual time of flight in ns, and t_0, S and E_0 are fitting parameters.

Retardation potential

To study the helium 2s2p autoionization peak [5] and also measure the resolution of the electron time-of-flight spectrometer [6], a retarding potential was setup by modifying the electron time-of-flight spectrometer to provide an option for energy shift to the electrons. The experimental setup is presented in Figure 3-16. This was achieved by gluing two small meshes in front of the collection cone and one large area mesh behind the gas jet. One of the two meshes is connected to the cone by a conducting epoxy and both the cone and small mesh were kept at ground, while the other small mesh is insulated from the mesh and cone by a thin (~300 µm)

polymer insulator. The small mesh, gas jet and the big mesh were kept at a constant positive voltage. The electrons lose a constant energy equal to the voltage difference when moved between the two small meshes before entering the cone.

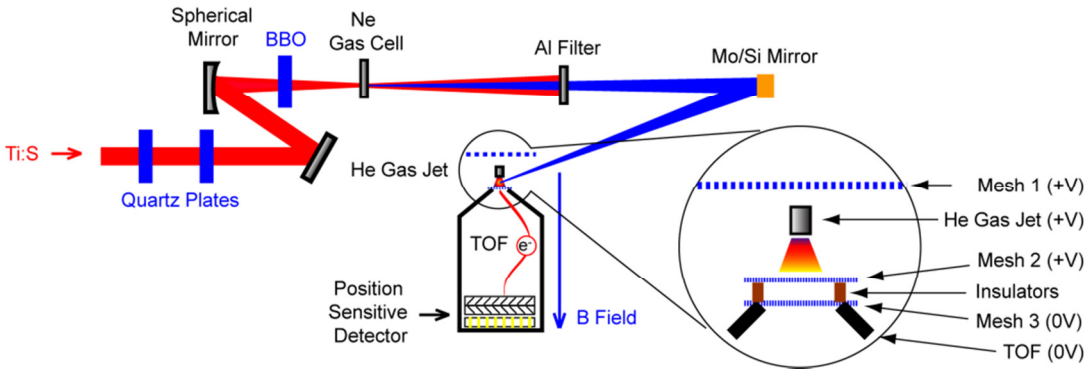

Figure 3-16 Schematic of the XUV leg of the attosecond streak camera with retarding potential [6].

Measurement of ToF resolution

In an attempt to measure the resolution of the electron time-of-flight spectrometer the helium 2s2p autoionization peak [5,6] is scanned from 10eV to 35.5 eV electron energy by applying a retarding potential at the entrance of the cone. The electron spectra are presented in Figure 3-17, and the helium autoionization peak is shifted from 35.5 eV to as low as 10eV. The autoionization peak is fitted by a Pearson type IV function to obtain the peak width. From synchrotron measurements the intrinsic line width of the autoionization peak is 38 meV [7]. Thus the resolution of the spectrometer varies from 300 meV at 10 eV to 600 meV at 35 eV as presented in Figure 3-18. The relation between energy resolution ΔE and electron energy E can be given as [6]:

$$\Delta E = \frac{2^{3/2}}{m_e{}^{1/2}} \frac{\Delta t}{S} E^{3/2}, \qquad 3.17$$

where m_e is the mass of the electron, Δt is the time resolution of the MCP and electronics and S is the length of the electric field-free drift region. It can be noted from Figure 3-18 that we did not get a good fit of this function to the experimental data. The first factor responsible for the deviation is the non-uniform magnetic field of the Helmholtz coils and the second factor is the technical difficulty of maintaining the surface of the mesh wrinkle free.

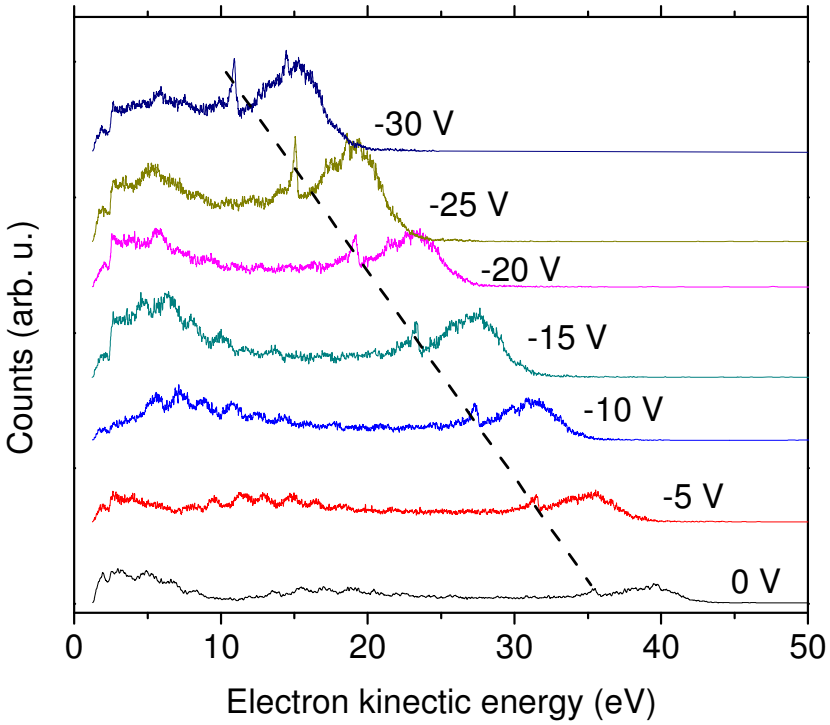

Figure 3-17 Photoelectron spectra of continuum electrons generated by a single attosecond pulse in helium with the helium 2s2p autoionization peak. The spectra are shifted towards lower energy by a retarding potential [6].

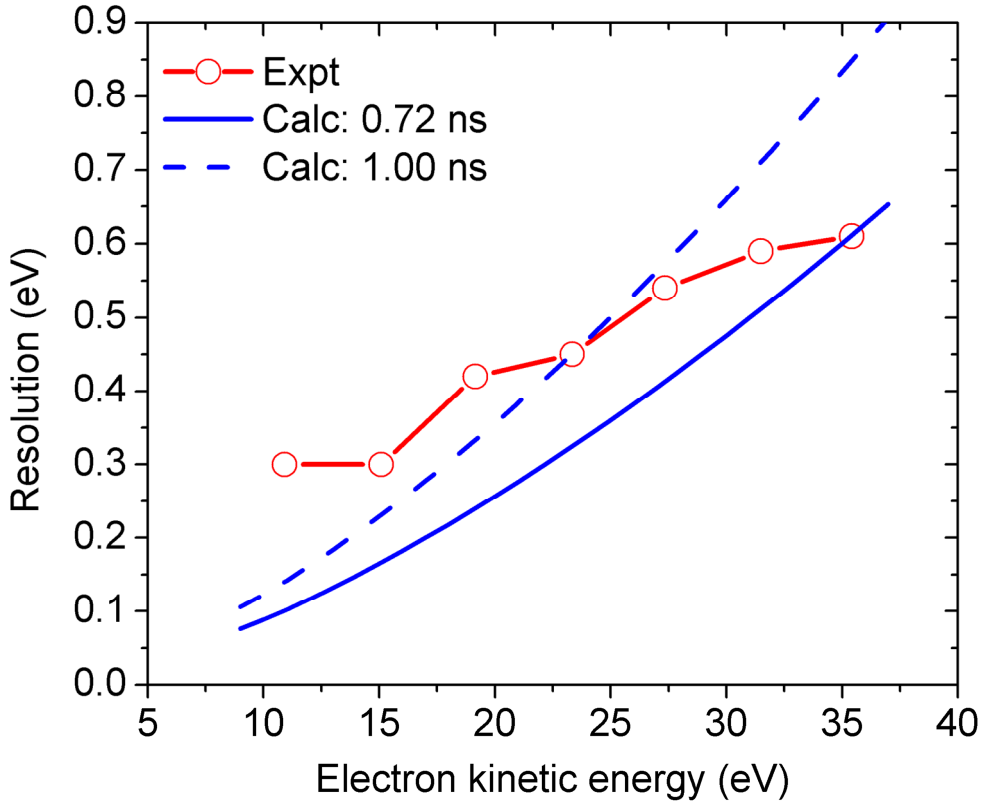

Figure 3-18 Experimentally measured resolution of the electron time-of-flight setup using a retarding potential (red circles). Calculated resolution from equation 3.17 with time resolution of 0.72 (blue continuous) and 1 ns (blue dashed) [6].

Conversion to ion time of flight

By utilizing the meshes we set up for the retarding potential and changing the voltage on the MCP and delay line, it is possible to convert the electron time-of-flight setup into a low resolution ion time-of-flight setup. The detailed schematic is presented in Figure 3-19. A linear electric field is generated between the big mesh and the small mesh in front of the cone, to guide ions produced at the gas jet into the cone. The ions see zero electric field between the cone and the mesh in front of the MCP. The ions see an accelerating potential between the mesh and the MCP front and hit the surface of the MCP producing secondary electrons, which are accelerated towards the MCP back, creating an avalanche of electrons on their way. The avalanche hits the delay-line detector and the position of the ions is measured. However, in the code we only measure the MCP signal and time-of-flight and did not process position.

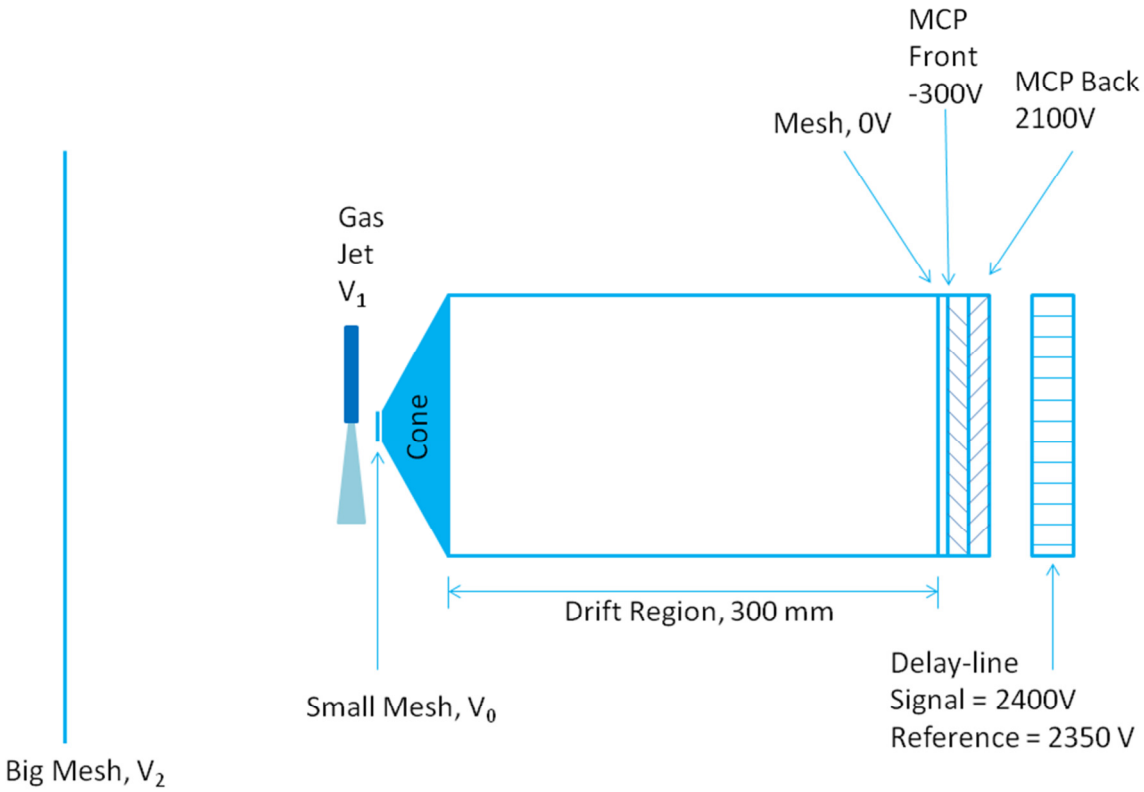

Figure 3-19 Schematic diagram of the ion time-of-flight spectrometer converted from the electron time-of-flight spectrometer by exploiting the retarding potential electrodes.

The constraint for potential on the big mesh, gas jet and small mesh is $V_2>V_1>V_0$. We set V_0 equal to zero and, scanned V_1 and V_2 for the highest count and the best resolution. The ion count increases with increasing V_2, due to the fact that collection angle of the time-of-fight setup increases. For maximum V_2 = 5000 V, the optimum voltage on the gas jet was 209 V. However, this is very sensitive to gas jet position and needs to be optimized during every run. We used argon, neon, nitrogen and krypton to calibrate the ion time-of-flight spectrometer. Their calibration curve is presented in Figure 3-20.

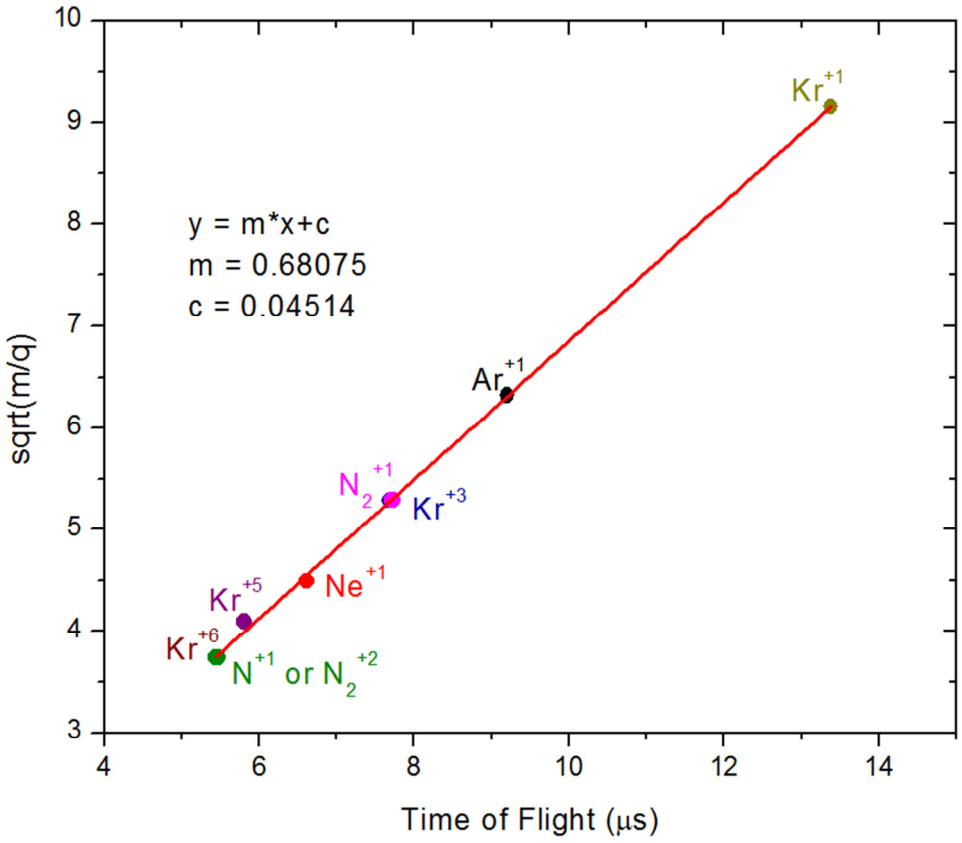

Figure 3-20 Mass to charge ratio of various ionized species from Ar, Ne, Kr and N_2 as a function of time-of-flight.

FROG-CRAB algorithm

Overview of the algorithm

The electric field of a single attosecond pulse can be given as:

$$\varepsilon_X(t) = \int_{-\infty}^{\infty} U(\omega) e^{i\varphi(\omega)} e^{i\omega t} d\omega, \qquad 3.18$$

where $U(\omega)$ is the electric field amplitude and $\varphi(\omega)$ is the spectral phase. The electric field amplitude is related to spectral intensity $I(\omega)$ by $I(\omega) = |U(\omega)|^2$. Spectral intensity can be measured easily with an XUV spectrometer. The attosecond pulses are diffracted by a grating and imaged by an MCP-Phosphor setup on a CCD camera. However, the measurement of phase is not so easy. The spectrogram obtained from the attosecond streak camera has phase encoded within it. A phase retrieval method similar to FROG (frequency resolved optical gating), used commonly to characterize the phase of femtosecond pulses, can be extended to the attosecond domain and is called FROG-CRAB (frequency resolved optical gating for complete

reconstruction of attosecond bursts). Several phase retrieval algorithms are available in the signal processing domain, but the most commonly used in FROG and FROG-CRAB is based on generalized projections and is called PCGPA (principle components of generalized projections algorithm). The electron wavepacket produced at the gas jet in an attosecond streak camera by the attosecond pulse can be given by $\varepsilon_X(t)d[\vec{p}_i(t)]$, where $d[\vec{p}_i(t)] = \langle\vec{p}_i|r|0\rangle$ is the dipole transition matrix element for an electron transition from the ground state $|0\rangle$ to the continuum $|\vec{p}_i\rangle$ and $\vec{p}_i(t)$ is the instantaneous momentum. According to Mairesse et al. [8], in an attosecond streak camera the momentum shift applied to the electron wavepacket by the dressing laser $\vec{\varepsilon}_L(t) = -\frac{\partial\vec{A}(t)}{\partial t}$ can be given in atomic units as an applied phase in 1D by:

$$\phi(t,\nu) = -\int_t^\infty \left[\vec{\nu}.\vec{A}(\acute{t}) + \frac{A^2(\acute{t})}{2}\right] d\acute{t}, \qquad 3.19$$

where $A(t)$ is the vector potential of the laser, ν is the momentum related to the vector potential, the instantaneous momentum is $\vec{p}_i(t) = \vec{\nu} + \vec{A}(t)$, and the final momentum is $\vec{p}(t) = \vec{\nu}$. The transition amplitude can be given as:

$$b(\nu,\tau) = -i\int_{-\infty}^{\infty} \varepsilon_X(t-\tau)d[p_i(t)]e^{i\phi(t,\nu)}e^{-i\left(\frac{\nu^2}{2}+I_p\right)t}\,dt, \qquad 3.20$$

where I_p is the ionization potential of the gas and the spectrogram is given by $I(\nu,\tau) = |b(\nu,\tau)|^2$. This is basically a Fourier transform of the electron wavepacket and the applied laser phase. A closer look at equation 3.20 reveals that both $d[p_i(t)] = d[\vec{\nu} + A(t)]$ and $\phi(t,\nu)$ are functions of ν and t. The momentum dependence of these terms can be removed by assuming $p(t) \to p_0$, where p_0 is the central momentum of streaked electrons. This is called the central momentum approximation, which means that the energy bandwidth of the electrons is narrow compared to their central energy [9]. Within this approximation, the spectrogram can be simplified as [10]:

$$I(\omega,\tau) = \frac{|b(\nu,\tau)|^2}{|d[p(t)]|^2} \approx \left|\int_{-\infty}^{\infty} E(t-\tau)G(t)e^{i\omega t}\,dt\right|^2, \qquad 3.21$$

where $G(t) = \frac{d[p_0+A(t)]}{d[p_0]}e^{i\phi(t)}$ is the applied phase from the streaking laser, and $E(t-\tau) = \varepsilon_X(t-\tau)$ is the attosecond field. This is quite similar to FROG and PCGPA and can be used to retrieve phase from the spectrogram.

When the laser electric field is $E_L(t) = E_0(t)cos(\omega_L t)$, under the slowly varying envelope approximation, a zero degree observation angle, and the strong field model, the applied laser phase can be approximated as:

$$\phi(t) = -\int_t^{\infty} \frac{E_0^2(t)}{4\omega_L^2} dt + \frac{\nu E_0(t)}{2\omega_L^2} cos(\omega_L t) - \frac{E_0^2(t)}{8\omega_L^3} sin(2\omega_L t). \quad 3.22$$

In PCGPA, we start with a random pulse and gating fields in equation 3.21 and generate a FROG-CRAB trace by matrix transitions to the outer product in the time domain [11] (called physical constraint) and a Fourier transform. The FROG-CRAB error is calculated by comparing with the experimental spectrogram (called intensity constraint) and new guess for the pulse and gating field is calculated by an inverse Fourier transform and singular value decomposition. The process is repeated many times until the FROG-CRAB error is minimized or the pulse and gating fields remain unchanged across iterations. The algorithm basically starts from a random point in space and alternates between physical constraint in time domain and intensity constraint in frequency domain [11]. An experimental spectrogram in Figure 3-21 (a) is compared with a reconstructed FROG-CRAB trace in Figure 3-21 (b) retrieved using PCGPA. The retrieved electric field are presented in Figure 3-21 (c), while an XUV only spectrum is compared with the spectral field in Figure 3-21 (d).

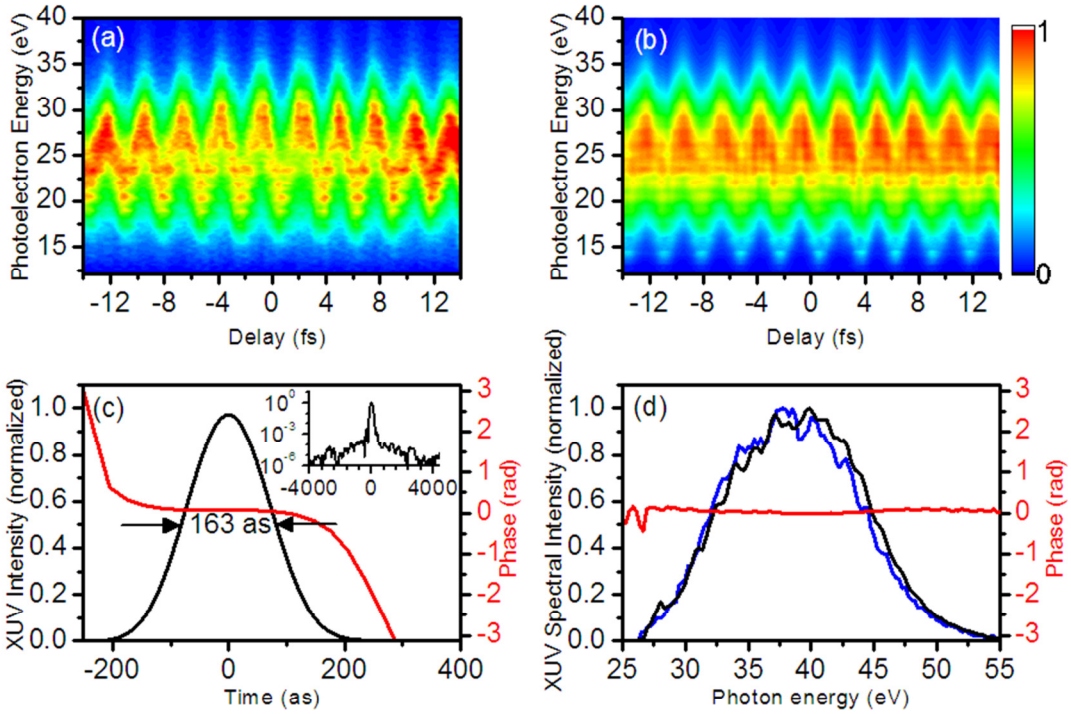

Figure 3-21 (a) Experimentally recorded spectrogram obtained using the GDOG method using neon in the gas cell and gas jet, (b) Reconstructed spectrogram using FROG-CRAB, (c) Retrieved pulse and phase, retrieved pulse with larger time range (inset) (d) Retrieved pulse in the spectral domain compared with an XUV only spectrum [12].

Theoretical simulations

To check the PCGPA based FROG-CRAB algorithm for attosecond pulse retrieval, we did a large set of theoretical simulations. Since streaking follows the vector potential of the dressing laser, the amount of streaking depends on the laser intensity. Figure 3-22 shows streaking traces for intensities of dressing lasers from $5\text{x}10^{10}$ W/cm^2 to $5\text{x}10^{14}$ W/cm^2. A low dressing laser intensity is typically desirable in the experiment, since high intensity can cause ionization from the streaking field by processes like multi-photon ionization. However, it can be seen that at $5\text{x}10^{10}$ W/cm^2 the amount of streaking is small. Based on the Rayleigh criterion, to resolve two events separated by δt in time, they must be shifted with respect to each other by at least as much as their own spectral width ΔW. When the quiver energy $U_{\mathrm{p}}(t) = E_0^2(t)/4\omega_{\mathrm{L}}^2$ is

much less than the central energy $W_0 = p_0^2 / 2$. The minimum attosecond pulse duration that can be measured is given by:

$$\delta t = \frac{T_{IR}}{2\pi}\sqrt{\frac{\hbar\omega_{IR}}{\Delta W}}, \qquad 3.23$$

where $\hbar\omega_{IR}$ is the photon energy of the streaking laser and T_{IR} is the period of the streaking laser. For a streaking laser with a central wavelength of 800 nm, to resolve a pulse shorter than 100 as, at least 28 eV of spectral width is required, which corresponds to a streaking laser intensity of $3\text{x}10^{13}$ W/cm^2 , when a central energy of 100 eV is assumed [13].

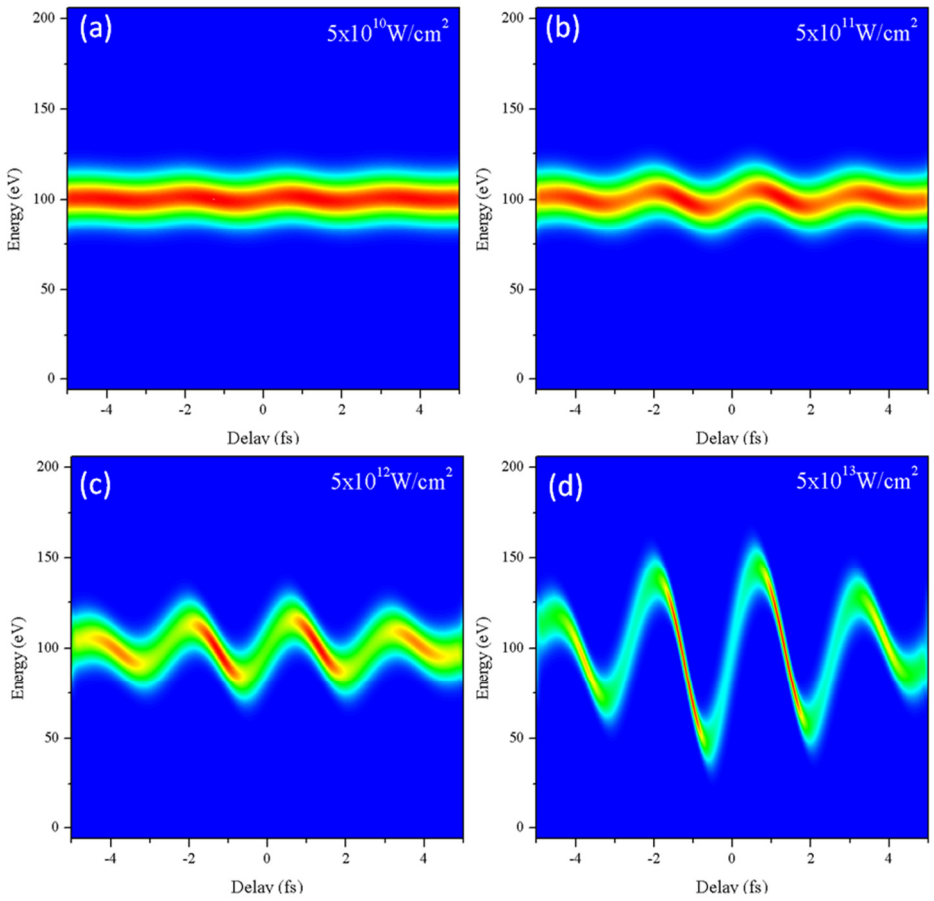

Figure 3-22 Simulated FROG-CRAB spectrogram under streaking intensities of $5\text{x}10^{10}$, $5\text{x}10^{11}$, $5\text{x}10^{12}$ and $5\text{x}10^{13}$ W/cm^2. The TL pulse duration of the attosecond pulse was 90 as with 5000 as^2 chirp, and the streaking laser pulse duration was 5 fs.

However, the retrieval of the FROG-CRAB trace from Figure 3-22 (c) with dressing laser intensity of $5\text{x}10^{12}$ W/cm^2 yielded very accurate phase as evident from Figure 3-23. This

indicates the robustness of FROG-CRAB against low streaking intensity, which is called streaking speed.

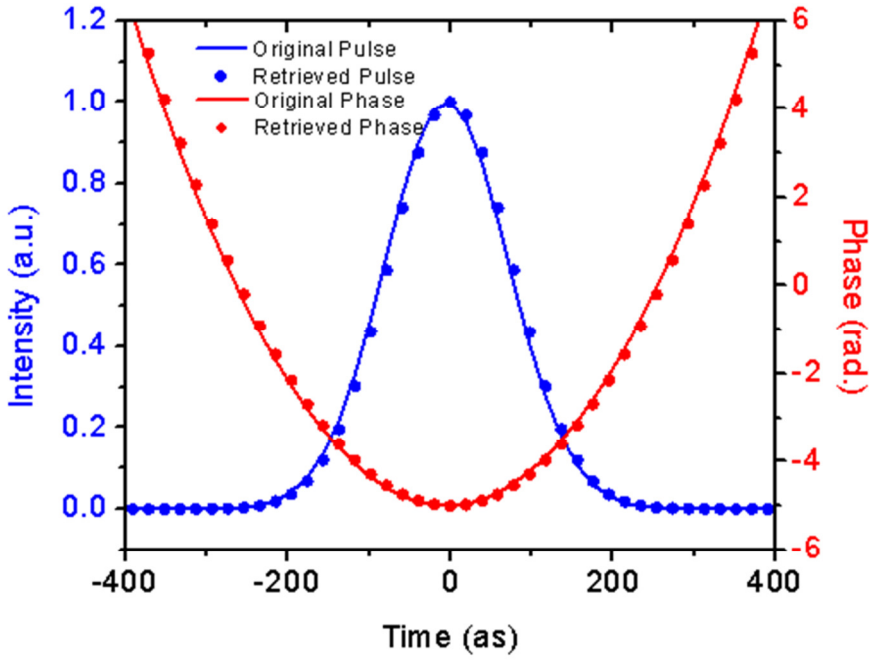

Figure 3-23 Retrieved pulse (filled circles) from the spectrogram in Figure 3-22(c) compared with the actual pulse (continuous lines) [14].

Temporal jitter between the attosecond pulse and the streaking pulse is an experimental reality, and in order to understand it we did a series of simulations with FROG-CRAB traces with different delay between the attosecond and streaking pulses, superimposing them. Retrieved attosecond pulse duration and chirp as a function of time delay jitter is compared with the actual pulse duration and chirp in Figure 3-24 (a) and Figure 3-24 (b), respectively. It can be seen that for up to 200 as delay jitter, which is around twice the pulse duration, phase can be retrieved with less than 10% error. This again proves the robustness of FROG-CRAB.

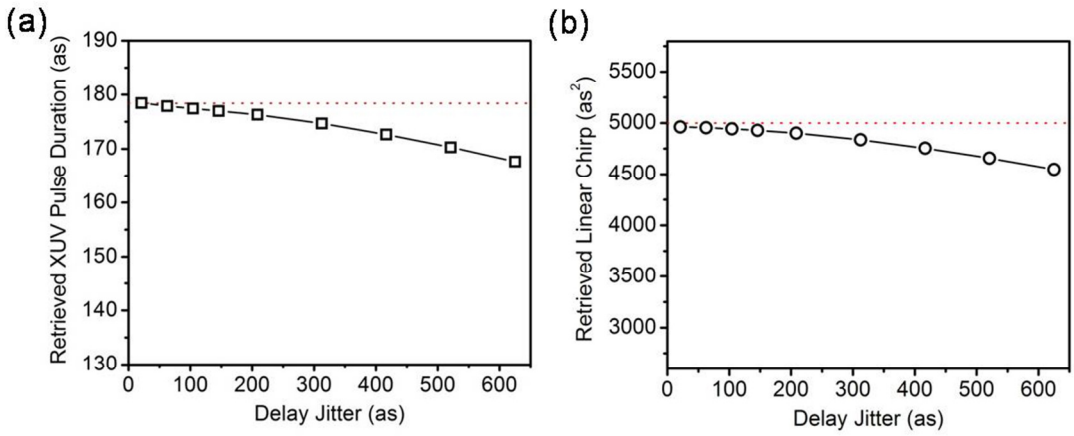

Figure 3-24 Retrieved pulse duration (squares) and chirp (circles) as a function of delay jitter compared with actual pulse duration and chirp (dashed lines) [9].

Another experimental reality is the noise added into the energy spectra in electron time-of-flight. We took a synthetic FROG-CRAB trace with the maximum pixel in the trace having 50 counts and a dressing laser intensity of 10^{12} W/cm^2, as presented in Figure 3-25 (a), and added shot noise to it. The noisy trace is given in Figure 3-25 (b) and the retrieved spectrogram is given in Figure 3-25 (c). The retrieved pulse duration is presented in Figure 3-26, and the accuracy of the retrieval is quite evident. A detailed analysis is presented in Figure 3-27 with maximum pixel 10 to 200 counts. Retrieved pulse duration and chirp are compared with the actual pulse duration and chirp in Figure 3-27 (a) and (b), respectively, for various streaking laser intensities. For streaking laser intensities of $7.5\text{x}10^{11}$ W/cm^2 and higher, a maximum pixel count of 50 or higher is enough to retrieve pulse duration and chirp within 10% error. This proves the robustness of FROG-CRAB against shot noise and allows us to reduce the integration time of the electron time-of-fight spectrometer.

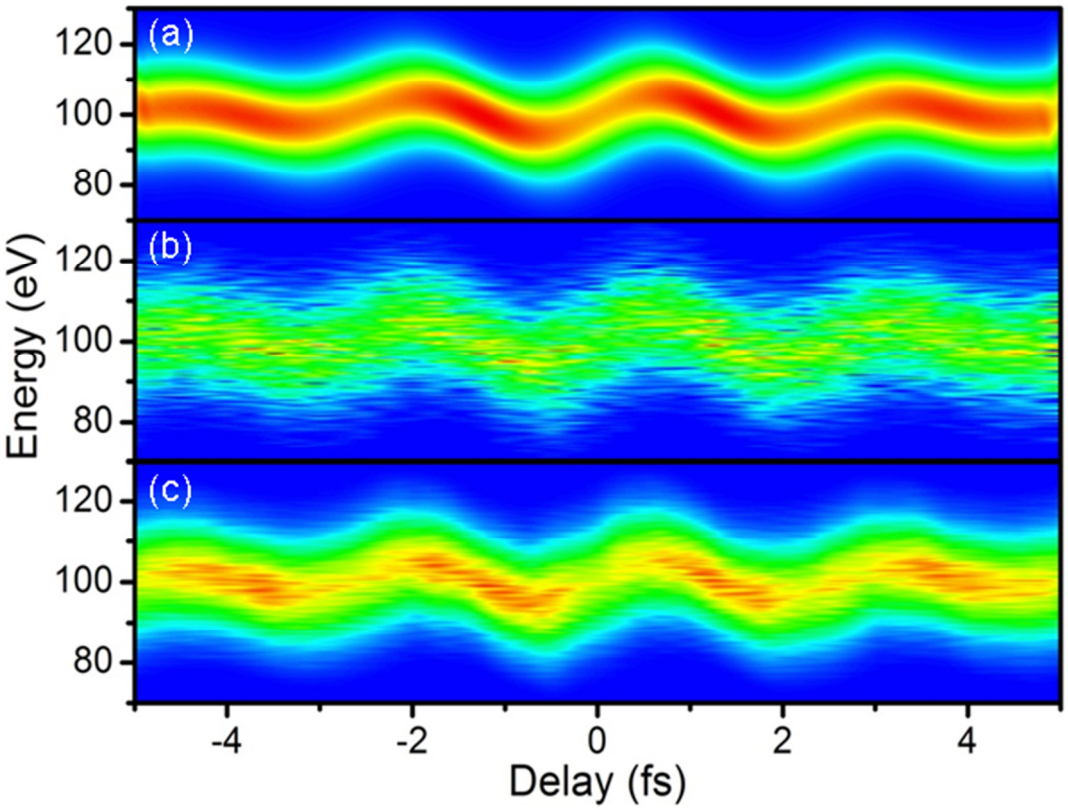

Figure 3-25 (a) FROG-CRAB spectrogram generated from an attosecond pulse with 90 as TL pulse duration and 5000 as^2 chirp streaked with a 5 fs 5x10^{12} W/cm^2 IR laser. The count of maximum pixel is 50. (b) Shot noise is added into the spectrogram, (c) Retrieved FROG-CRAB spectrogram [9].

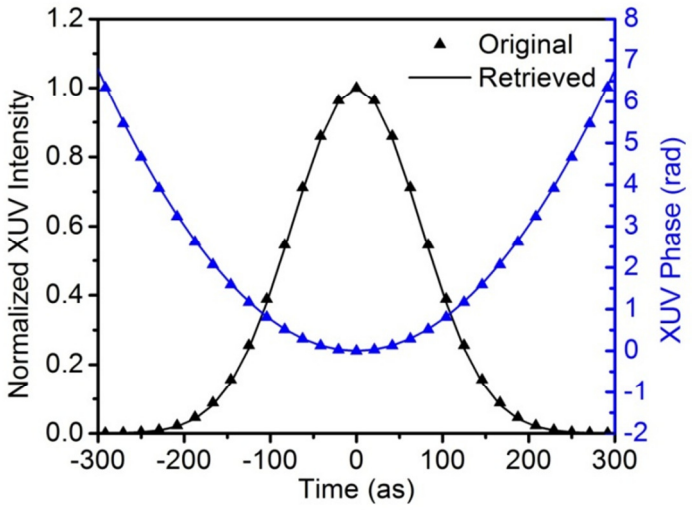

Figure 3-26 Retrieved pulse of the FROG-CRAB spectrogram in Figure 3-25 [14].

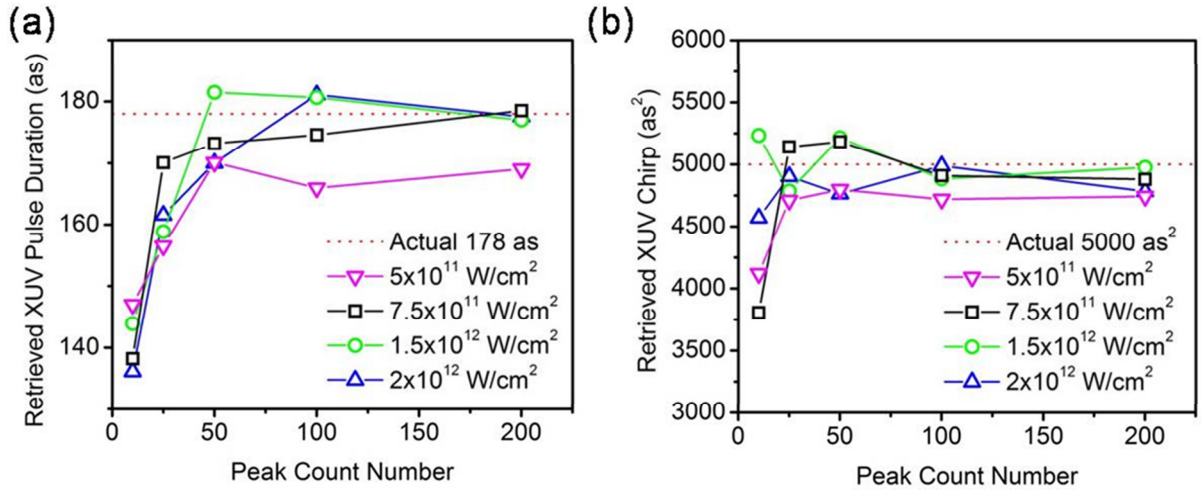

Figure 3-27 Retrieved pulse duration and chirp as a function of maximum peak count at various streaking intensities, compared to actual pulse duration and chirp [9].

To further test this against actual experimental noise, we took a streaking trace with 1 minute integration time per slice and reduced the integration time by modifying the SpecTcl code to process fewer laser events. Retrieved pulse duration as a function of maximum pixel count is plotted in Figure 3-28 (d), while retrieved intensity and phase from 60 s and 2 s integration times are presented in Figure 3-28 (a) and (b), respectively. Figure 3-28 (a) is re-plotted on a log scale and a larger temporal range in Figure 3-28 (c). The robustness of FROG-CRAB against noise is once again evident, thus reducing the amount of time to record one full spectrogram, which is experimentally beneficial, since keeping laser parameters constant for longer periods of time is difficult.

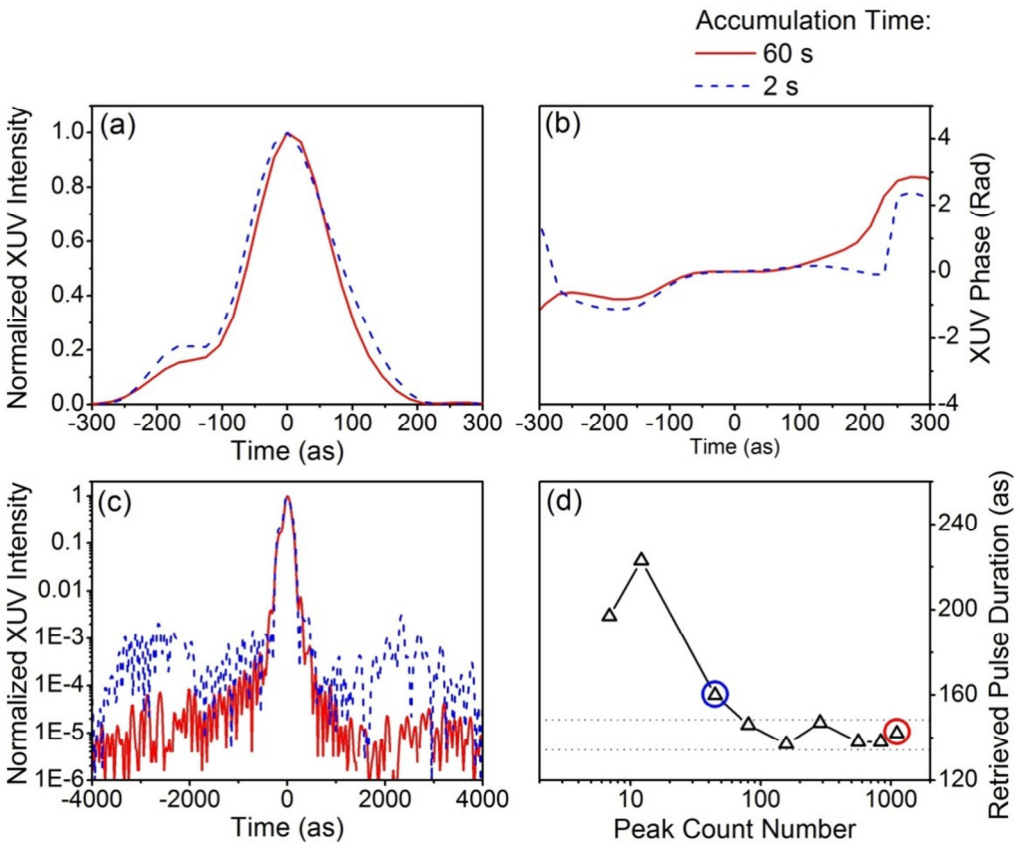

Figure 3-28 Retrieved attosecond pulse (a) from 60 s (continuous red line) and 2 s (dashed blue line) accumulation times from an experimentally recorded spectrogram, retrieved pulse in log scale (c), retrieved temporal phase (b) for 60 s (continuous red line) and 2 s (dashed blue line) accumulation time, and (d) retrieved pulse duration as a function of peak count number for different accumulation times [9].

Collection angle is another important experimental parameter. Retrieved pulse duration and chirp as functions of collection angle is plotted in Figure 3-29 (a) and (b), respectively. It can be seen that within the measured acceptance angle of our electron time-of-flight spectrometer (46^{o} from figure 3-15) the pulse duration and chirp are retrieved with less than 1% error.

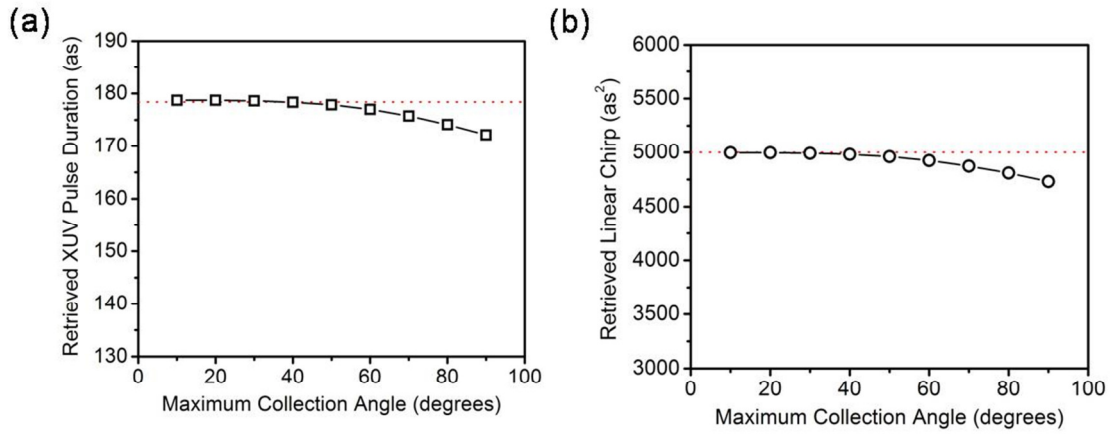

Figure 3-29 Retrieved pulse duration (a) and chirp (b) as functions of collection angle [9].

Experimental measurement

Shortest pulse with DOG

Using DOG optics the shortest attosecond pulse we were able to measure was 108 as. This is close to the allowed spectral bandwidth of the Mo/Si multi-layer mirror. The retrieved FROG-CRAB trace and attosecond pulse is presented in Figure 3-30.

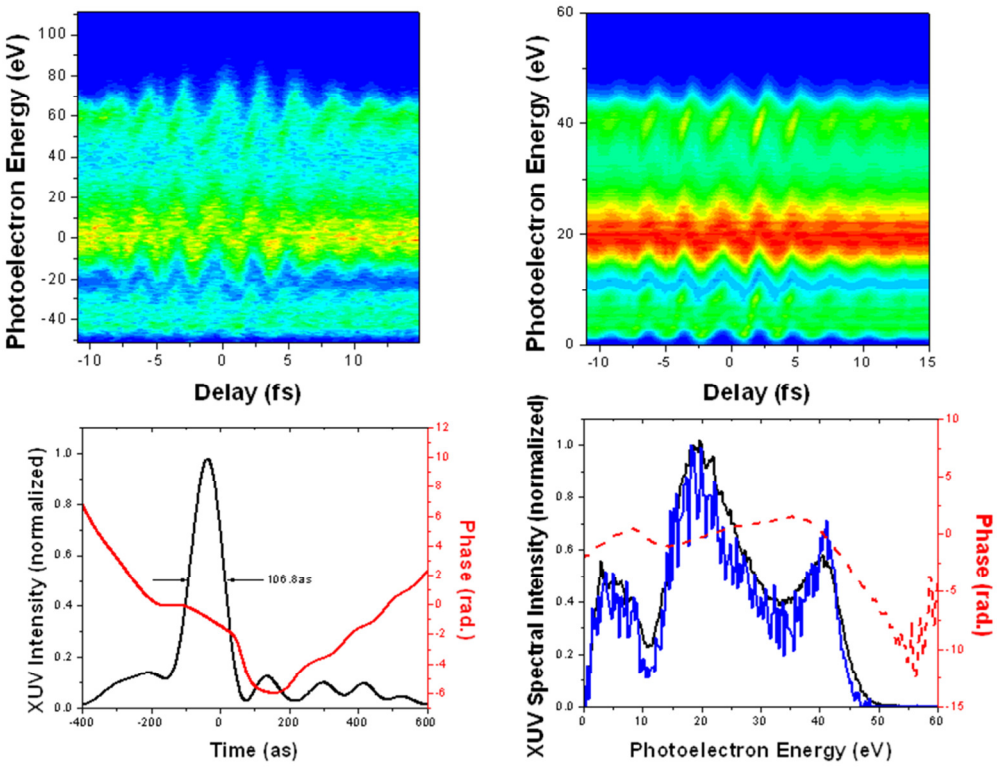

Figure 3-30 (a) Experimentally recorded spectrogram obtained using the DOG method with neon in the gas cell and the gas jet, (b) Reconstructed spectrogram using FROG-CRAB, (c) Retrieved pulse and phase, (d) Retrieved pulse in the spectral domain compared with the XUV only spectrum.

Shortest pulse with GDOG

Using GDOG the shortest pulse duration we were able to measure so far was 163 as, which is presented in Figure 3-31. We were also able to measure 148 as pulse duration, but the quality of the spectrogram was not good. The retrieved spectrogram and pulse is presented in Figure 3-32.

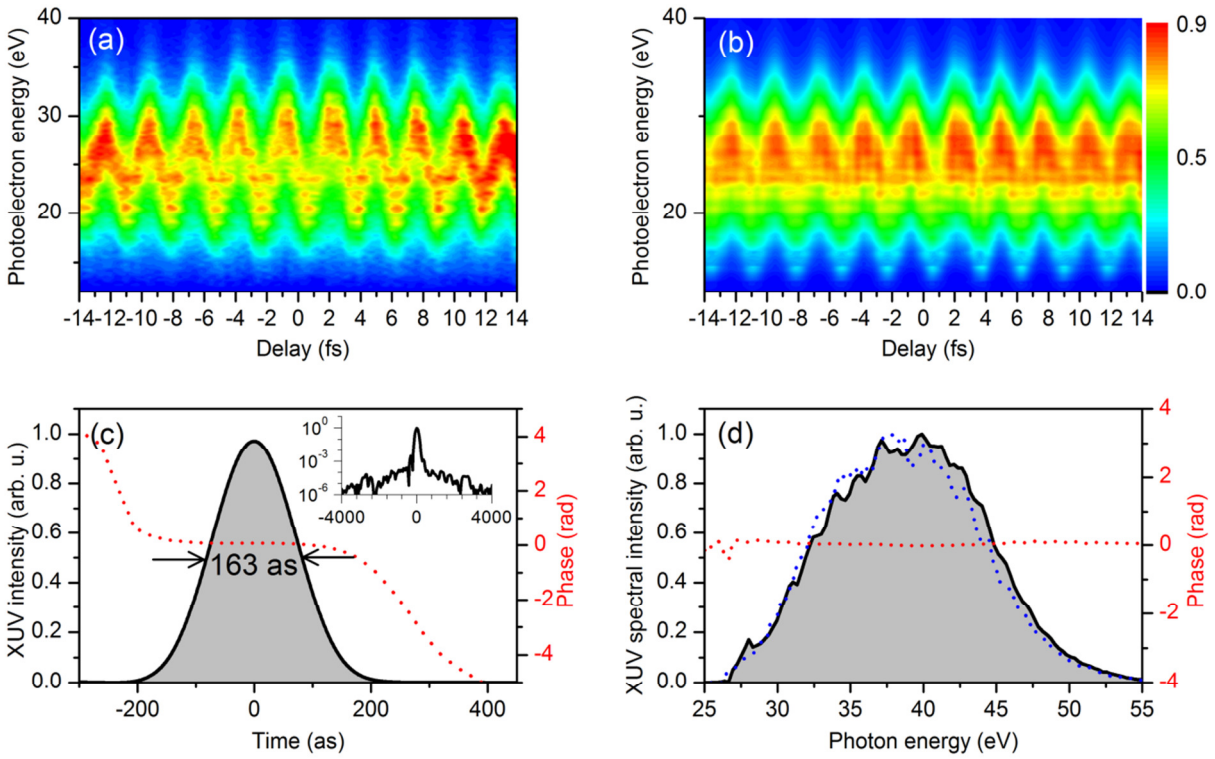

Figure 3-31 (a) Experimentally recorded spectrogram obtained using the GDOG method with neon in the gas cell and gas jet, (b) Reconstructed spectrogram using FROG-CRAB, (c) Retrieved pulse and phase, retrieved pulse with larger time range (inset) (d) Retrieved pulse in the spectral domain compared with the XUV only spectrum [12].

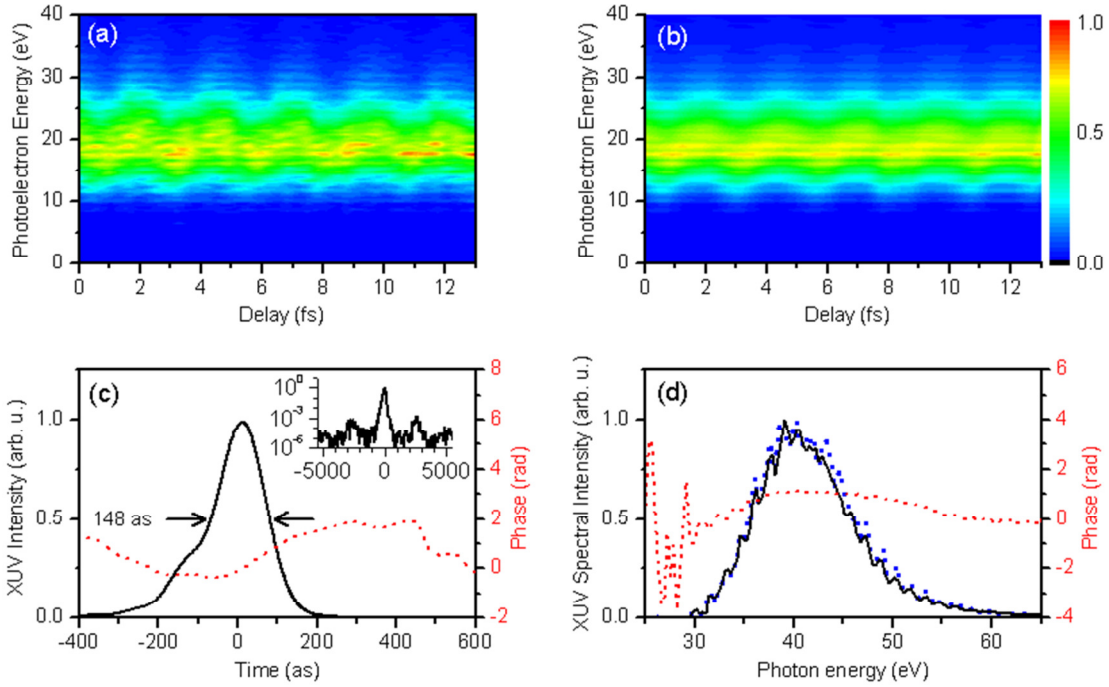

Figure 3-32 (a) Experimentally recorded spectrogram obtained using the GDOG method with using Neon in the gas cell and the gas jet, (b) Reconstructed spectrogram using FROG-CRAB, (c) Retrieved pulse and phase, retrieved pulse with larger time range (inset) (d) Retrieved pulse in the spectral domain compared with the XUV only spectrum [1].

PROOF algorithm

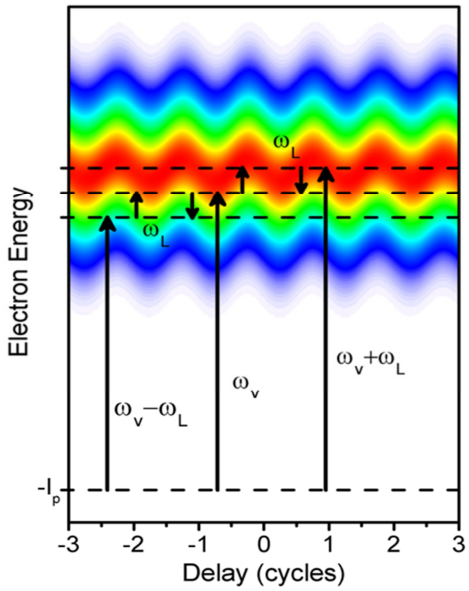

Figure 3-33 The principle of PROOF. A streaked spectrogram is formed by the quantum interference of electrons at ω_v with electrons shifted from $\omega_v \pm \omega_L$ by the dressing laser. The phase at any point ω_v is a function of the phase from $\varphi(\omega_v)$ and $\varphi(\omega_v \pm \omega_L)$ [15].

Overview of PROOF algorithm

For sub-100 attosecond pulses, as the spectrum gets broader the central momentum approximation is no longer valid and FROG-CRAB cannot be used accurately. We developed a new algorithm to characterize such short pulses and called it PROOF (Phase Retrieval by Omega Oscillation Filtering). An attosecond streak camera can be used to measure a PROOF spectrogram. However, the streaking laser intensity should be kept lower than that in FROG-CRAB. The difference between PROOF and FROG-CRAB is the way phase is encoded in the spectrogram. In PROOF, this phase encoding can be described by the quantum interference of continuum states due to the streaking laser. When an attosecond pulse of central frequency ω_v is focused in a gas jet in the attosecond streak camera it is converted into an electron wavepacket. When this electron wavepacket encounters the streaking laser field the electrons from ω_v are either shifted up or down by ω_L, which is the central frequency of the streaking laser. This is shown schematically in Figure 3-33. The streaked electrons at a given point in the spectrum are due to quantum interference between electrons from ω_v and shifted electrons from $\omega_v - \omega_L$ and $\omega_v + \omega_L$. Thus phase at any point is a result of interference between electrons from these three

sources. This, however, is only valid if the streaking laser intensity is weak enough and only single photon transitions are possible. For higher streaking intensities, as typically experienced in FROG-CRAB, electrons from $\omega_\nu \pm 2\omega_L$ and higher can also play a role in the quantum interference and retrieval can get more complicated. In PROOF, we propose that the phase of the attosecond pulse can be completely retrieved by looking at part of the spectrogram with ω_L contributions only. This can be done easily by taking the Fourier transform at each ω_ν along the delay axis.

From equation 3.22, the applied phase shift due to the streaking laser is

$$\phi(t) = -\int_t^\infty \frac{E_0^2(t)}{4\omega_L^2} dt + \frac{\nu E_0(t)}{2\omega_L^2} cos(\omega_L t) - \frac{E_0^2(t)}{8\omega_L^3} sin(2\omega_L t),$$

where the second term has the biggest contribution and the phase shift can be approximated as

$$\phi(t) = \approx \frac{\nu E_0(t)}{2\omega_L^2} cos(\omega_L t). \quad 3.24$$

When $\frac{\nu E_0(t)}{2\omega_L^2} \ll \omega_L$, i.e. the energy shift of the streaking is much smaller than the energy of the streaking laser photon, then

$$e^{i\phi(t)} \approx 1 + i\phi(t) = 1 + i\frac{\nu E_0(t)}{2\omega_L^2} cos(\omega_L t), \quad 3.25$$

or

$$e^{i\phi(t)} = 1 + i\frac{\nu E_0(t)}{\omega_L^2}\left(e^{i\omega_L t} + e^{-i\omega_L t}\right). \quad 3.26$$

From, equation 3.18 the electric field of an attosecond pulse can be given as

$$\varepsilon_X(t) = \int_{-\infty}^{\infty} U(\omega) e^{i\varphi(\omega)} e^{i\omega t} d\omega.$$

and by substituting 3.26 into equation 3.20 and for $d[p_i(t)] \approx 1$, we get

$$b(\nu, \tau) \propto \int_{-\infty}^{\infty} \varepsilon_X(t-\tau)\left[1 + i\frac{\nu E_0(t)}{\omega_L^2}\left(e^{i\omega_L t} + e^{-i\omega_L t}\right)\right] e^{-i\left(\nu^2/2 + I_p\right)t}\, dt. \quad 3.27$$

Substituting equation 3.18 and using relation $\int_{-\infty}^{\infty} e^{i\omega t} dt = \delta(\omega)$, we get

$$b(\nu, \tau) \propto e^{i\omega_\nu t}\left\{U(\omega_\nu) e^{i\varphi(\omega_\nu)} + i\frac{\nu E_0(t)}{\omega_L^2}\left[U(\omega_\nu + \omega_L) e^{i\varphi(\omega_\nu + \omega_L)} e^{-i\omega_L \tau} + U(\omega_\nu - \omega_L) e^{i\varphi(\omega_\nu - \omega_L)} e^{i\omega_L \tau}\right]\right\}. \quad 3.28$$

By defining, $U_\nu = U(\omega_\nu) = \sqrt{I(\omega_\nu)}$, $U_\pm = U(\omega_\nu \pm \omega_L) = \sqrt{I(\omega_\nu \pm \omega_L)}$

$$\varphi_\nu = \varphi(\omega_\nu),\ \varphi_\pm = \varphi(\omega_\nu \pm \omega_L) \text{ and } \varphi_0 = \frac{\nu E_0(t)}{\omega_L^2},$$

we get

$$b(\nu,\tau) \propto e^{i\omega_\nu t}\left\{U_\nu e^{i\varphi_\nu} + i\varphi_0\left[U_+ e^{i\varphi_+} e^{-i\omega_L\tau} + U_- e^{i\varphi_-} e^{i\omega_L\tau}\right]\right\}. \quad 3.29$$

The streaking spectrogram is related to the amplitude of the electron wavepacket by

$$I(\nu,\tau) = |b(\nu,\tau)|^2. \quad 3.30$$

By simple algebraic expansion it can be seen that the streaking spectrogram has three terms: I_0 terms independent of ω_L, I_{ω_L} terms with one photon contribution and $I_{2\omega_L}$ terms with two photon contribution

$$I(\nu,\tau) = I_0 + I_{\omega_L} + I_{2\omega_L}. \quad 3.31$$

The terms with one photon contribution are given as

$$I_{\omega_L} = \varphi_0 U_\nu\left\{ie^{-i\varphi_\nu}\left[U_+ e^{i\varphi_+} e^{-i\omega_L\tau} + U_- e^{i\varphi_-} e^{i\omega_L\tau}\right] - ie^{i\varphi_\nu}\left[U_+ e^{-i\varphi_+} e^{i\omega_L\tau} + U_- e^{-i\varphi_-} e^{-i\omega_L\tau}\right]\right\}, \quad 3.32$$

which can also be given in terms of sines instead of exponentials as

$$I_{\omega_L} = 2\varphi_0 U_\nu\left\{U_+\left[\frac{e^{i(\omega_L\tau+\varphi_\nu-\varphi_+)} - e^{-i(\omega_L\tau+\varphi_\nu-\varphi_+)}}{2i}\right] - U_-\left[\frac{e^{i(\omega_L\tau-\varphi_\nu+\varphi_-)} - e^{-i(\omega_L\tau-\varphi_\nu+\varphi_-)}}{2i}\right]\right\}, \quad 3.33$$

$$I_{\omega_L} = 2\varphi_0 U_\nu\{U_+ sin(\omega_L\tau + \varphi_\nu - \varphi_+) - U_- sin(\omega_L\tau - \varphi_\nu + \varphi_-)\}. \quad 3.34$$

Using the relation $A_1 sin(x+\alpha_1) + A_2 sin(x+\alpha_2) = A_3 sin(x+\alpha_3)$,

where ${A_3}^2 = [A_1 cos(\alpha_1) + A_2 cos(\alpha_2)]^2 + [A_1 sin(\alpha_1) + A_2 sin(\alpha_2)]^2$,

and $tan(\alpha_3) = \frac{A_1 sin(\alpha_1) + A_2 sin(\alpha_2)}{A_1 cos(\alpha_1) + A_2 cos(\alpha_2)}$,

and defining $A_1 = U_+,\ A_2 = -U_-,\ \alpha_1 = \varphi_\nu - \varphi_+,\ \alpha_2 = -\varphi_\nu + \varphi_-,\ x = \omega_L\tau,\ \alpha_3 = \alpha$

and $A_3 = U_\nu\gamma$,

we get

$$I_{\omega_L} = 2\varphi_0 {U_\nu}^2 \gamma sin(\omega_L\tau + \alpha). \quad 3.35$$

Here γ is the modulation depth and α is the phase angle, given by:

$$tan(\alpha) = \frac{\sqrt{I(\omega_\nu+\omega_L)}sin(\varphi(\omega_\nu)-\varphi(\omega_\nu+\omega_L)) + \sqrt{I(\omega_\nu-\omega_L)}sin(\varphi(\omega_\nu)-\varphi(\omega_\nu-\omega_L))}{\sqrt{I(\omega_\nu+\omega_L)}cos(\varphi(\omega_\nu)-\varphi(\omega_\nu+\omega_L)) - \sqrt{I(\omega_\nu-\omega_L)}cos(\varphi(\omega_\nu)-\varphi(\omega_\nu-\omega_L))}, \quad 3.36$$

and

$$\gamma^2 = \frac{1}{I(\omega_\nu)}\left[\sqrt{I(\omega_\nu+\omega_L)}cos\big(\varphi(\omega_\nu)-\varphi(\omega_\nu+\omega_L)\big)+\sqrt{I(\omega_\nu-\omega_L)}cos\big(\varphi(\omega_\nu)-\varphi(\omega_\nu-\omega_L)\big)\right]^2+\left[\sqrt{I(\omega_\nu+\omega_L)}sin\big(\varphi(\omega_\nu)-\varphi(\omega_\nu+\omega_L)\big)+\sqrt{I(\omega_\nu-\omega_L)}sin\big(\varphi(\omega_\nu)-\varphi(\omega_\nu-\omega_L)\big)\right]^2.$$

3.37

This can be simplified as

$$\gamma^2 = \frac{1}{I(\omega_\nu)}\Big[I(\omega_\nu+\omega_L)+I(\omega_\nu-\omega_L) - 2\sqrt{I(\omega_\nu+\omega_L)I(\omega_\nu-\omega_L)}cos\big(\varphi(\omega_\nu)-\varphi(\omega_\nu+\omega_L)-\varphi(\omega_\nu-\omega_L)\big)\Big].$$

3.38

For slowly varying phase $cos(2\varphi_\nu-\varphi(\omega_\nu+\omega_L)-\varphi_-)=cos\big(\varphi_- -\varphi(\omega_\nu+\omega_L)\big)$, and $\gamma^2=\frac{1}{I(\omega_\nu)}\big[I(\omega_\nu+\omega_L)+I(\omega_\nu-\omega_L)-2\sqrt{I(\omega_\nu+\omega_L)I(\omega_\nu-\omega_L)}cos\big(\varphi(\omega_\nu-\omega_L)-\varphi(\omega_\nu+\omega_L)\big)\big]$.

3.39

A closer look at the above equations reveals that by a Fourier transform of the streaking spectrogram along the delay axis, we can retrieve the modulation depth and phase angle, which are a function of $\varphi(\omega_\nu), \varphi(\omega_\nu+\omega_L)\ and\ \varphi(\omega_\nu-\omega_L)$. In Figure 3-34(a) and (d), we present streaking spectrograms with no chirp and chirp in the attosecond pulse, respectively. After Fourier filtering ω_L contribution, the spectrogram is presented in Figure 3-34(b) and (e), with modulation depth in the right panel. After normalization the filtered spectrogram is presented in Figure 3-34(c) and (f), with phase angle given in the right panel. The effect of chirp in the modulation depth and phase angle is quite evident.

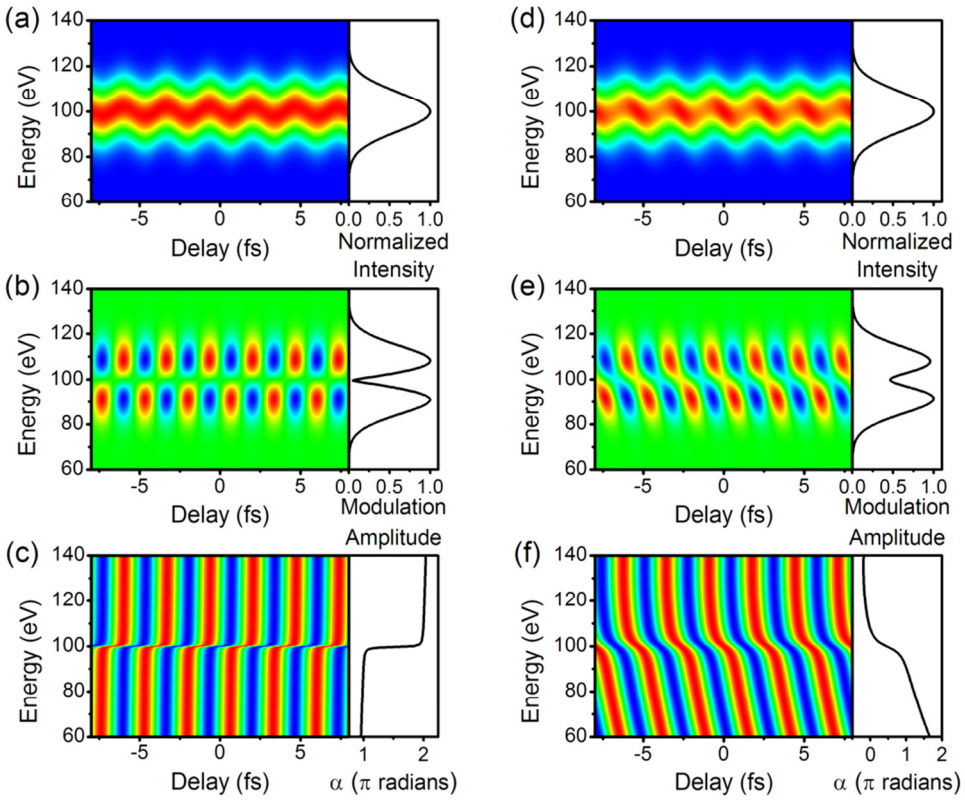

Figure 3-34 Simulated spectrogram from a 95 as transform limited pulse (a) and strongly chirped 300 as pulse (d). Fourier filtered spectrogram and modulation depth for transform limited (b) and chirped case (e). Normalized Fourier filtered spectrogram and phase angle for transform limited (c) and chirped case (f) [15].

Overview of genetic algorithm

From equation 3.36, phase angle is related to spectral phase by

$$tan(\alpha) = \frac{\sqrt{I(\omega_\nu+\omega_L)}sin\left(\varphi(\omega_\nu)-\varphi(\omega_\nu+\omega_L)\right)+\sqrt{I(\omega_\nu-\omega_L)}sin\left(\varphi(\omega_\nu)-\varphi(\omega_\nu-\omega_L)\right)}{\sqrt{I(\omega_\nu+\omega_L)}cos\left(\varphi(\omega_\nu)-\varphi(\omega_\nu+\omega_L)\right)-\sqrt{I(\omega_\nu-\omega_L)}cos\left(\varphi(\omega_\nu)-\varphi(\omega_\nu-\omega_L)\right)}.$$

To calculate spectral phase from phase angle $\alpha(\nu)$, we used multidimensional optimization using an evolutionary algorithm. The dimension of the search space is equal to the number of pixels in the phase, which is typically greater than 150. Instead of using bit-string chromosomes, the phase at each pixel is used as a real number chromosome for this evolutionary algorithm, which leads to much faster convergence. We made several customizations to the standard genetic algorithm to achieve faster and guaranteed convergence in this very large dimensional search, so it may no longer mimic biological evolution. A flow diagram of the algorithm is given in Figure 3-35. A population of 20,000 real number chromosomes with each

chromosome a polynomial of random order and random coefficients is taken as an initial population. In general, the polynomial is given as:

$$P(x) = \sum_{i=0}^{n} \frac{Rnd(-\pi,\pi)}{10^i} x \qquad 3.40$$

Where Rnd$(-\pi, \pi)$ is the random number generator with range $[-\pi, \pi]$ and n is the order of the polynomial calculated by another random number generator. The size of x is equal to the size of the input XUV-only spectrum N, with range [-N/2,N/2]. Fitness is calculated from the least squares error weighted by the spectral intensity as follows:

$$F(i) = \frac{\frac{1}{R(i)}}{Max\left[\frac{1}{R(i)}\right]}, \qquad 3.41$$

where i is the ith population and $R(i)$ is the objective function which is the least squared error between the phase angle from the current chromosome $\alpha(\nu)$ and the experimental phase angle $\alpha_{exp}(\nu)$ weighted by the spectral intensity $I(\omega_\upsilon)$:

$$R(i) = \sum_{\omega_\upsilon} I(\omega_\upsilon)\left[\alpha(\nu) - \alpha_{exp}(\nu)\right]^2. \qquad 3.42$$

The phase angle $\alpha(\nu)$ for the current population is calculated from the phase from chromosomes smoothed by a cubic spline with a balance parameter of 0.2. The main object of the algorithm is to minimize the objective function by maximizing the fitness function. A new population is generated by swapping the chromosomes cleaved at a random location of a pair of populations selected by a roulette wheel biased by the fitness function. The population with the highest fitness has more likelihood of selection than the population with the lowest fitness, which is termed the biased roulette wheel. Additionally, the top 5% of the population is cloned into the next generation. The new population goes through several types of mutation, cross-over and rotation. Three types of mutations are carried out with a probability of 10% each. In 1-point mutation, a random chromosome is picked in a population and is added with a random number between $-\pi$ and π. In multi-point mutation, a random number of consecutive chromosomes is picked and added with a random number between $-\pi$ and π. In the third type, all the chromosomes of a randomly picked population are added with a phase given by a polynomial of random order with random coefficients. For cross-over we used 1-point and multi-point cross-over. In 1-point cross-over, a population pair is randomly picked and a single chromosome at a random location is swapped. In multi-point cross-over a random number of consecutive chromosomes at random locations are swapped between a randomly picked population. It's

worth noting that this is similar to reproduction, which is a special type of multi-point cross-over. The probability for both types of cross-over is 10% each. In rotation, a random population is picked and its chromosomes are rotated randomly. The actual values of the chromosomes remain unchanged, however their locations are changed.

It seems that multi-point mutation, random phase mutation, multi-point cross-over and rotation leads to faster convergence by introducing more genetic diversity and expanding the search space faster than just 1-point mutation and cross-over as seen in typical evolutionary algorithms. Cloning of the top 5% population is termed elitist selection and helps retain good population over several generations. Additionally, 10,000 extra populations containing random phase are added after every 100 generations. This gives a similar effect as running the algorithm several times from the start with a random population and as a result convergence is seen most of the times. The algorithm runs from a minimum 20k to a maximum 100k generations and stops when convergence is achieved.

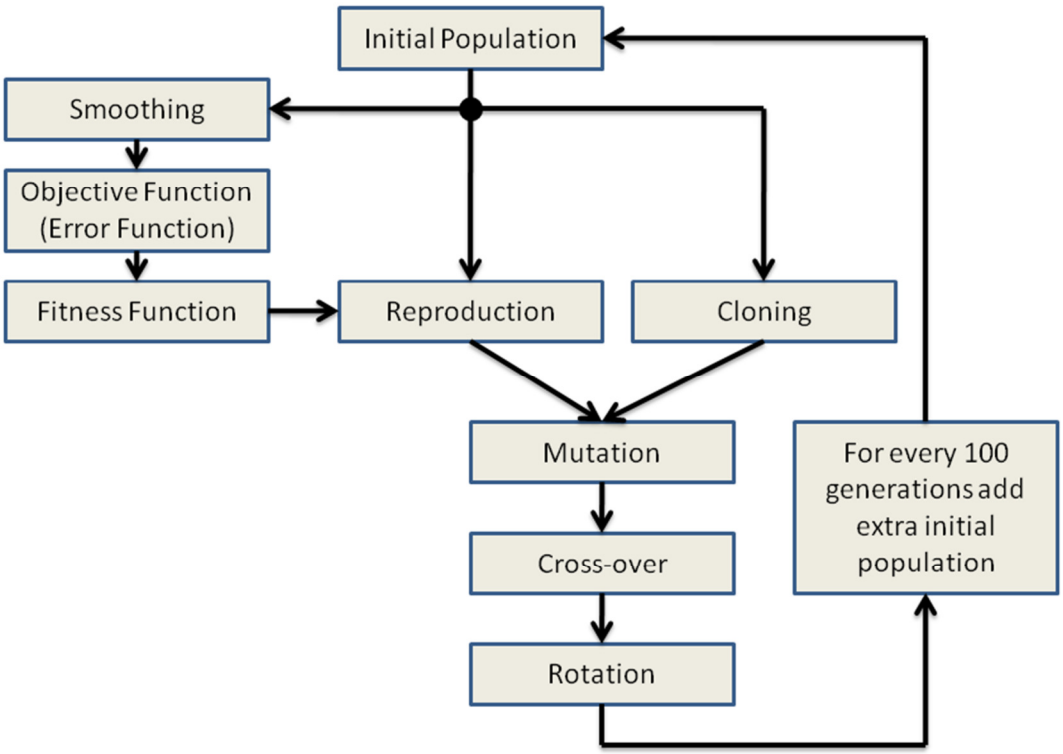

Figure 3-35 Evolutionary algorithm used in PROOF.

Simulations of genetic algorithm with sample functions

To benchmark the evolutionary algorithm we tested it with two hard maximization functions in a 2 dimensional space [16]. The first function consists of a global maximum surrounded completely by rings of local maxima and minima, and is extremely hard for standard search algorithms like the Simplex. With fractional coverage of 1% by the peak of the global maximum, on average 10^2 iterated hill climbing trials are required. The function is given as:

$$f(x,y) = cos^2(n\pi r)\ exp\left(-\frac{r^2}{\sigma^2}\right), \quad 3.43$$

$$r^2 = (x-0.5)^2 + (y-0.5)^2, \quad 3.44$$

where n =9 and σ^2= 0.15 and the domain of x and y is [0,1]. The function is plotted in Figure 3-36.

Using bit-string chromosomes of 8-bits and the same parameters as the actual algorithm, in five trials we were able to achieve convergence in 401, 1, 5, 404 and 105 generations. Convergence was achieved in every trial.

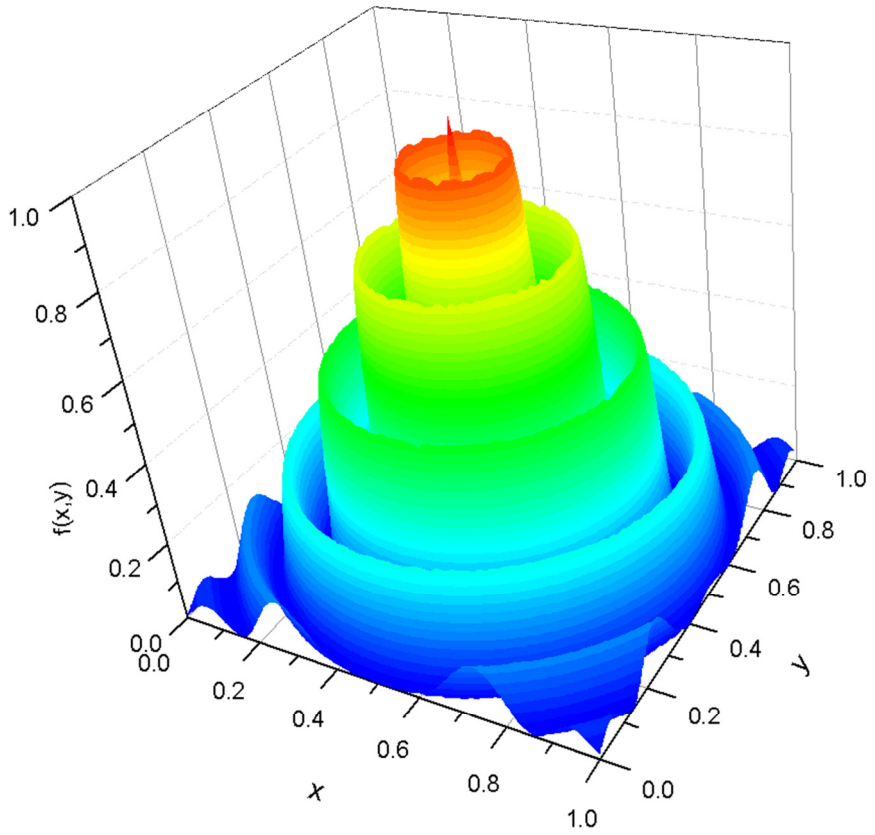

Figure 3-36 Hard test function given by equation 3.43 with maximum at (0.5,0.5) [16].

The second problem is also considered hard, with fraction coverage of 1% by the maximum peak. Unlike the previous problem, this is considered a deceptive problem, as going uphill may lead us away from the solution towards the local maximum. It is given by:

$$f(x,y) = 0.8\, exp\left(-\frac{r_1^2}{0.3^2}\right) + 0.879008\ \ exp\left(-\frac{r_2^2}{0.03^2}\right), \qquad 3.45$$

where $r_1^2 = (x-0.5)^2 + (y-0.5)^2$ and $r_2^2 = (x-0.6)^2 + (y-0.1)^2$. The function in plotted in Figure 3-37.

Using 8-bits bit-string chromosome, convergence was very slow. However, with 32-bits chromosomes and the same parameters as the actual algorithm, in five trials we were able to achieve convergence with a precision of 4 decimal places in 3, 1802, 776, 4902 and 305 generations. Convergence was achieved in every trial. On closer inspection the algorithm was not trapped by the deceptive nature of the problem, and a 1% peak with global maxima was located in less than 10 generations in every trial.Convergence was delayed, however, due to slow hill climbing, a problem similar to Hamming's Wall. The number of bits needed to mutate simultaneously was large and took many generations. Such issues could be solved with a better choice of chromosome scheme. Note that in the actual algorithm bit-string chromosomes were not used.Instead, real number chromosomes were used, which significantly improved convergence.

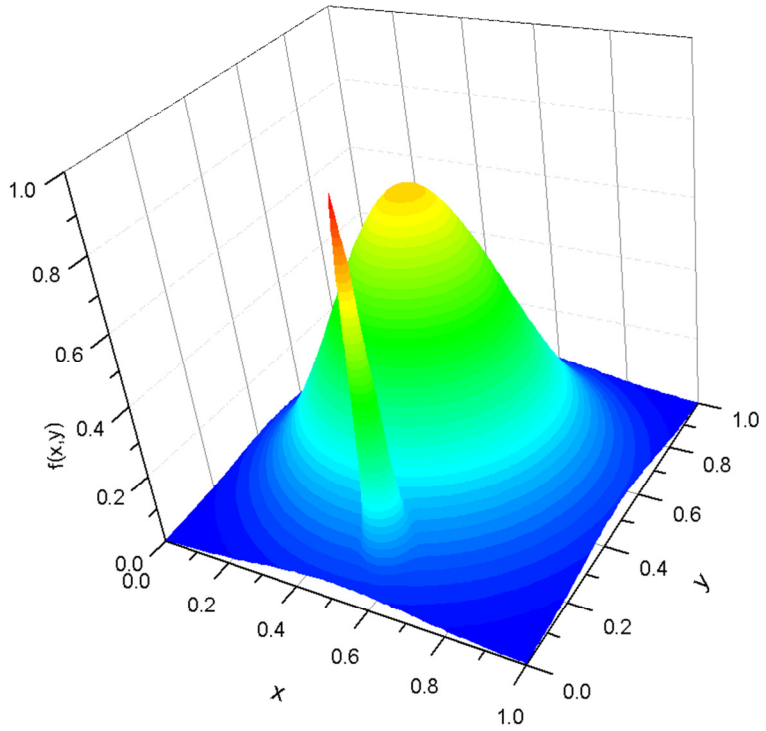

Figure 3-37 Hard and deceptive test function given by equation 3.45 with maximum at (0.6,0.1) [16]

Theoretical simulations

To check the ability of PROOF to retrieve attosecond pulses with broad spectra, we tested it against a complicated broad synthetic spectrum extending from 0 to 200 eV corresponding to 25 as pulse duration with chirp added to make a ~73 as pulse. The streaking laser had 20 fs pulse duration and 10^{11} W/cm^2 intensity. The streaking intensity is picked so that both FROG-CRAB and PROOF are valid. The streaked spectrogram is presented in Figure 3-38(a), and the Fourier filtered ω_L contribution and phase angle α are presented in Figure 3-38(b). The retrieved intensity and phase in the spectral domain is given in Figure 3-38(c), while the retrieved pulse is presented in Figure 3-38(d). FROG-CRAB retrieved a flat phase due to the fact that the central momentum approximation is not valid for this broad bandwidth. It is quite evident that FROG-CRAB under-estimates the pulse duration, while PROOF can accurately retrieve the phase.

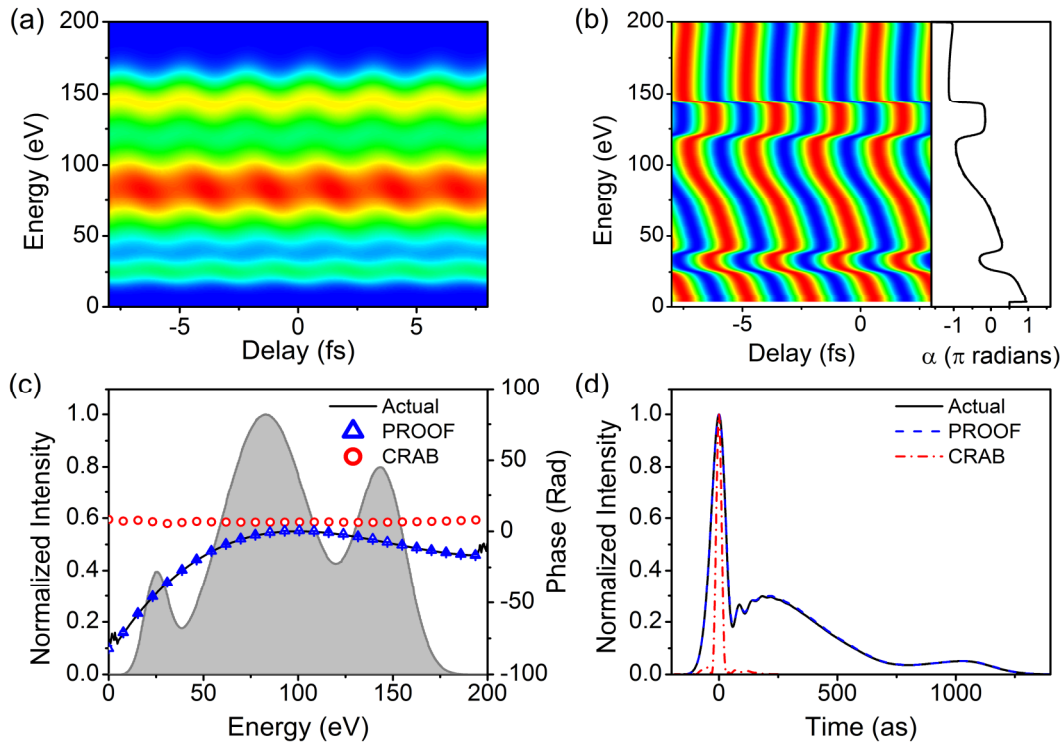

Figure 3-38 (a) Simulated spectrogram of broad continuum extending from 0 to 200 eV supporting a 25 as transform limited pulse with chirp added to make ~73 as streaked by 20 fs pulse with 10^{11} W/cm^2 intensity. (b) ω_L contribution by Fourier filtering and phase angle. (c) Retrieved spectrum and phase retrieved using PROOF (blue triangles) and FROG-CRAB (red circles) compared with actual phase (black line). (d) Retrieved pulse from PROOF (blue dashed, 73 as pulse duration) and FROG-CRAB (red dot dashed, 26 as pulse duration) compared with actual pulse (black line) [15].

Experimental measurement

Comparison with FROG-CRAB

To benchmark PROOF with FROG-CRAB, we took an experimental spectrogram using GDOG under conditions in which both the central momentum approximation is valid and the streaking intensity is suitable. The streaking laser was 25 fs with an intensity of ~10^{12} W/cm^2, which is enough for FROG-CRAB retrieval. The experimentally recorded spectrogram is presented in Figure 3-39(a), while the Fourier filtered ω_L contribution and phase angle α are presented in Figure 3-39(b). The retrieved intensity and phase in the spectral domain is given in

Figure 3-39(c), while the retrieved pulse is presented in Figure 3-39(d). As evident from Figure 3-39(c) and (d). PROOF agrees quite accurately with FROG-CRAB.

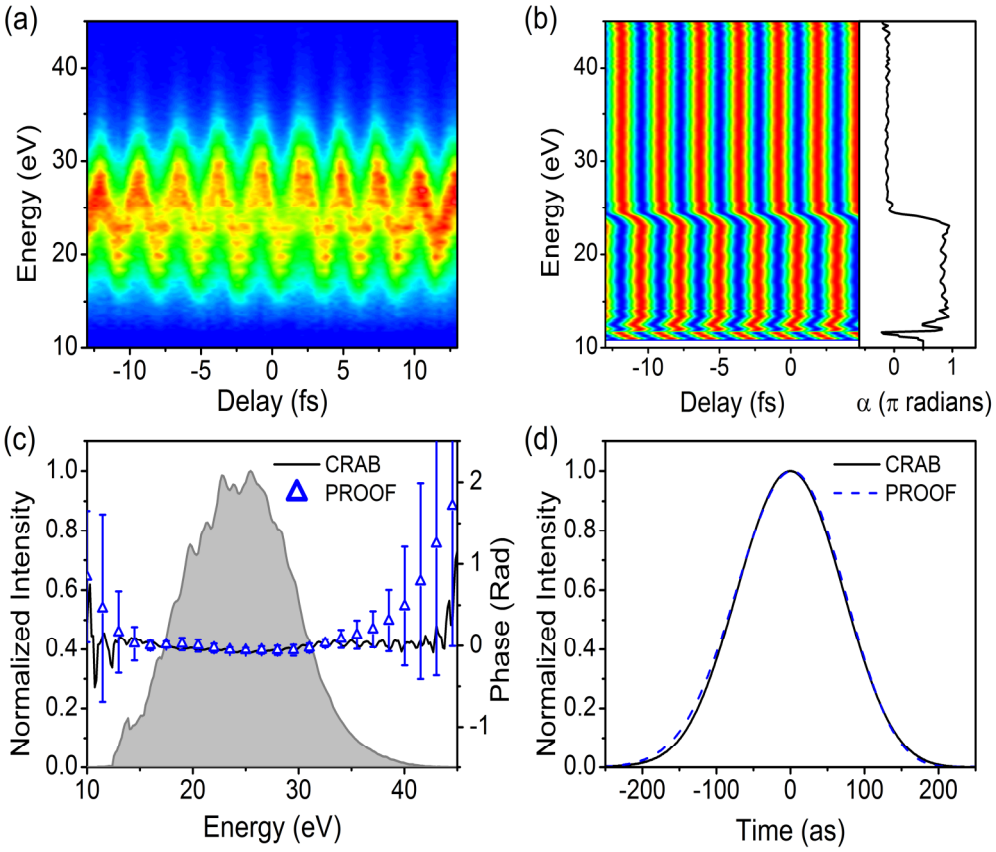

Figure 3-39 Benchmark of PROOF with FROG-CRAB (a) Experimentally recorded spectrogram. (b) ω_L contribution by Fourier filtering and phase angle. (c) Retrieved spectrum and phase retrieved using PROOF (blue triangles) and FROG-CRAB (black line), (d) Retrieved pulse from PROOF (blue dashed, 170 as pulse duration) and FROG-CRAB (black line, 167 as pulse duration) [15].

Attosecond streaking without CE-phase locking

CE-phase effect & GDOG gate width

CE-phase lock is an important constraint, which is preventing the use of high power lasers to generate intense attosecond pulses, since currently it's a technical challenge to lock CE-phase of a peta-watt class laser. By setting the gate width of GDOG to less than 1 fs, we were able to demonstrate that with very small gate width single attosecond pulses can be generated without the need of CE-locking. As presented in Figure 3-40 (a) and (b), in an elliptically

dependent field, attosecond pulses are only produced in the narrow region where polarization is linear. When CE-phase is not locked, the carrier of the driving laser drifts within this gating region. With a very narrow gate width, an attosecond pulse is either produced or suppressed with drifting CE-phase. To prove this point we present electron spectra as a function of CE-phase from 0 to 10π in Figure 3-40(c), and it's evident that the continuum is either present or absent, but no discrete harmonics are visible. However, the flux of the attosecond pulse fluctuates with changing CE-phase, which is evident from the fluctuation of the attosecond continuum signal in Figure 3-40 (c). In Figure 3-40(d), we present a spectrogram obtained with unlocked CE-phase. The retrieved pulse is presented in figure 3-40(e), with a pulse duration of 182 as. The spectrograms obtained with CE-phase locked at 0, π/2, π and 3π/2 are presented in Figure 3-41(a), (b), (c) and (d) respectively. The continuum spectra are presented in Figure 3-42(a). The highest flux is evident at π CE-phase and the lowest at 0 CE-phase. The retrieved pulses are presented in Figure 3-42(b) and (c), with pulse durations of 180, 183, 180 and 183 as for CE-phase of 0, π/2, π and 3π/2, respectively. The extracted electric field of the streaking laser from the spectrograms in Figure 3-41 is presented in Figure 3-42(d). The change of CE-phase is quite evident. Comparing pulse durations retrieved from locked and unlocked CE-phase, it is evident that with very small gate widths of GDOG pulse, it is possible to generate single attosecond pulses without the need to lock CE-phase. These are pretty powerful results and open the possibility of using currently available peta-watt class lasers and future high power lasers to produce intense single attosecond pulses.

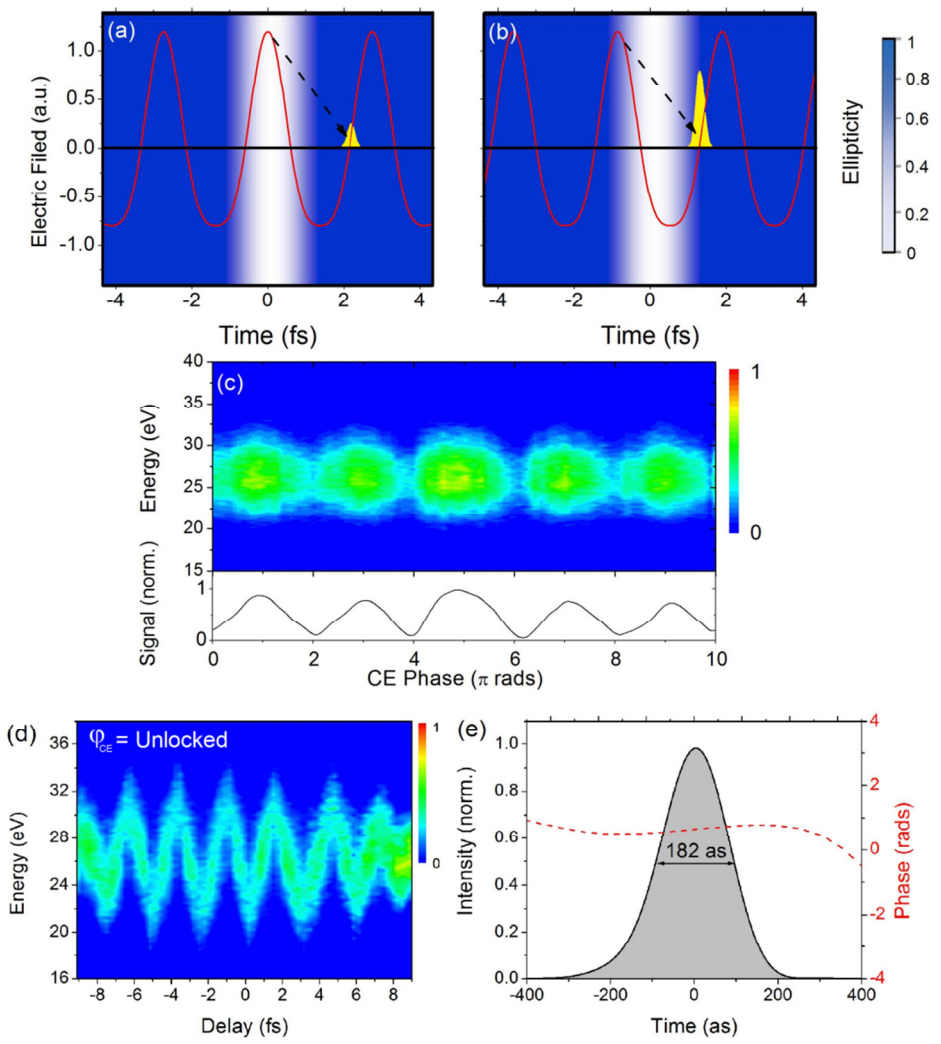

Figure 3-40 Single attosecond pulse generated from narrow gate width (~1 fs) using GDOG. In (a), the CE phase of the NIR laser means the freed electron recombines in a field of high ellipticity, severely limiting its recombination probability. In (b), the CE phase is more favorable for high attosecond pulse emission since the electron experiences a linear field for its full lifetime. The color gradient represents the ellipticity of the field with the darker being the most elliptical and white the most linear. Generated continuum as a function of CE-phase (c) and signal strength of the continuum. Spectrogram from unlocked CE-phase (d) and retrieved pulse (black line) and phase (red dashed) (e) [17].

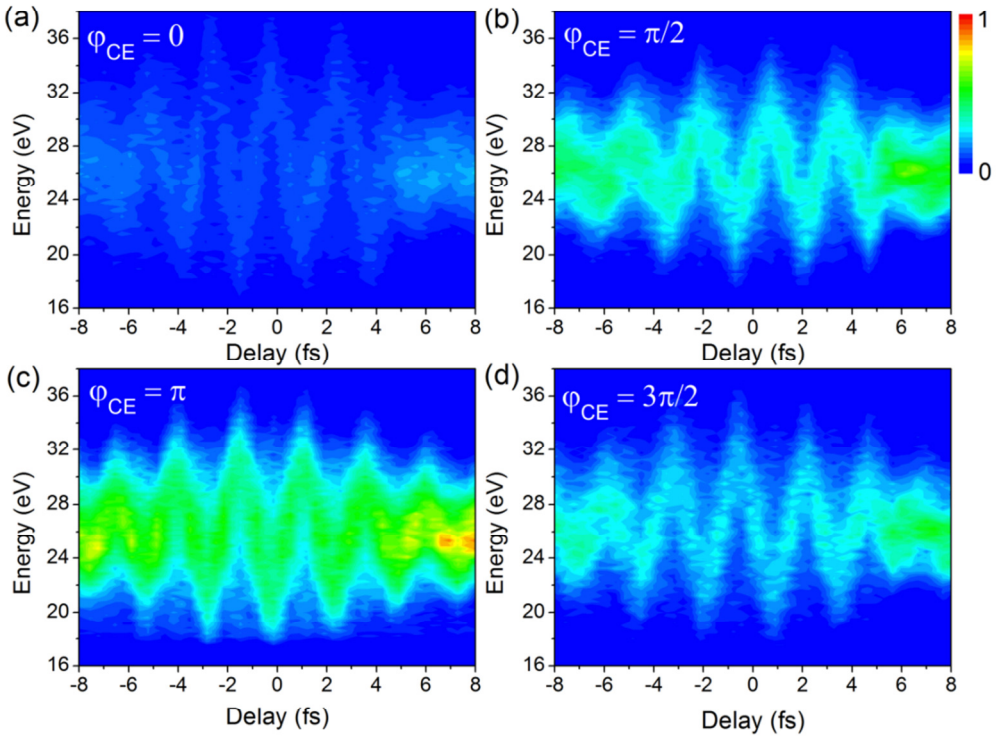

Figure 3-41 Spectrogram obtained with narrow gate width (~1 fs) using GDOG at CE-phase 0, π/2, π and 3π/2 in (a), (b), (c) and (d) respectively [17].

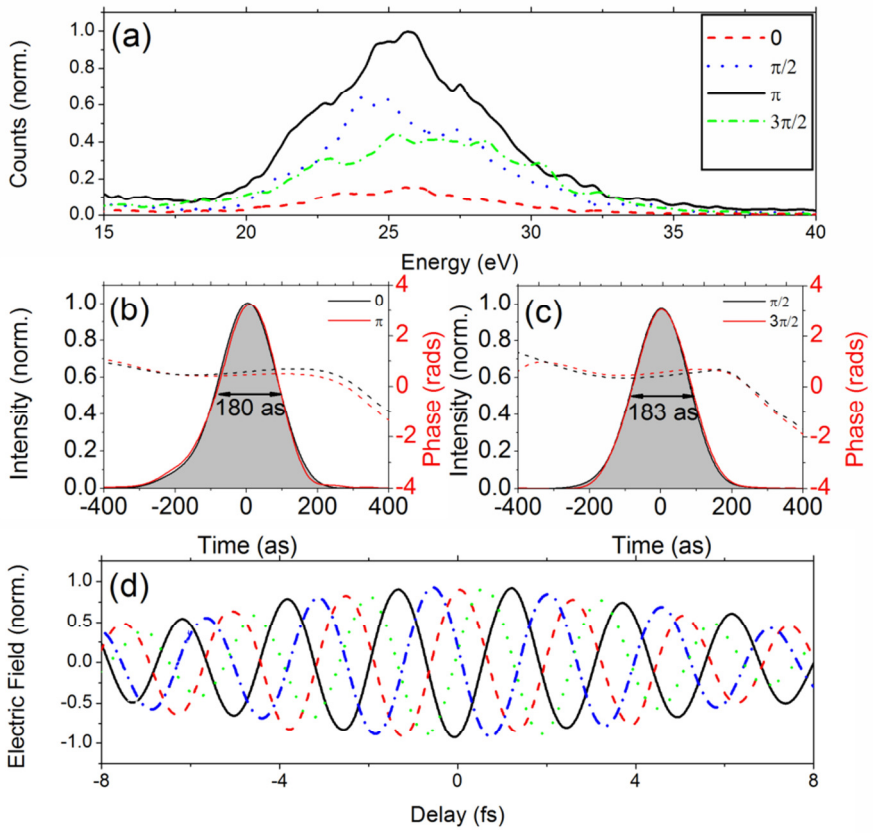

Figure 3-42 (a) Photo electron spectra from CE-phase of 0, π/2, π and 3π/2, (b) Retrieved pulse for 0 and π CE-phase, (c) Retrieved pulse for π/2 and 3π/2, (d) Retrieved streaking field for CE-phase of 0, π/2, π and 3π/2. [17].

References

[1] X. Feng, S. Gilbertson, H. Mashiko, H. Wang, S. D. Khan, M. Chini, Y. Wu, K. Zhao, and Z. Chang, "Generation of Isolated Attosecond Pulses with 20 to 28 Femtosecond Lasers", Phys. Rev. Lett., 103,18,183901 (2009).

[2] B.L. Henke, E.M. Gullikson, and J.C. Davis, "X-ray interactions: photoabsorption, scattering, transmission, and reflection at E=50-30000 eV, Z=1-92", Atomic Data and Nuclear Data Tables, 54, 2, 181 (1993).

[3] "MCP Delay line detector manual", Roentdek Handles GmbH, http://www.roentdek.com/manuals/MCP%20Delay%20Line%20manual(9.22.1003.1).pdf

[4] "Technical information manual, Mod. V1290-VX1290 A/N, 32/16 Ch. Multihit TDC", CAEN http://www.caen.it/servlet/checkCaenManualFile?Id=8082 (2011).

[5] S. Gilbertson, M. Chini, X. Feng, S. Khan, Y. Wu, and Z. Chang, "Monitoring and Controlling the Electron Dynamics in Helium with Isolated Attosecond Pulses", Phys. Rev. Lett., 105, 263003 (2010).
[6] X. Feng, S. Gilbertson, S. D. Khan, M. Chini, Y. Wu, K. Carnes, and Z. Chang , "Calibration of electron spectrometer resolution in attosecond streak camera", Optics Express, 18, 2, 1316 (2010).
[7] H. D. Morgan and D. L. Ederer, “Photoionization cross section of helium for photon energies 59-67 eV: The (sp,2n+) 1P0 Rydberg series of autoionizing resonances,” Phys. Rev. A 29, 1901 (1984).
[8] Y. Mairesse and F. Quéré, "Frequency-resolved optical gating for complete reconstruction of attosecond bursts", Phys. Rev. A, 71, 011401(R) (2005).
[9] H. Wang, M. Chini, S. D Khan, S. Chen, S. Gilbertson, X. Feng, H. Mashiko and Z. Chang, "Practical issues of retrieving isolated attosecond pulses", J. Phys. B: At. Mol. Opt. Phys., 42, 134007 (2009).
[10] J. Gagnon, E. Goulielmakis and V.S. Yakovlev, "The accurate FROG characterization of attosecond pulses from streaking measurements", App. Phys. B, 92, 25(2008).
[11] Kane, D. J., "Recent progress toward real-time measurement of ultrashort laser pulses", IEEE J. Quantum Electronics, 35, 421 (1999).
[12] S. Gilbertson, Y. Wu, S. D. Khan, M. Chini, K. Zhao, X. Feng, and Z. Chang, "Isolated attosecond pulse generation using multicycle pulses directly from a laser amplifier", Phys. Rev. A 81, 043810 (2010).
[13] R. Kienberger, E. Goulielmakis, M. Uiberacker, A. Baltuska, V. Yakovlev, F. Bammer, A. Scrinzi, Th. Westerwalbesloh, U. Kleineberg, U. Heinzmann, M. Drescher and F. Krausz, "Atomic transient recorder", Nature, 427, 817 (2004).
[14] S. D. Khan, H. Wang, X. Feng, M. Chini, Z. Chang, "Practical Issues of Retrieving Isolated Attosecond Pulse from CRAB", Conference on Lasers and Electro-Optics (CLEO), OSA Technical Digest (CD), CThDD4 (2009).
[15] M. Chini, S. Gilbertson, S. D. Khan, and Z. Chang, "Characterizing ultrabroadband attosecond lasers", Optics Express, 18, 12, 13006 (2010).

[16] P. Charbonneau, "AN INTRODUCTION TO GENETIC ALGORITHMS FOR NUMERICAL OPTIMIZATION", NCAR Technical Note, http://informatics.indiana.edu/larryy/al4ai/extras/Charbonneau.GAtutorial.pdf (2002).
[17] S. Gilbertson, S. D. Khan, Y. Wu, M. Chini, and Z. Chang, "Isolated Attosecond Pulse Generation without the Need to Stabilize the Carrier-Envelope Phase of Driving Lasers", Phys. Rev. Lett., 105, 093902 (2010).

Chapter 4 - Intense attosecond pulses with 400 nm driving pulses

With 800 nm driving pulses, the highest reported attosecond photon flux is in the few nJ range [1,2], which limits their use in attosecond pump, attosecond probe experiments and non-linear attosecond science. It is known from theory that harmonic efficiency scales as λ^{-6} in the plateau region and λ^{-5} in the cutoff region of high harmonics spectra [3], where λ is the wavelength of the driving laser. Additionally, Falcao-Filho et al. [4] demonstrated a conversion efficiency of 10^{-4} for ~90 eV high harmonic photons and 10^{-5} for the 80-150 eV range from 400 nm (blue) driving pulses, which is two to three orders of magnitude higher than from 800 nm (red) driving lasers. In this chapter, we investigate the phase matching of high harmonics from blue driving pulses, compare them with red driving pulses in gas and plasma mediums, and report the first experimental measurement of ellipticity dependence at 400 nm. We present results of first demonstration of high harmonics from carbon plasmas using blue pulses. In later chapters, we attempt to compress these pulses to sub-10 fs and propose a gating scheme to extract single attosecond pulses.

Generation of blue driving pulse

We used a BBO (beta barium borate) crystal (300 µm thick, Type 1 phase matching) for second harmonic generation from 800nm pulses to generate blue driving pulses. With an unfocused beam we were able to get ~25% efficiency (1.2mJ output, 1kHz repetition rate) by slight tuning of the amplifier compressor to pre-compensate the chirp introduced by the propagation in the BBO. Efficiency can be further increased by focusing the beam, however, filamentation at the focus spot can reduce beam quality. The beam energy at the BBO was close to the damage threshold of the BBO, which is 200GW/cm^2 [5].

Dichroic mirrors and astigmatism

To separate red pulses from blue we used two dichroic mirrors (LWP-45-Rp400-Ts800-PW-1025-UV). The reflectivity curve is presented in Figure 4-1; the reflectivity at 400nm was >99%. We found through experiments that the thin substrate of the dichroic mirror (as usually preferred in such applications) is prone to surface distortions and leads to astigmatism in the focused beam, as presented schematically in Figure 4-2 [6]. A flat surface of the dichroic mirror (ideal case, Figure 4-2(a)) can lead to a single focus spot. However a small curvature can

introduce astigmatism in the focused beam, and two focus spots (from tangential and sagittal rays) were detected using a CCD camera with a microscope objective. This phenomenon is common in confocal microscopy [6]. To remove this aberration in our focusing system, we used a thick fused silica substrate (>5 mm) to keep the reflecting surface of the dichroic mirror distortion free. The damage threshold of the dichroic mirrors is 4-5 J/cm^2 (at 400 nm, 20 ns). The damage threshold for femtosecond pulses is not available experimentally[7].

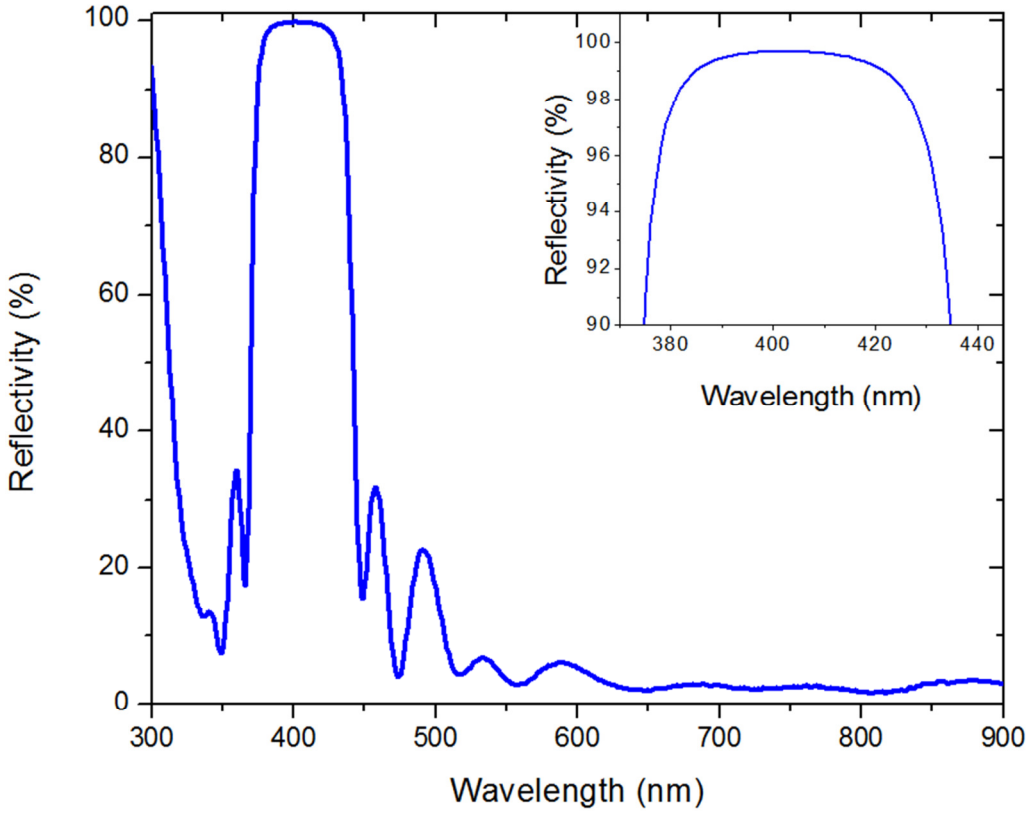

Figure 4-1 Reflectivity of dichroic mirror over the 300 to 900nm wavelength range. Reflectivity within our range of interest from 380 to 425nm (inset) [8].

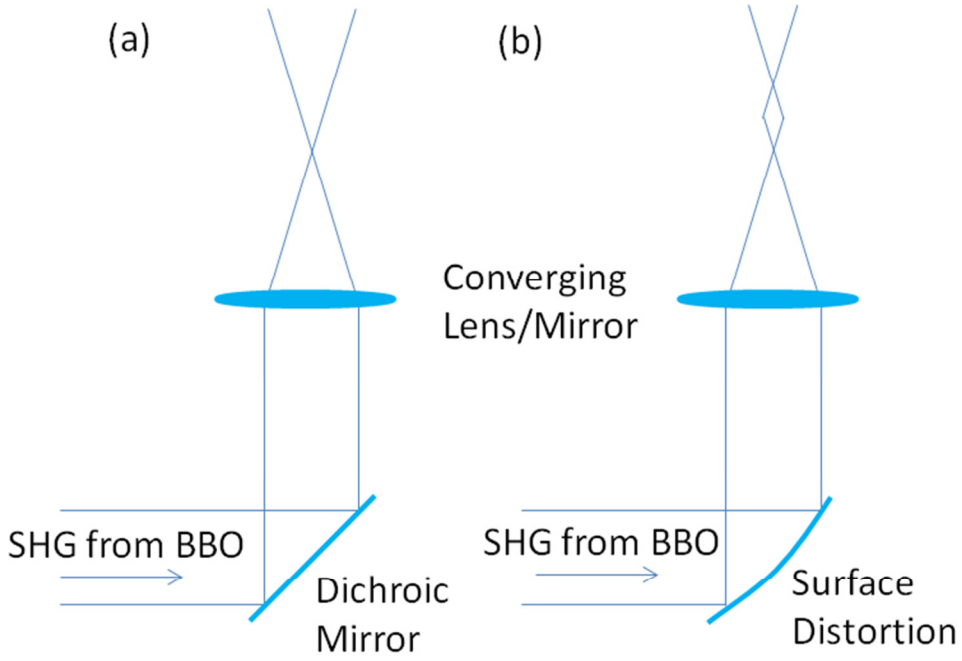

Figure 4-2 Schematic to illustrate astigmatism due to surface distortion in a thin dichroic mirror, (a) No astigmatism from the ideally flat surface of the dichroic mirror, (b) astigmatism due to curvature in the surface [6].

Silver, aluminum and dielectric mirrors for 400nm driving pulses

In Figure 4-3 reflectivity curves are presented for the typical mirror coatings we used for this experiment. As evident from Figure 4-3(b), protected silver (PS) has a sharp dip below 420nm and is not suitable for experiments with blue pulses. We used dielectric mirrors with TLM1-400 (>99% reflectivity) coating and UV enhanced aluminum (PAUV) mirrors (>85%) in this experiment. As evident in Figure 4-3(b), the TLM1-400 coating has a bandwidth dependence on incidence angle and polarization. However, even the minimum bandwidth (45^{o}, P-polarization) is not a bottle-neck in our spectral range of interest. For long pulses, the maximum spectral range is from 400 to 410 nm, and for short pulses the maximum range is from 485 to 420 nm. The damage threshold of PAUV and TLM1-400 coatings is 0.07 J/cm^2 (at 355 nm, 10 ns) and 20 J/cm^2 (at 1064 nm, 20 ns), respectively [8]. The experimental damage threshold is not available for these coatings for femtosecond pulses.

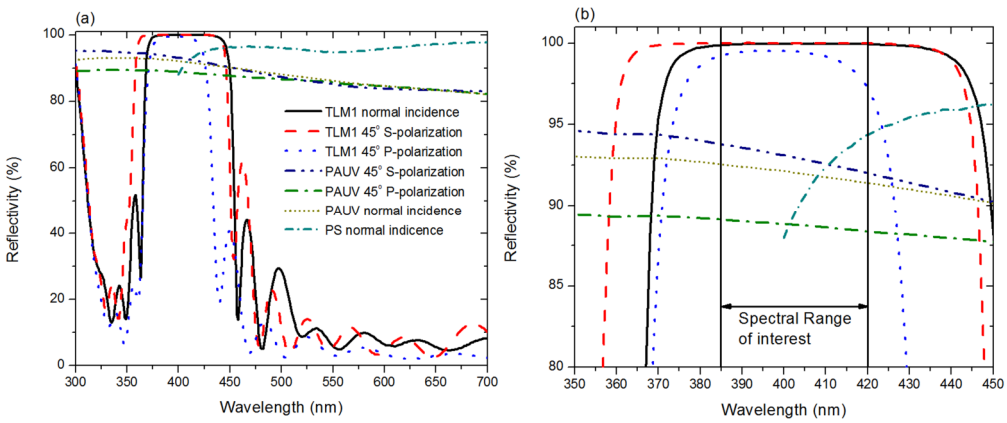

Figure 4-3 Reflectivity curve of TLM1, UV enhanced protected aluminum (PAUV) and protected silver (PS) in 300 to 700nm range (a) and 350 to 450nm range(b)[8].

Short pulse second harmonic generation

As an alternate to hollow core fiber compression to get blue short pulses, we tried to achieve this directly from the BBO by second harmonic generation. Figure 4-4 presents the bandwidth of various thicknesses of BBO calculated using the following spectral filter function [9]:

$$H(\lambda) = \left(\frac{sin(\Delta k(\theta,\lambda)\, L)}{\Delta k(\theta,\lambda)\, L}\right)^2, \qquad 4.1$$

where $\Delta k(\theta, \lambda)$ is the phase mismatch as a function of the fundamental wavelength λ and the BBO angle θ and L is the thickness of the BBO.

Based on these calculations for an unfocused beam the bandwidth is 24.6, 12.2, 8.1 and 4.1 nm for 50, 100, 150 and 300 µm thick BBO, respectively. This bandwidth can be increased with a convergent beam as the beam makes more than one angle with the BBO crystal, and phase matching can be enhanced. To get sub-10 fs pulses we need a bandwidth of at least 24 nm. The experimental setup, as presented in Figure 4-5, consists of a hollow core fiber and chirp mirror compression for the generation of red pulses from a Ti:sapphire laser. An extra pair of chirp mirrors is used to pre-compensate the beam for propagation in air and tune the chirp in the BBO. The slightly negatively chirped short red pulses (~2 mJ pulse energy, 1 kHz repetition rate) are then focused into a BBO using a 1.5 m focal length aluminum mirror and then collimated with another 1.5 m focal length aluminum mirror. Two dichroic mirrors are then used to separate the

collimated red and blue pulses. Fused silica plates are used before the BBO to optimize the chirp of the fundamental for the best efficiency. Since a broad spectrum is available in the short red pulses, the BBO angle was tuned to get the best efficiency and/or bandwidth. Both bandwidth and efficiency are a function of angle tuning. In Figure 4-6, efficiency and bandwidth as a function of BBO angle are presented for 141 and 300 μm thick BBO. The spectra for the BBO angle at the best bandwidth and highest efficiency is presented in Figure 4-7. With 141 μm BBO, a maximum bandwidth of 14.1 nm was obtained with a pulse energy of 69 μJ, and a 12.31 nm bandwidth was obtained with a pulse energy of 75 μJ with a 300 μm thick BBO. Additionally, bandwidths of 65 and 61 nm were obtained with 10 and 50 μm thick BBO, respectively. However, the pulse energy was less than 40 μJ, while the background level of the power meter was 37 μJ. Thus the pulse was too weak to be measured accurately. The beam quality of the blue pulse was poor and a hot spot was also detected in the red beam, which damaged first dichroic mirror, subsequently damage was avoided by reducing the pressure in the fiber to reduce self phase modulation. The poor beam quality was attributed to the filament formation of the red beam at the focus of the 1.5 m focal length focusing mirror, while the hot spot may be due to Bessel beam propagation of the intense short red beam in air. Using 141 μm BBO at 0^{o} angle of incidence, we focused the short blue pulse using a 375 mm focal length aluminum mirror in an argon gas cell (Pressure = 17 Torr) and generated high harmonics. The blue pulse could not produce a filament in air, but weak 7^{th} and 9^{th} harmonics were observed with argon. A 300 nm aluminum filter was used to separate the blue pulse from high harmonics and a grating based spectrometer with an MCP and phosphor screen based imaging system was used to detect high harmonic spectra (Details of the spectrometer are discussed later in the chapter). With blue driving pulses, the 7^{th} and 9^{th} harmonics are visible. Shown in Figure 4-8. The 9^{th} harmonic (27.9 eV) corresponds to 2.57×10^{14} W/cm^2, based on the cutoff law from the semi-classical model. Thus intensity $>2.57 \times 10^{14}$ W/cm^2 was available at the focus spot in the gas cell. The pulse energy of the blue driving pulse at the entrance of the spectrometer was 170 μJ. However, the harmonic peaks were weak, which we attribute it to bad beam profile and chirp.

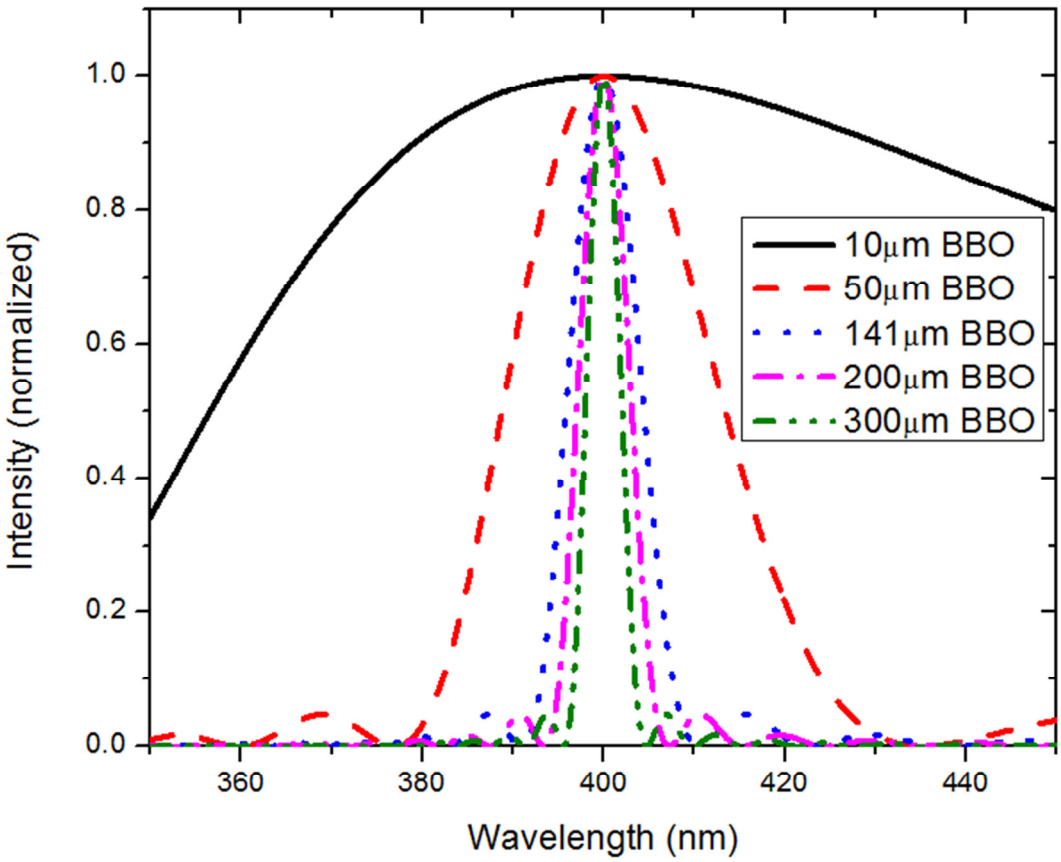

Figure 4-4 Spectral filter function as a function of wavelength for various BBO thicknesses.

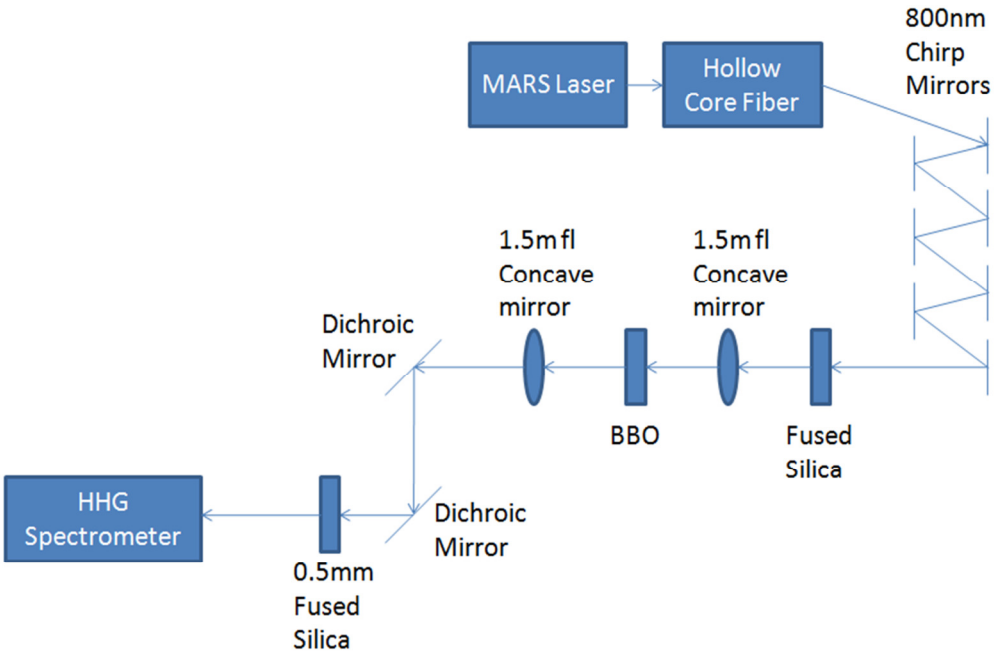

Figure 4-5 Experimental setup for generating SHG from short fundamental pulse.

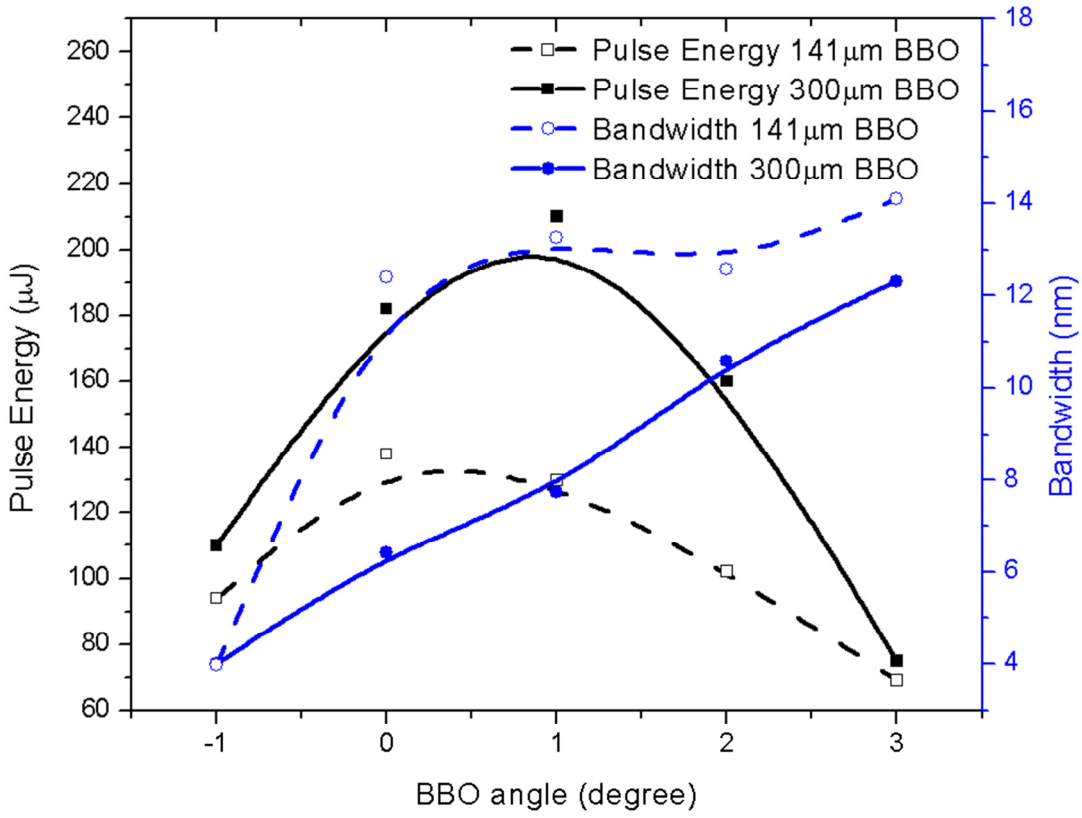

Figure 4-6 SHG pulse energy and bandwidth as a function of BBO angle for 141 and 300 μm BBO.

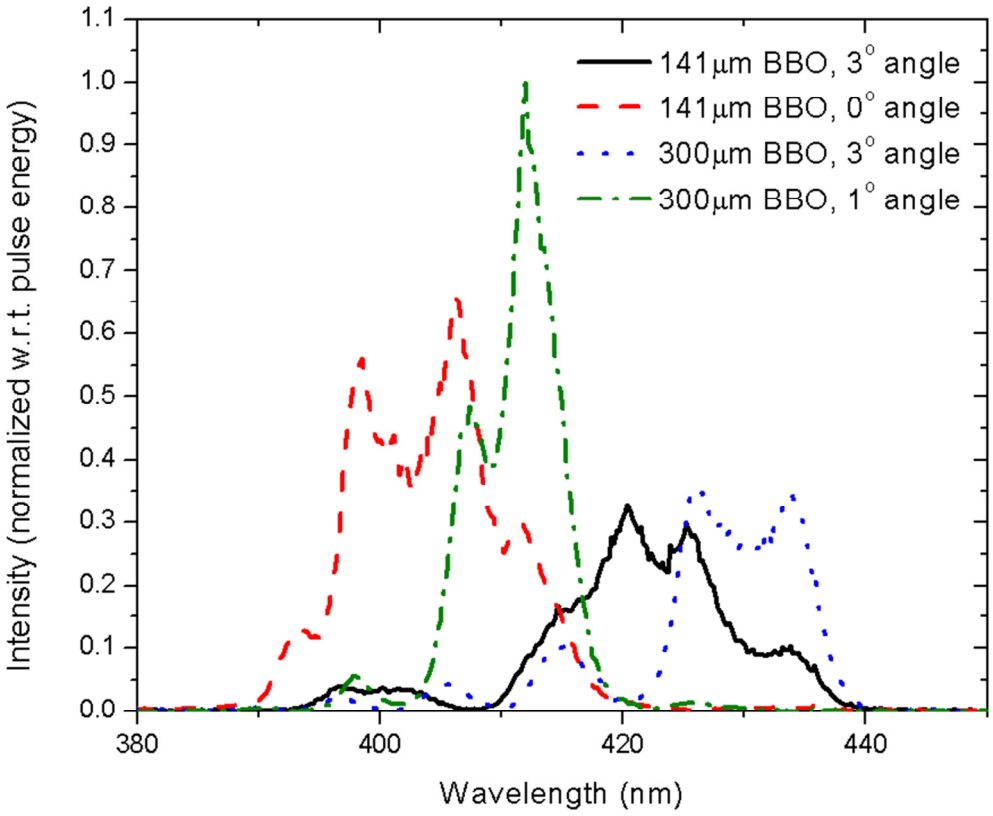

Figure 4-7 Second harmonic spectra from 141 and 300 μm BBO with highest second harmonic pulse energy and maximum bandwidth.

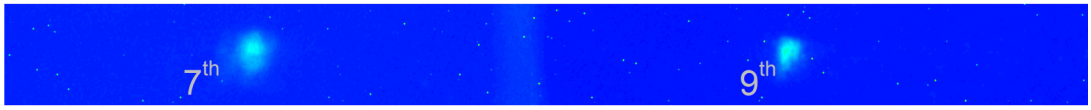

Figure 4-8 High harmonic spectrum obtained from blue pulses generated by red short pulses from BBO.

High harmonics from 400nm in gases and comparison with 800nm

We compared the high harmonic efficiency between red and blue driving pulses focused in an argon gas cell using a grating based spectrometer. We measured the strength of the 7th harmonic (~21.7 eV) from blue driving pulses and the 13th harmonic (~20.15 eV) from red driving pulses for the same driving laser pulse energy, 860 μJ. The spectra are shown in Figure 4-9. The area under the 7th harmonic peak (from blue pulses) of the measured spectrum is about 100 times larger than that under the 13th harmonic (from red pulses). This indicates an increase of two orders of magnitude in the energy conversion efficiency for the 7th harmonic (from blue

pulses) compared to that of 13th harmonic (from red pulses). It is consistent with the observations in [6].

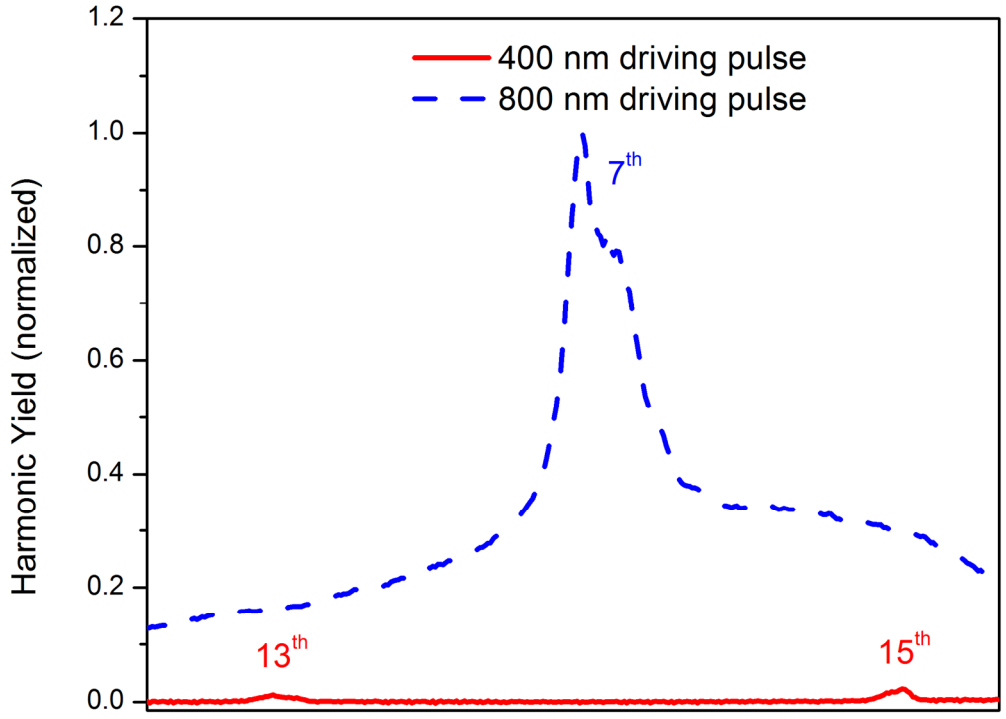

Figure 4-9 Comparison of high harmonics generated from red and blue pulses under same driving pulse energy of 860 μJ.

Ellipticity dependence of argon, neon and helium

Theoretical model

To calculate the ellipticity dependence of high harmonics driven by red and blue pulses, we developed a theoretical model by extending the semi-classical 3-step model to elliptically polarized laser pulses. If the electric field of the elliptically dependent pulse is given by

$$\vec{F}(t) = \frac{F}{\sqrt{1+\varepsilon^2}}\begin{bmatrix} cos(\omega t) \\ \varepsilon\, sin(\omega t) \end{bmatrix}, \qquad 4.2$$

then from Newton's second law,

$$\begin{bmatrix} a_x(t) \\ a_y(t) \end{bmatrix} = \begin{bmatrix} \frac{d^2x}{dt^2} \\ \frac{d^2y}{dt^2} \end{bmatrix} = -\frac{F}{\sqrt{1+\varepsilon^2}}\begin{bmatrix} cos(\omega t) \\ \varepsilon\, sin(\omega t) \end{bmatrix}. \qquad 4.3$$

Integration with respect to time gives velocity

$$\begin{bmatrix} v_x(t) \\ v_y(t) \end{bmatrix} = \begin{bmatrix} \frac{dx}{dt} \\ \frac{dy}{dt} \end{bmatrix} = -\frac{F}{\sqrt{1+\varepsilon^2}} \int \begin{bmatrix} cos(\omega t') \\ \varepsilon\, sin(\omega t') \end{bmatrix} dt' \quad 4.4$$

and

$$\begin{bmatrix} v_x(t) \\ v_y(t) \end{bmatrix} = -\frac{F}{\sqrt{1+\varepsilon^2}} \begin{bmatrix} \frac{sin(\omega t)}{\omega} \\ -\frac{\varepsilon\, cos(\omega t)}{\omega} \end{bmatrix} + \begin{bmatrix} c_1 \\ c_2 \end{bmatrix}, \quad 4.5$$

where c_1 and c_2 are constants of integration and depend on initial conditions. From the initial condition $v_x(t = t_0) = v_{x0}$ and $v_y(t = t_0) = v_{y0}$, we get

$$\begin{bmatrix} v_x(t) \\ v_y(t) \end{bmatrix} = -\frac{F}{\sqrt{1+\varepsilon^2}} \frac{1}{\omega} \begin{bmatrix} sin(\omega t) - sin(\omega t_0) \\ -\varepsilon\{cos(\omega t) - cos(\omega t_0)\} \end{bmatrix} + \begin{bmatrix} v_{x0} \\ v_{y0} \end{bmatrix}. \quad 4.6$$

Integration again with respect to time yields

$$\begin{bmatrix} x(t) \\ y(t) \end{bmatrix} = \int \left\{ -\frac{F}{\sqrt{1+\varepsilon^2}} \frac{1}{\omega} \begin{bmatrix} sin(\omega t') - sin(\omega t_0) \\ -\varepsilon\{cos(\omega t') - cos(\omega t_0)\} \end{bmatrix} + \begin{bmatrix} v_{x0} \\ v_{y0} \end{bmatrix} \right\} dt' \quad 4.7$$

and

$$\begin{bmatrix} x(t) \\ y(t) \end{bmatrix} = \frac{F}{\sqrt{1+\varepsilon^2}} \frac{1}{\omega^2} \begin{bmatrix} cos(\omega t) \\ \varepsilon\, sin(\omega t) \end{bmatrix} + t \begin{bmatrix} \frac{F}{\sqrt{1+\varepsilon^2}} \frac{1}{\omega} sin(\omega t_0) + v_{x0} \\ -\frac{F}{\sqrt{1+\varepsilon^2}} \frac{\varepsilon}{\omega} cos(\omega t_0) + v_{y0} \end{bmatrix} + \begin{bmatrix} c_3 \\ c_4 \end{bmatrix}, \quad 4.8$$

where c_3 and c_4 are constants of integration and depend on initial conditions. From the initial condition $x(t = t_0) = x_0$ and $y(t = t_0) = y_0$, we get

$$\begin{bmatrix} x(t) \\ y(t) \end{bmatrix} = \frac{F}{\sqrt{1+\varepsilon^2}} \frac{1}{\omega^2} \begin{bmatrix} cos(\omega t) - cos(\omega t_0) + \omega(t - t_0)\, sin(\omega t_0) \\ \varepsilon\, \{sin(\omega t) - sin(\omega t_0) - \omega(t - t_0)\, cos(\omega t_0)\} \end{bmatrix} + (t - t_0) \begin{bmatrix} v_{x0} \\ v_{y0} \end{bmatrix} + \begin{bmatrix} x_0 \\ y_0 \end{bmatrix}. \quad 4.9$$

When $x_0 = y_0 = 0$ then equation 4.9 becomes

$$\begin{bmatrix} x(t) \\ y(t) \end{bmatrix} = \frac{F}{\sqrt{1+\varepsilon^2}} \frac{1}{\omega^2} \begin{bmatrix} cos(\omega t) - cos(\omega t_0) + \omega(t - t_0)\, sin(\omega t_0) \\ \varepsilon\, \{sin(\omega t) - sin(\omega t_0) - \omega(t - t_0)\, cos(\omega t_0)\} \end{bmatrix} + (t - t_0) \begin{bmatrix} v_{x0} \\ v_{y0} \end{bmatrix}. \quad 4.10$$

Defining $tan(\alpha_0) = \varepsilon\, tan(\omega t_0)$;

$$\begin{bmatrix} v_{x0} \\ v_{y0} \end{bmatrix} = \boldsymbol{R}(-\alpha_0) \begin{bmatrix} v_{\parallel} \\ v_{\perp} \end{bmatrix} = \begin{bmatrix} v_{\parallel} cos(\alpha_0) + v_{\perp} sin(\alpha_0) \\ -v_{\parallel} sin(\alpha_0) + v_{\perp} cos(\alpha_0) \end{bmatrix} \quad 4.11$$

and

$$\vec{r}(t) =$$

$$\frac{F}{\sqrt{1+\varepsilon^2}} \frac{1}{\omega^2} \begin{bmatrix} cos(\omega t) - cos(\omega t_0) + \omega(t - t_0)\, sin(\omega t_0) \\ \varepsilon\, \{sin(\omega t) - sin(\omega t_0) - \omega(t - t_0)\, cos(\omega t_0)\} \end{bmatrix} +$$

$$(t-t_0)\begin{bmatrix} v_{\parallel}cos(\alpha_0)+v_{\perp}sin(\alpha_0) \\ -v_{\parallel}sin(\alpha_0)+v_{\perp}cos(\alpha_0)\end{bmatrix}.$$

4.12

When $v_{\parallel}=0$ then

$$\vec{r}(t)=\frac{F}{\sqrt{1+\varepsilon^2}}\frac{1}{\omega^2}\begin{bmatrix} cos(\omega t)-cos(\omega t_0)+\omega(t-t_0)\,sin(\omega t_0) \\ \varepsilon\{sin(\omega t)-sin(\omega t_0)-\omega(t-t_0)\,cos(\omega t_0)\}\end{bmatrix}+(t-t_0)\begin{bmatrix} v_{\perp}sin(\alpha_0) \\ v_{\perp}cos(\alpha_0)\end{bmatrix}.$$

4.13

At re-collision $\vec{r}(t=t_r)=0$

$$\begin{bmatrix}0\\0\end{bmatrix}=\frac{F}{\sqrt{1+\varepsilon^2}}\frac{1}{\omega^2}\begin{bmatrix} cos(\omega t_r)-cos(\omega t_0)+\omega(t_r-t_0)\,sin(\omega t_0) \\ \varepsilon\{sin(\omega t_r)-sin(\omega t_0)-\omega(t_r-t_0)\,cos(\omega t_0)\}\end{bmatrix}+(t_r-t_0)\begin{bmatrix} v_{\perp}sin(\alpha_0) \\ v_{\perp}cos(\alpha_0)\end{bmatrix}.$$

4.14

For the x-axis,

$$\frac{F}{\sqrt{1+\varepsilon^2}}\frac{1}{\omega^2}\,[cos(\omega t_r)-cos(\omega t_0)+\omega(t_r-t_0)\,sin(\omega t_0)]=-(t_r-t_0)v_{\perp}sin(\alpha_0). \qquad 4.15$$

The perpendicular component of the velocity $v_{\perp}$ can be derived as

$$v_{\perp}=-\frac{F}{\sqrt{1+\varepsilon^2}}\frac{1}{\omega\,sin(\alpha_0)}\left[\frac{cos(\omega t_r)-cos(\omega t_0)}{\omega(t_r-t_0)}+sin(\omega t_0)\right], \qquad 4.16$$

and for the y-axis

$$\frac{F}{\sqrt{1+\varepsilon^2}}\frac{\varepsilon}{\omega^2}[sin(\omega t_r)-sin(\omega t_0)-\omega(t_r-t_0)\,cos(\omega t_0)]=-(t_r-t_0)v_{\perp}cos(\alpha_0).$$

4.17

The perpendicular component of the velocity $v_{\perp}$ can also be derived as

$$v_{\perp}=-\frac{F}{\sqrt{1+\varepsilon^2}}\frac{\varepsilon}{\omega\,cos(\alpha_0)}\left[\frac{sin(\omega t_r)-sin(\omega t_0)}{\omega(t_r-t_0)}-cos(\omega t_0)\right]. \qquad 4.18$$

Comparing equation 4.16 and 4.18, and since $tan(\alpha_0)=\varepsilon\,tan(\omega t_0)$, we get

$$-cos(\omega t_0)\,[cos(\omega t_r)-cos(\omega t_0)+\omega(t_r-t_0)sin(\omega t_0)] = -\varepsilon^2\,sin(\omega t_0)[sin(\omega t_r)-sin(\omega t_0)-\omega(t_r-t_0)cos(\omega t_0)]$$

4.19

and

$$cos(\omega t_0)[cos(\omega t_r)-cos(\omega t_0)]+\omega(t_r-t_0)sin(\omega t_0)cos(\omega t_0) = \varepsilon^2\,sin(\omega t_0)[sin(\omega t_r)-sin(\omega t_0)]-\varepsilon^2\omega(t_r-t_0)\,sin(\omega t_0)cos(\omega t_0).$$

4.20

After further simplification we get

$$(1+\varepsilon^2)\omega(t_r-t_0)sin(\omega t_0)cos(\omega t_0)+cos(\omega t_0)[cos(\omega t_r)-cos(\omega t_0)] - \varepsilon^2\, sin(\omega t_0)[sin(\omega t_r)-sin(\omega t_0)]=0,$$

4.21

which relates re-collision time t_r with the birth time t_0 of the electron. This is the return condition for an elliptically polarized driving field and can be solved numerically to get the return time t_r from the birth time t_0. In Figure 4-10(a) electron trajectory is plotted using equation 4.13 for $\varepsilon = 0.5$ and $v_\perp = 0$ and it can be seen that the electron does not return to the parent ion along the y-axis. However, in Figure 4-10(b), the electron returns to the parent ion for re-collision when the perpendicular displacement is compensated by $v_\perp$. The harmonic yield is related to the probability of electrons with perpendicular velocity $v_\perp$ which compensate the perpendicular displacement, which is related to the tunneling rate of electrons with $v_\perp$ normalized by the tunneling rate with $v_\perp = 0$. So, the harmonic yield with an elliptically polarized laser normalized to the yield with a linear polarized laser is

$$\frac{I_{XUV}(\varepsilon)}{I_{XUV}(\varepsilon=0)} \approx \frac{w(v_\perp)}{w(v_\perp=0)} = \exp\left(-\frac{\sqrt{2I_p}v_\perp(\varepsilon)^2}{|F(t_0)|}\right), \qquad 4.22$$

where $w(v_\perp)$ is the perpendicular velocity distribution that was predicted by tunneling theory [10] and was found to agree well with experimental results [11]. Here, I_p denotes the ionization potential and $|F(t_0)|$ is the absolute value of the driving field at the instant of ionization [12].

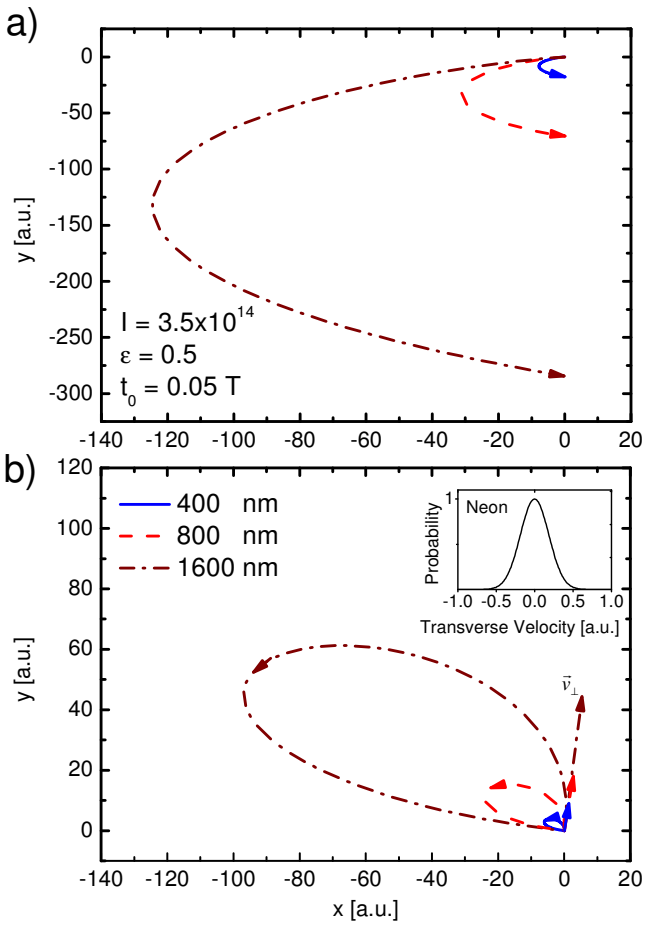

Figure 4-10 (a) Electron trajectories in elliptically polarized fields ($\varepsilon = 0.5$) driven by 400 (blue continuous), 800 (red dashed) and 1600nm (purple dot dashed) wavelengths at zero initial perpendicular velocity. Here, the birth time is $t_0 = 0.05 \cdot T$ and I= $3.5\ 10^{14}$ W/cm^2 , (b) Perpendicular displacement is compensated by initial perpendicular velocity [12].

Experimental results

The schematic of the experimental setup for the measurement of ellipticity dependence of high harmonics is presented in Figure 4-11. The 895 μJ blue driving pulses were generated by SHG from 30 fs, 4.8 mJ red pulses from a kHz Ti:Sapphire regenerative amplifier using a 300 μm BBO crystal (Type 1 phase matching). Second harmonic blue pulses are separated from the fundamental by reflection from two dichroic mirrors at 45^o angle of incidence. To produce high harmonics, these blue pulses are focused onto a 1 mm long noble gas (helium, neon, etc.) filled gas cell using a 375 mm focal length concave mirror at near normal incidence. The blue pulses are separated from the high harmonics by a 300 nm thick aluminum filter and high harmonics are

diffracted from a 384 lines/mm grating and imaged by two micro-channel plates in a chevron configuration, phosphor screen and cooled CCD camera. A zero-order half-wave plate on a rotation stage and a quarter-wave plate with a fixed optical axis are used to change the ellipticity of the blue pulses while keeping the major axis of the ellipse normal to the grooves of the grating. This is used to minimize the effect due to the ellipticity dependent gain of the grating [13]. The ellipticity dependence of the harmonics from the red pulses is also measured with a similar setup, but the optics are replaced with those for 800 nm. The ellipticity dependence of the 11th harmonic from the blue driving pulses is compared with the 19th harmonic from the red driving pulses at an intensity of 7.7x10^{14} W/cm^2 in Figure 4-12. The numerically calculated ellipticity dependence using equation 4.22, 4.21 and 4.16 is also plotted in Figure 4-12. Good agreement between experiment and theory is evident.

An analytical expression $v_\perp = -\beta F \varepsilon \lambda / 2\pi c$ can be obtained from equation 4.16 for small ellipticity ($\varepsilon^2 \ll 1$), $\cos\alpha_0 = \cos(\tan^{-1}(\varepsilon \tan(\omega t_0))) \approx 1$ and $|F(t_0)| \approx \sqrt{I}$, where $\beta = \left(\frac{\sin\omega t_r - \sin\omega t_0}{\omega(t_r - t_0)} - \cos\omega t_0\right)$ and c is the speed of light. Equation 4.5 can be approximated as

$$\frac{I_{XUV}(\varepsilon)}{I_{XUV}(\varepsilon=0)} \approx \exp\left(-\frac{\beta^2\sqrt{2I_p I}}{4\pi^2 c^2}\lambda^2\varepsilon^2\right). \qquad 4.23$$

In Figure 4-13 (a) and (b) the experimentally measured ellipticity dependence is compared with numerical and approximate results for the 27th harmonic from red pulses and the 11th harmonic from blue pulses, respectively, at an intensity of 5.4x10^{14} W/cm^2 in neon and, in Figure 4-13 (c) and (d), for the 19th harmonic of red pulses and the 11th harmonic of blue pulses, respectively, at an intensity of 7.7x10^{14} W/cm^2 in helium. A good fit of numerical results to experiment is evident and deviation of approximate results from experiment at larger ellipticity is due to the fact that the conditions of approximation are not valid at large ellipticity.

A typical parameter used in optical gating is threshold ellipticity ε_{th} , which is the ellipticity at which harmonic yield drops by one order of magnitude. For the cutoff harmonic $\beta^2 \approx 1.59$, and equation 4.23 can be used to derive an expression for ε_{th} ,

$$\varepsilon_{th} \approx \frac{691}{{I_p}^{1/4}} \frac{1}{I^{1/4}} \frac{1}{\lambda}. \qquad 4.24$$

We compare threshold ellipticity of various harmonic orders generated from neon using red and blue pulses in Figure 4-14 (a) and (b), respectively, and for various intensities in Figure 4-14 (c). Additionally, threshold ellipticity as a function of wavelength is compared with the theoretical results of other groups in Figure 4-14 (d). It can be seen that threshold ellipticity reduces with increasing wavelength, making optical gating like PG, DOG and GDOG easier and allowing shorter attosecond pulses to be achieved with longer wavelengths. However, getting intense attosecond pulses using shorter wavelengths poses a challenge for gating due to larger threshold ellipticity. In Chapter 6, we propose a scheme for GDOG which can be used to gate using short wavelength driving lasers.

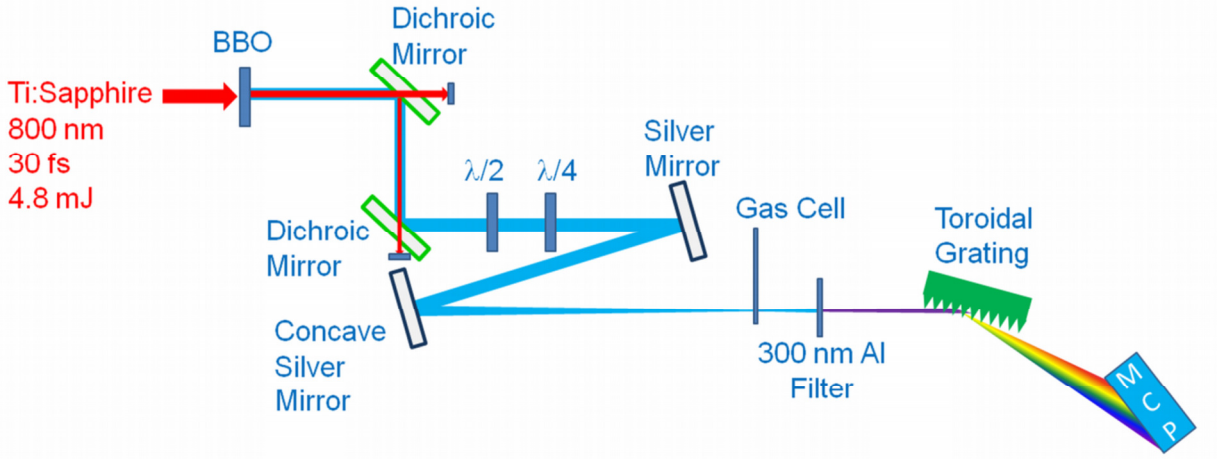

Figure 4-11 Schematic of the experimental setup used for the measurement of the ellipticity dependence [14].

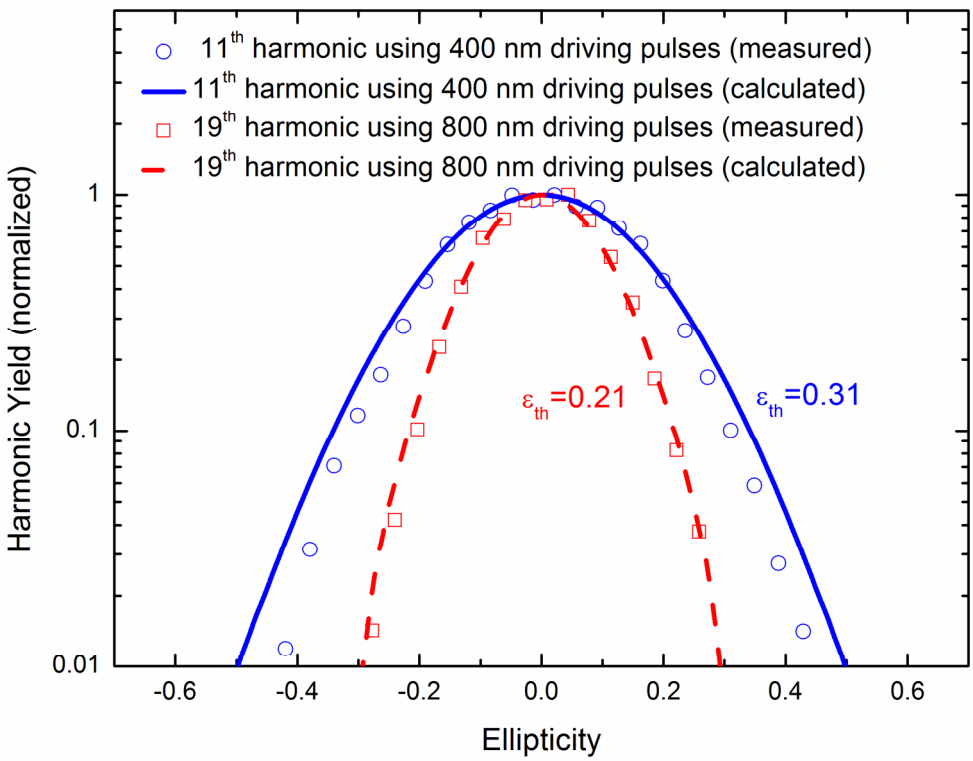

Figure 4-12 Ellipticity dependence of 11^{th} harmonic driven by blue pulses and 19^{th} harmonic driven by red pulses in helium at an intensity of 7.7×10^{14} W/cm^2 [14].

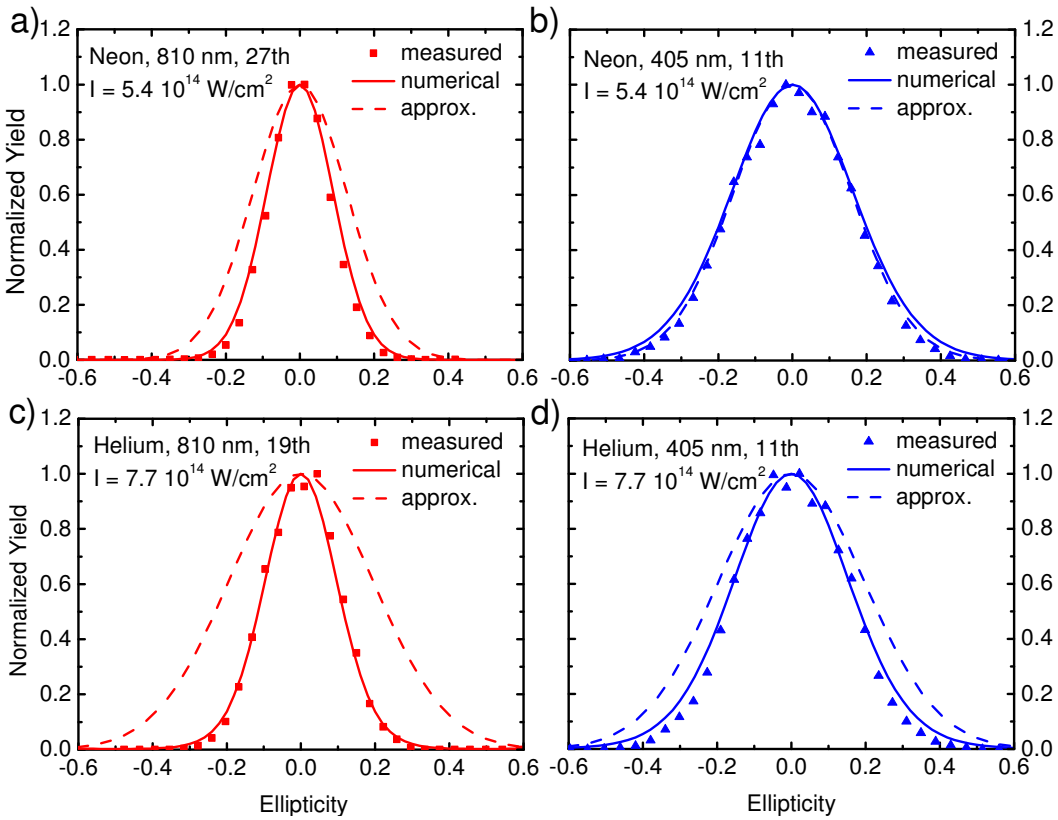

Figure 4-13 Ellipticity dependence of neon and helium driven by red and blue pulses [12].

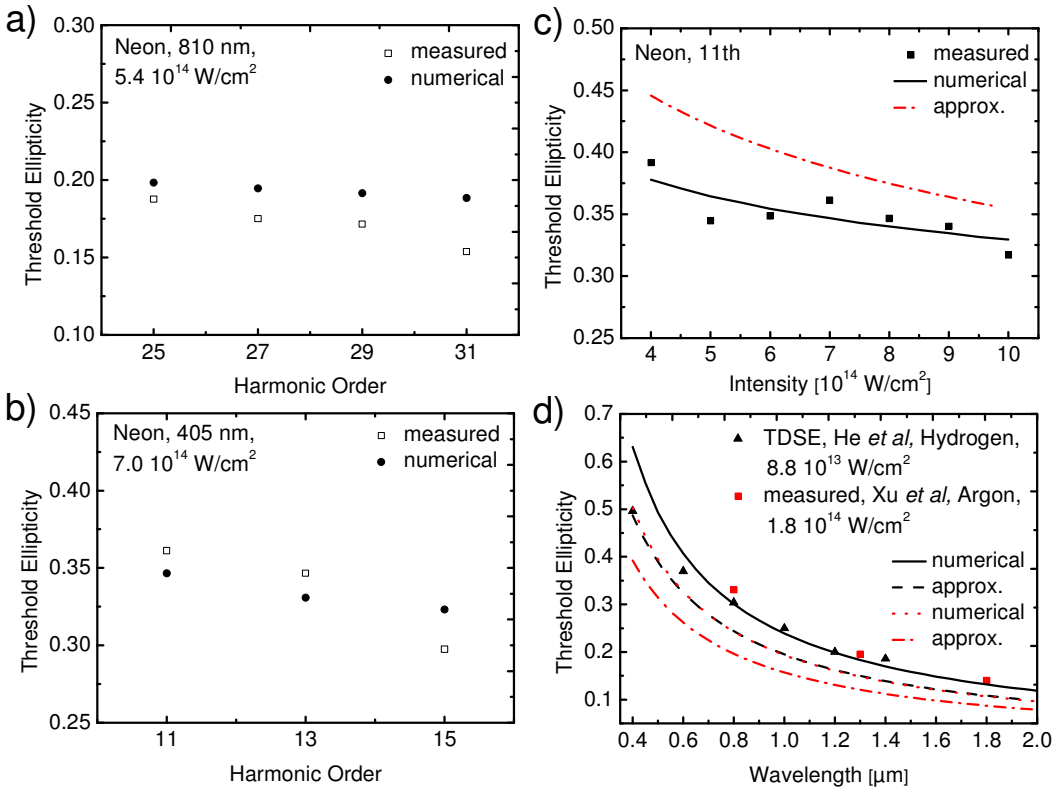

Figure 4-14 Threshold ellipticity as a function of harmonic order (a) and (b) for red and blue driving pulses respectively, intensity (c) and wavelength (d) [12].

High harmonics generation from solid targets using 400 nm pulses

In an attempt to scale attosecond flux further, we also generated high harmonics using blue driving pulses from carbon plasmas in collaboration with the team from ALLS, INRS, Canada, using a scheme similar to the one discussed in Chapter 2 for red driving pulses. However, instead of using uncompressed and compressed pulses to generate harmonics from plasmas, we used compressed beam from the MARS laser system. The experimental setup is presented in Figure 4-15. A half wave plate is used to control the polarization of the red pulses at the BBO entrance. A 300 μm BBO with type 1 phase matching is used to generate long blue pulses, the transform limited pulse duration of the blue pulses was estimated to be ~55 fs. The leftover fundamental from the BBO is separated from second harmonic by the first dichroic mirror and is used as the pre-pulse (for surface ablation). The 1.8 mJ, 800 nm pre-pulse is focused on the graphite target surface using a 400 mm focal length fused silica lens. The pre-pulse passed through several millimeters of fused silica in the dichroic mirror and fused silica

lens, making it highly chirped and long. The repetition rate of the pre-pulse was reduced to 100 Hz using a mechanical shutter in order to stabilize the plasma. The blue pulse from the two dichroic mirrors is propagated through a long delay line to make it come 19 ns later than the pre-pulse. One key advantage of using this scheme instead of a 50/50 beamsplitter before the compressor is that the highest blue pulse energy is achieved and the leftover red pulse after second harmonic generation is reused. Additionally, the high harmonics produced were much more stable than in the previous experiment discussed in Chapter 2.

Figure 4-16 presents a schematic showing the position of the main and pre-pulse with respect to the target and defines the coordinate axes. For phase matching, the first delay between the pre- and main-pulse was scanned from 5 to 50 ns and the highest efficiency was achieved at 19 ns. The results are presented in Figure 4-17. Next, the position of the pre-pulse with respect to the target was scanned using two micrometer translation stages along the z' and y' directions. Since the ablated plasma is cylindrically symmetric making x' and y' symmetric axes. The target was at 0 mm along the z' axis and the plasma center was at ~5.4 mm along the y' axis. The target position was determined by translating it along the z' axis to block the main pulse. The harmonic yield as a function of z' and y' is presented in Figures 4-18 and 4-19, respectively. Next y' and z' were fixed at a position to get the highest harmonic yield, and the position of the main pulse was scanned across the plasma along the z-axis. The harmonic yield as a function of the main pulse position is presented in Figure 4-20. The double hump structure in Figure 4-17 and 4-18 may be associated with the contribution of two species towards high harmonic generation, like single atom/ions (faster species) and neutral nano-clusters (slower species). However, a more systematic set of experiments with better plasma diagnostics is required to prove this point. Our collaborators at ALLS, INRS are in the process of planning such experiments with help from theoretical plasma simulations which are currently being carried out.

To compare photon flux, we compare the 7^{th} harmonic generated from argon gas at 30 Torr and a carbon target using blue driving pulses with 921 μJ energy at the gas cell or at the plasma. The high harmonic spectra are presented in Figure 4-21 (a) and (b), respectively. Additionally, a carbon harmonics spectrum driven by red pulses under the same pre- and main-pulse energy is presented in Figure 4-21(c). Based on the area under the curve, harmonic yield for the 7^{th} order from carbon is ~1.8 times more intense than that from argon driven by blue

pulses. However, the carbon harmonic yield driven by blue pulses is ~1.1 times more intense than that driven by red pulses. As evident from Figure 4-21, the divergence of carbon harmonics is quite large as compared to that from argon. We attribute low photon flux for carbon harmonics driven by blue pulses to the lack of pulse energy in the pre-pulse, which leads to lower plasma density.

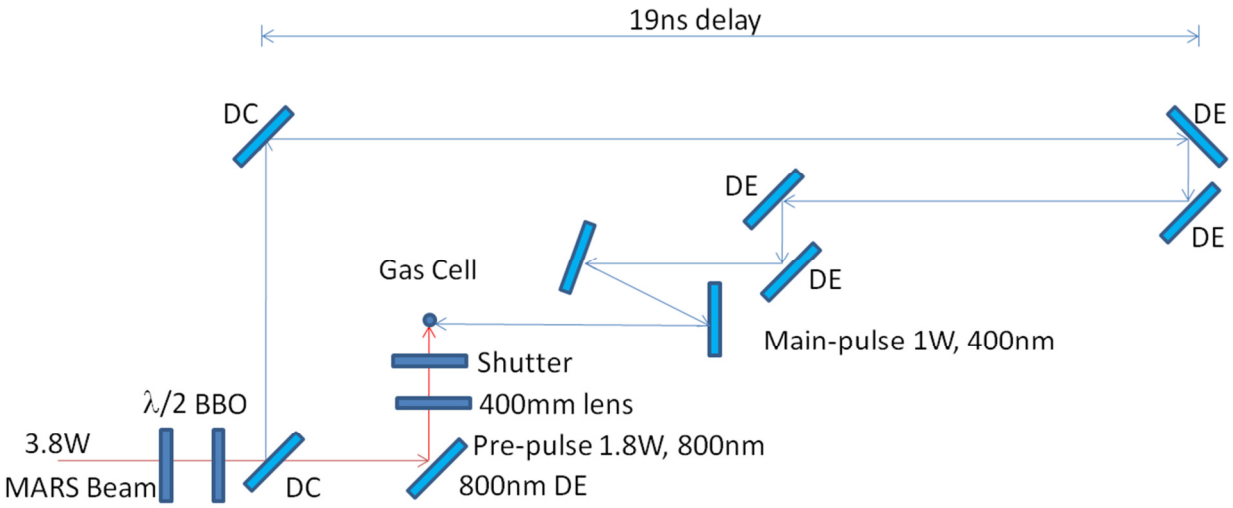

Figure 4-15 Schematic for the high harmonics generated from laser ablated carbon plasma driven by blue pulses.

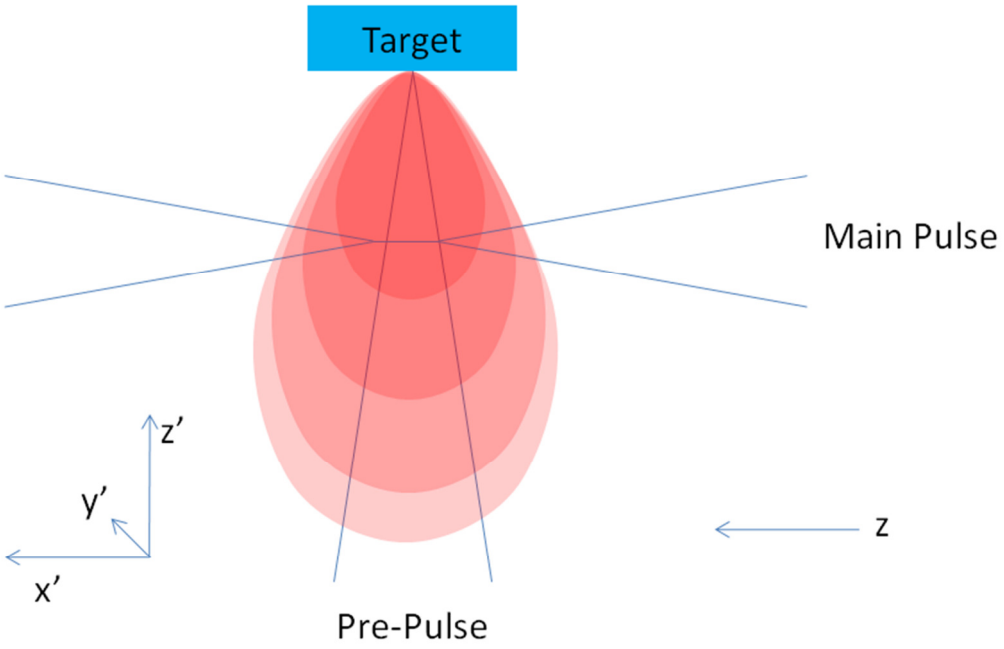

Figure 4-16 Schematic to illustrate plasma generated from surface ablation of carbon target by red pre-pulse and generation of high harmonics by the blue main pulse.

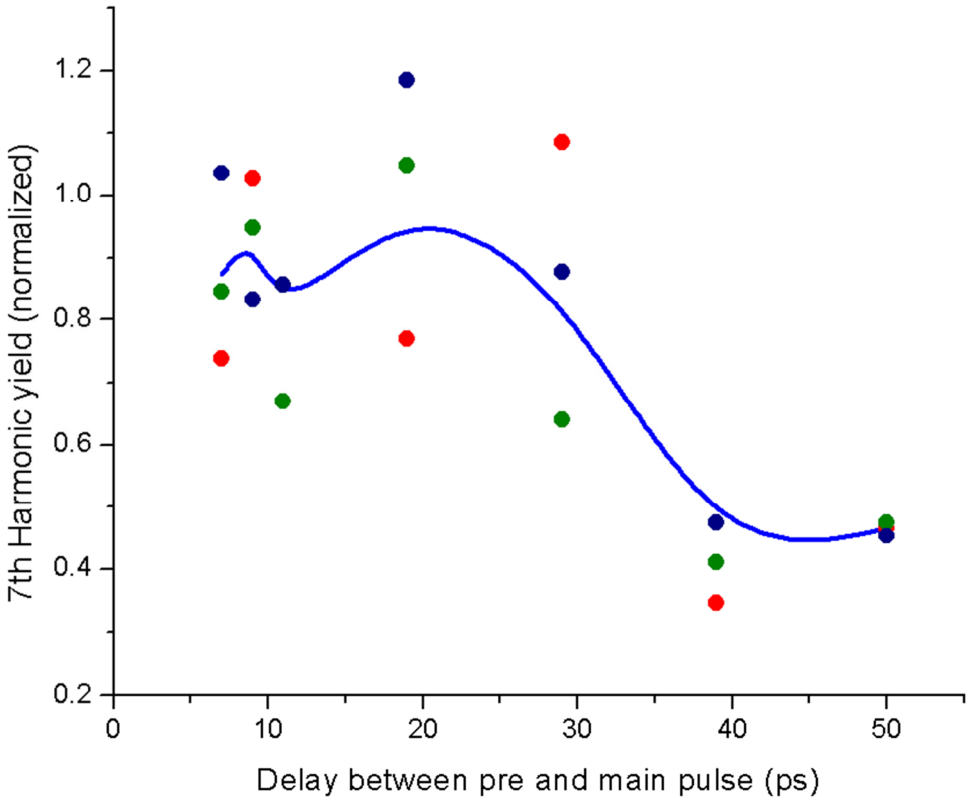

Figure 4-17 Harmonic efficiency of 7th order as a function of delay between pre and main pulse at three different trials (indicated by circles, fitted by a spline curve).

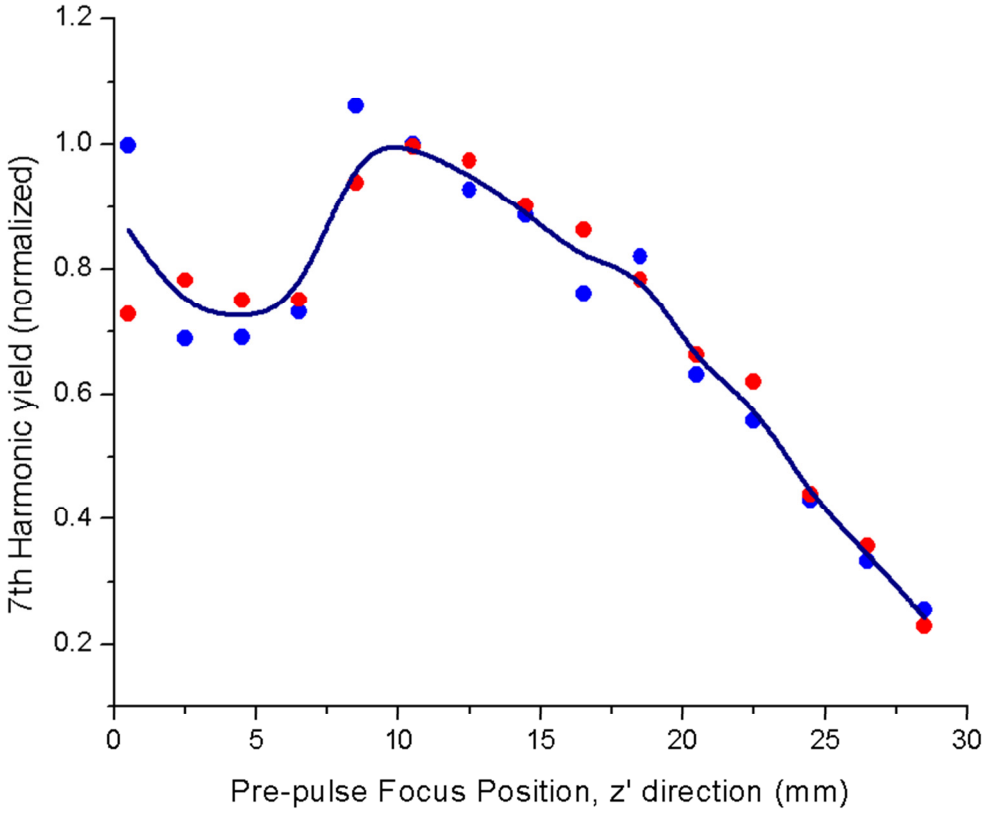

Figure 4-18 Harmonic efficiency of the 7th order as a function of pre-pulse focus position along the z' axis, which controls the amount of ablation from the target, for three different trials (indicated by circles, fitted by a spline curve). z'=0 indicates roughly the surface of the carbon target.

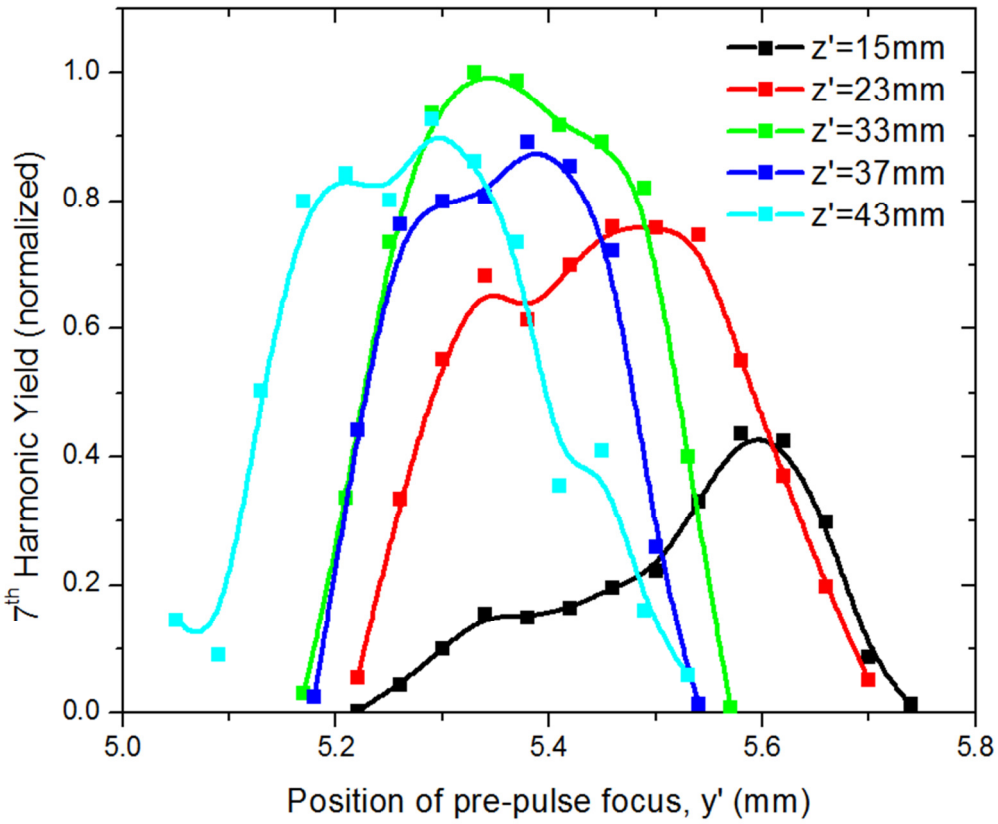

Figure 4-19 Harmonic efficiency of the 7th order as a function of pre-pulse focus position along the y' axis. y' =5.4 mm is roughly the position of main pulse.

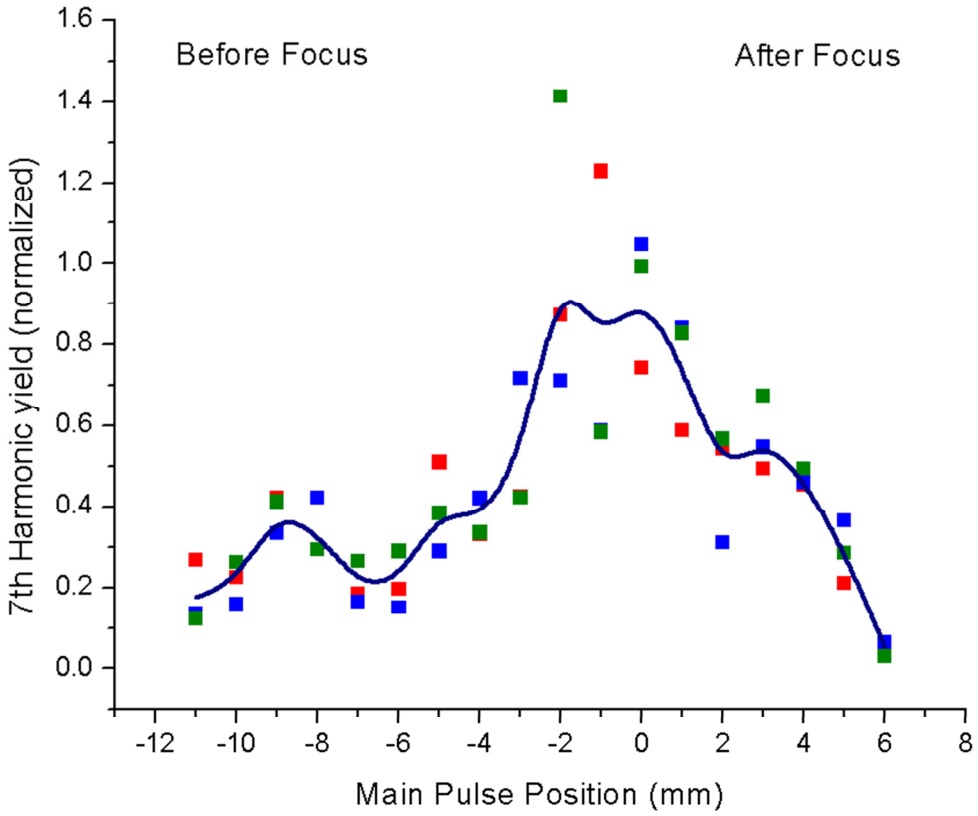

Figure 4-20 Harmonic efficiency of the 7th order as a function of main pulse focus position for three different trials (indicated by circles, fitted by a spline curve). 0 mm indicates the focus position.

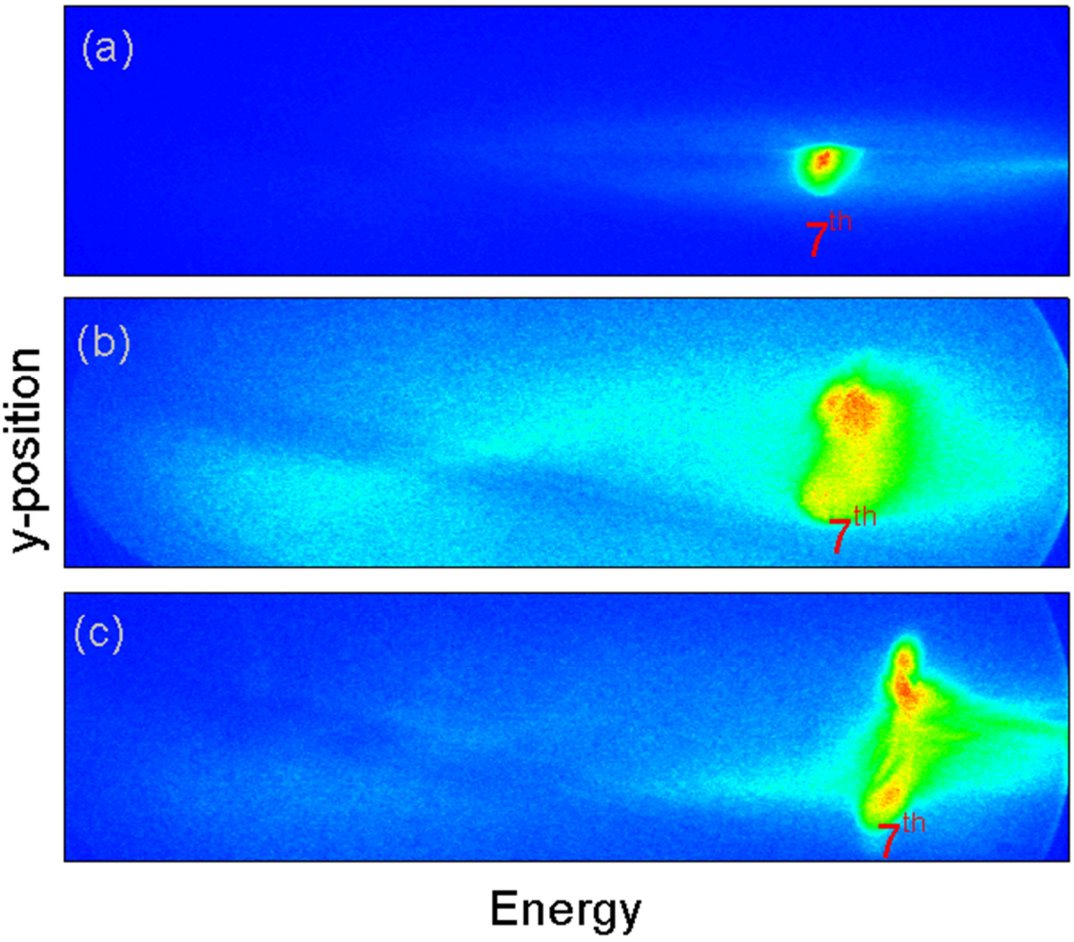

Figure 4-21 High harmonic spectra generated from argon (a) and carbon plasma (b) driven by blue pulses compared with high harmonics from carbon plasma driven by red pulses (c). (Color scale is normalized)

References

[1] H. Mashiko, S. Gilbertson, C. Li, E. Moon, and Z. Chang, Phys. Rev. A 77, 063423 (2008).

[2] F. Ferrari, F. Calegari, M. Lucchini, C. Vozzi, S. Stagira, G. Sansone and M. Nisoli, "High-energy isolated attosecond pulses generated by above-saturation few-cycle fields", Nature Photonics 4, 875 (2010).

[3] E. L. Falcão-Filho, V. M. Gkortsas, A. Gordon & F. X. Kärtner, "Analytic scaling analysis of high harmonic generation conversion efficiency", Opt. Express 17, 11217 (2009).

[4] 11. E. L. Falcão-Filho, C. Lai, K. Hong, V. M. Gkortsas, S. Huang, L. Chen & F. X. Kärtner, “Scaling of high-order harmonic efficiencies with visible wavelength drivers: A route to efficient extreme ultraviolet sources”, Appl. Phys. Lett. 97, 061107 (2007).
[5] Private communication with EKSMA Optics and Altos Photonics.
[6] http://www.semrock.com/Data/Sites/1/semrockpdfs/whitepaper_flatnessofdichroicbeamsplittersaffectsfocusandimagequality_web.pdf
[7] Private communication with CVI Melles Griot
[8] https://www.cvimellesgriot.com/Products/Mirrors.aspx
[9] R. W. Boyd, "Nonlinear Optics", Academic Press, ISBN: 978-0-12-369470-6 (2008).
[10] M. Y. Ivanov, M. Spanner, O. Smirnova, “Anatomy of Strong Field Ionization”, J. Mod. Optics, 52, 165-184, (2005).
[11] L. Arrissian, C. Smeenk, F. Turner, C. Trallero, A. V. Sokolov, D. M. Villeneuve, A. Staudte, P. B. Corkum, “Direct Test of Laser Tunneling with Electron Momentum Imaging”, Phys. Rev. Lett., 105, 133002 (2010).
[12] M. Möller, S.. D. Khan, Y. Cheng, B. Zhao, K. Zhao, M. Chini, G. G. Paulus and Z. Chang, "Dependence of high harmonic generation yield on driving-laser ellipticity", Physical Review A (submitted).
[13] Z. Chang, Fundamentals of Attosecond Optics, CRC Press; 1 edition (February 16, 2011) ISBN-10: 1420089374.
[14] S. D. Khan, Y. Cheng, M. Möller, K. Zhao, B. Zhao, M. Chini, G.. G. Paulus and Z. Chang, "Ellipticity dependence of 400 nm-driven high harmonic generation", App. Phys. Lett., 99, 161106 (2011).

Chapter 5 - Compression of 400nm pulses

In this chapter, we review compression of ~55 fs (long pulses), 400 nm (blue pulses) into < 11 fs pulses (short pulses) by self phase modulation in a neon filled hollow core fiber and chirp mirrors. Additionally, we discuss the details of self-diffraction FROG to characterize long and short blue pulses.

Hollow core fiber to get broad spectrum

The long pulse from the MARS laser system is frequency doubled by a 300 µm BBO (Type 1 phase matching), and long blue pulses are separated from the fundamental by reflection from two dichroic mirrors (discussed in detail in Chapter 4). The chirp of long blue pulses after the dichroic mirrors is pre-compensated by reflection from two chirp mirrors (-50 fs^2 per mirror). The negatively chirped long pulses are reflected from a 1.5 m focal length aluminum mirror and are focused into a 400 µm inner diameter borosilicate hollow core fiber filled with neon at 30 psi by transmission through a 0.5 mm fused silica window. Bandwidth of the input pulse is ~5 nm which is increased to > 23 nm through self phase modulation. The output spectrum from the fiber is presented in Figure 5-1, which corresponds to a transform limited pulse duration of 10.5 fs. The output pulse from the hollow core fiber is collimated by a 3 m focal length aluminum mirror after transmission through a 0.5 mm fused silica window. Due to limited space on the optics table, a normal incidence TLM1-400 flat mirror is used between the output window and the collimating mirror to fold the beam path. The collimated beam is reflected from 6 chirp mirrors after a 45^o reflection from two TLM1-400 mirrors. The through-put of the fiber was > 40% and the output pulse energy was ~250 µJ, which is the highest achieved pulse energy from a hollow core fiber setup at 400 nm, <11 fs. Previously, the highest reported pulse energy was 80 µJ before the chirp mirrors for sub-8 fs pulses, which was not enough for optical gating to produce single attosecond pulses [1]. Additionally Liu et al. reported 45 µJ before the chirp mirrors for sub-8 fs pulses [2,3]. Higher energy coupling from the hollow core fiber and design of suitable chirp mirrors in this wavelength range appears to be the major bottleneck towards intense short blue pulses. We have solved the first issue by demonstrating > 40% fiber throughput with an output pulse energy of ~250 µJ. However, compensation of chirp with suitable chirp mirrors is still a challenge.

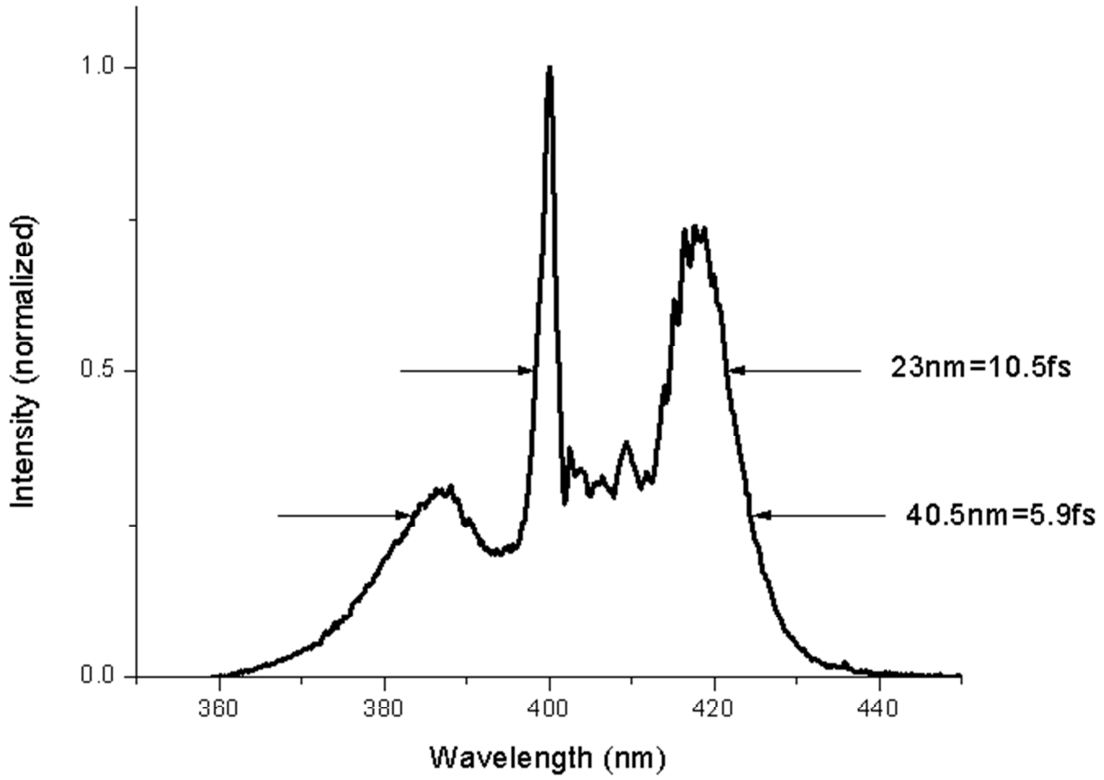

Figure 5-1 Spectrum after 400 µm inner diameter borosilicate hollow core fiber filled with 30 psi neon.

400nm chirp mirrors to compress pulses

We used 4 pairs of chirp mirrors, 1 pair before the fiber for pre-compensation and 3 pairs after the fiber, to compensate positive chirp added into the broad bandwidth produced during self-phase modulation. The mirrors have >99% reflectivity from 380 to 425 nm. The group delay dispersion added by one chirp mirror is presented in Figure 5-2. These are double chirp mirrors, i.e. one chirp mirror is equal to a pair of conventional chirp mirrors and are not oscillation compensated. The average GDD of each mirror reflection is -50 fs^2 and the modulation is +/- 5 fs^2 (around 10%), which is the best available with the current technology in this wavelength range.

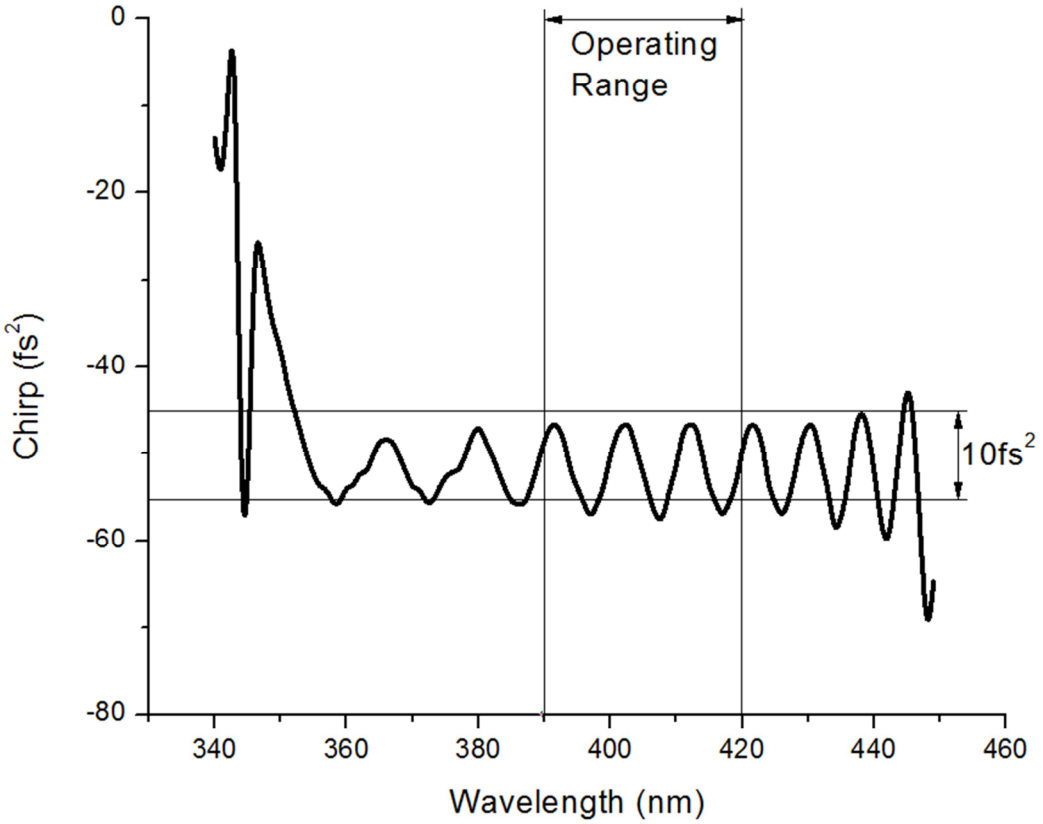

Figure 5-2 GDD introduced by chirp mirror [4].

High harmonic generation using 400nm short pulses

We generated high harmonics from 1 to 6 reflections from chirp mirrors. The high harmonic spectra are presented in Figure 5-3, where the 7th harmonic driven by blue short pulses is clearly visible. In Figure 5-4, we present the harmonic yield of 7th harmonic as a function of the number of reflections from chirp mirrors. We see a strong harmonic peak at 5 reflections from the chirp mirrors, which indicate best pulse duration.

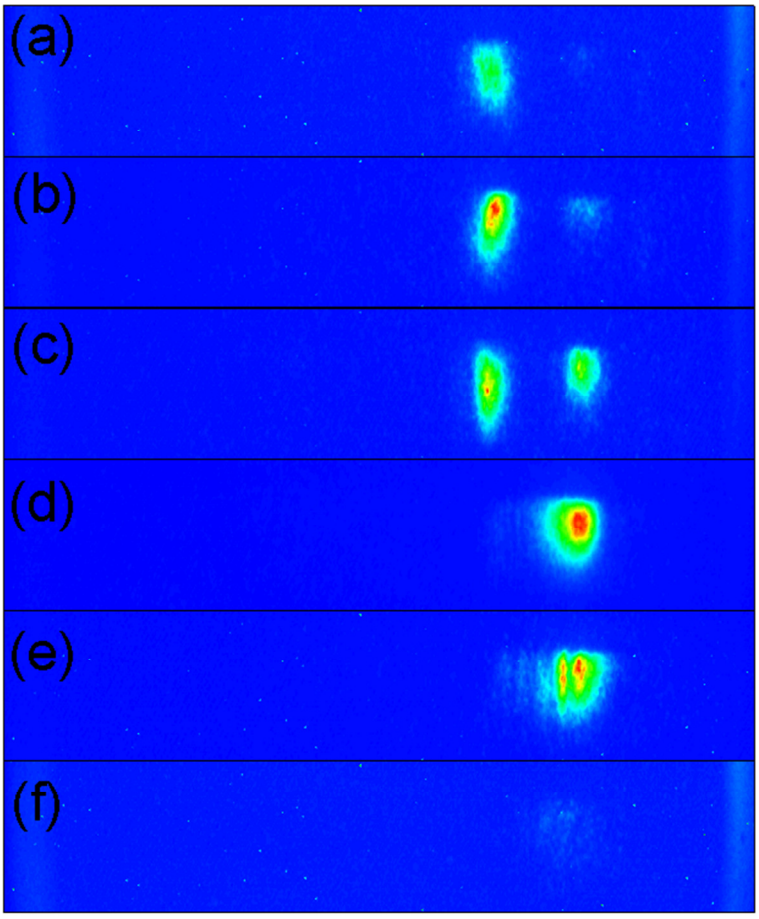

Figure 5-3 High harmonic spectrum driven by short blue pulses compressed by hollow core fiber and 6 (a), 8 (b), 10 (c), 12 (d), 14 (e) and 16 (f) chirp mirrors.

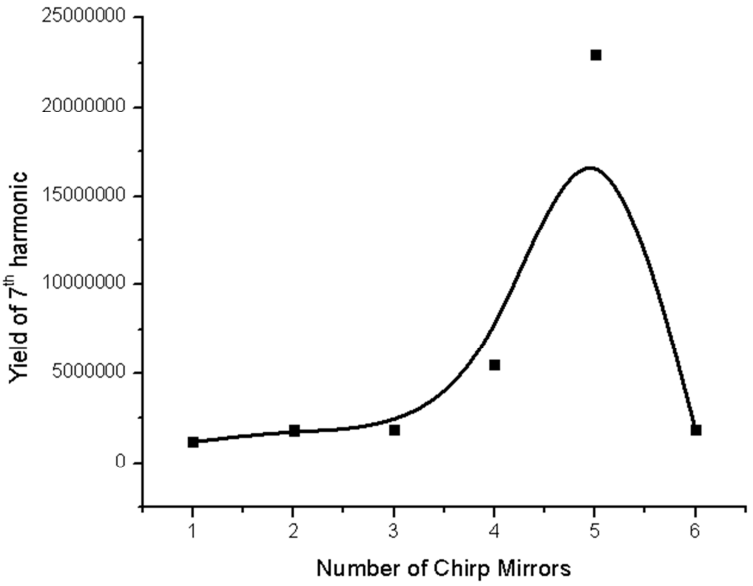

Figure 5-4 Yield of 7th harmonic driven (filled squares, fitted by a spline curve) by blue short pulse compressed by hollow core fiber and chirp mirrors.

Pulse characterization with SD-FROG

To characterize short blue pulses we developed a FROG setup based on self-diffraction [5, 6, 7]. We selected SD-FROG over SHG-FROG due to the lack of availability of non-linear crystals to phase match frequency doubling from 400 nm to 200 nm. However, due to the requirement of high intensity at the nonlinear crystal to exhibit self-diffraction, we used a 500 mm aluminum focusing mirror, due to which we were limited to the scanning FROG configuration instead of the single-shot configuration. For the nonlinear crystal we used a 111 µm thick quartz (n_2=1.06 for o-ray, 1.13 for e-ray at 1064 nm) with broadband anti-reflection coating for 400 nm. The schematic of the SD-FROG setup is presented in Figure 5-5. The incoming beam is split by a D-shaped aluminum mirror. Both the transmitted and reflected beams goes through two delay stages and are recombined on a 1"(25.4 mm) aluminum mirror and focused by another 1"(25.4 mm) aluminum 500 mm concave mirror. A microscope objective and CCD camera (not shown in the schematic) are used to image the overlap of the focus spots from two legs on the nonlinear medium. The delay stage on the transmitted leg is fixed with a 45 µm scanning range PZT actuator in addition to a manual translation stage. First, spatial overlap between the two legs is achieved on the surface of the nonlinear medium by using the microscope objective and CCD camera, and then time overlap is achieved through the manual

translation stage on the transmitted leg until self-diffraction is observed after the nonlinear medium. Once self-diffraction is achieved fine spatial and temporal overlap is optimized iteratively until the highest yield of the self-diffraction beam is observed. A USB-based CCD spectrometer with fiber optic cable (Ocean Optics Inc. HR2000+, range 199 to 644 nm) is used to measure the spectrum of the self-diffraction beam. The PZT actuator is scanned from 0 to 300 fs by a Labview Program and the spectrum at each delay is captured by the Labview Program and displayed as a FROG trace. The scanning FROG takes 10 to 20 minutes for one FROG trace depending on the resolution of the PZT actuator. A commercial FROG3 program from FemtoSoft / Swamp Optics is used to re-construct intensity and phase from the SD-FROG trace.

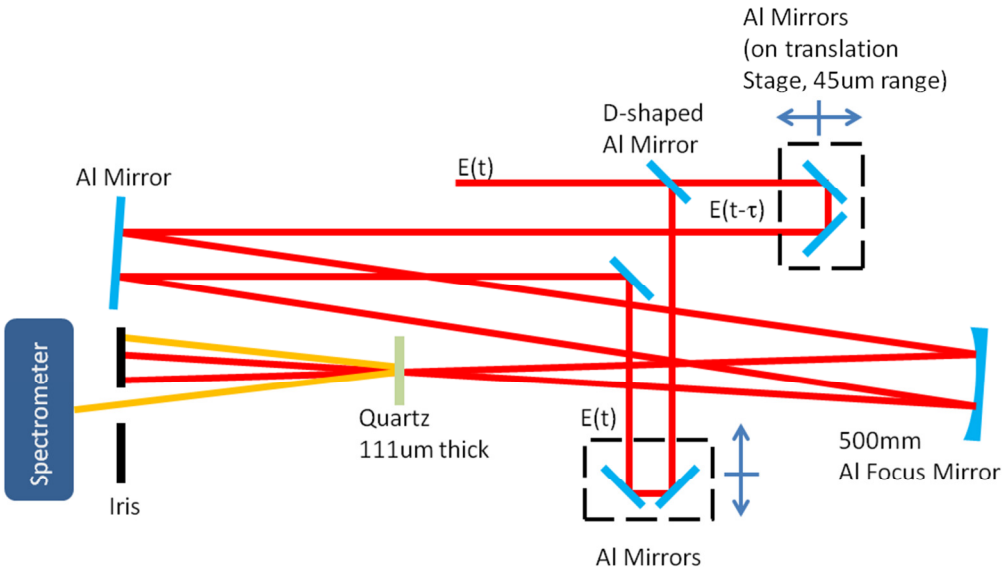

Figure 5-5 Schematic of experimental setup of D-shaped mirror based SD-FROG.

In Figure 5-6(a), we present the FROG trace after the fiber and the marginal is presented in Figure 5-6(b). A good agreement of the marginal with the spectrum proves that the SD-FROG works. In Figures 5-7 and 5-8, we present the FROG traces after the fiber with and without chirp mirrors, it seems that with the addition of chirp mirrors the FROG trace gets further skewed, meaning the phase become worse with chirp mirrors. This is due to the fact that higher order chirp is present in the pulses after self-phase modulation in addition to 2^{nd} order chirp, which is compensated by the chirp mirrors. Further investigation reveals the dichroic and dielectric mirrors after the BBO used to separate red pulses from blue pulses appear to distort the phase, which is further amplified during self-phase modulation in the fiber. An experimentally

measured phase for dichroic and dielectric mirrors is not available from the manufacturer [8], and the manufacturer suspect the dichroic mirror to be the main culprit.

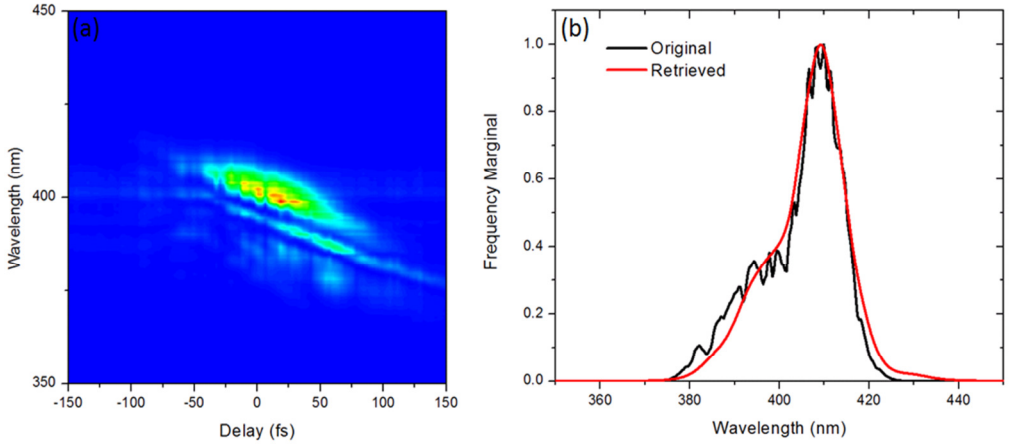

Figure 5-6 (a) SD-FROG spectrogram after hollow core fiber filled with 30 psi neon, with two chirp mirrors before fiber. (b) Marginal trace compared with experimentally obtained spectrum after fiber.

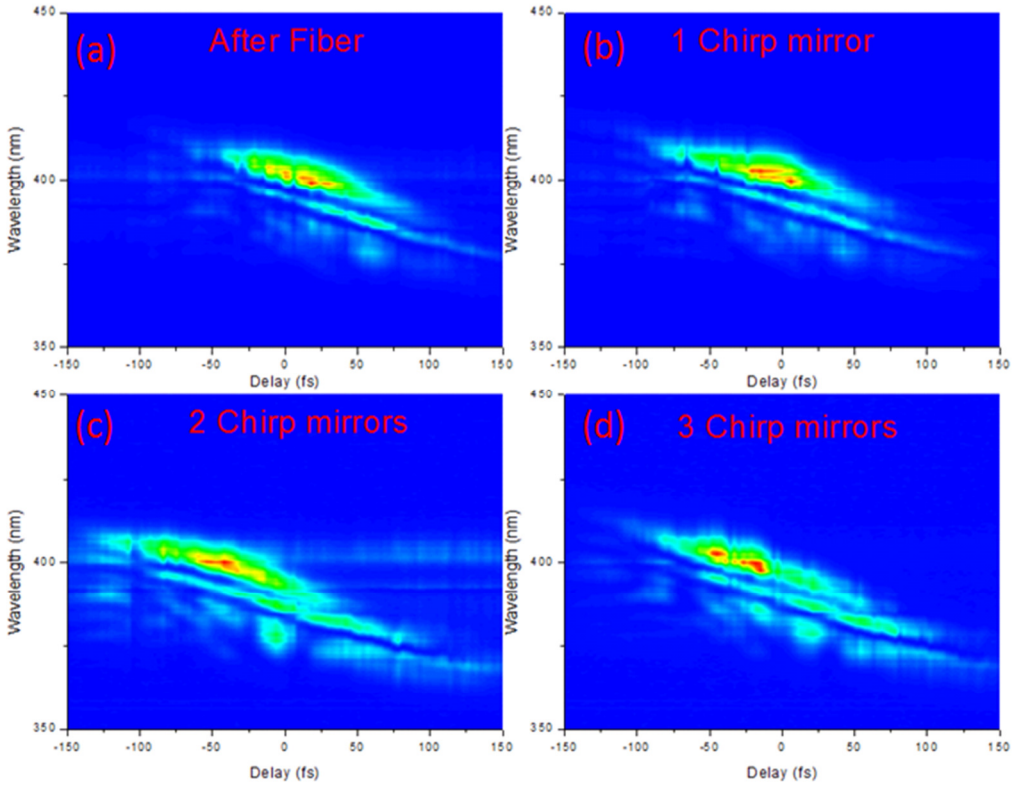

Figure 5-7 SD-FROG trace after fiber, 1, 2 and 3 chirp mirrors after fiber, 2 chirp mirror are added after the BBO and before the fiber for pre-compensation.

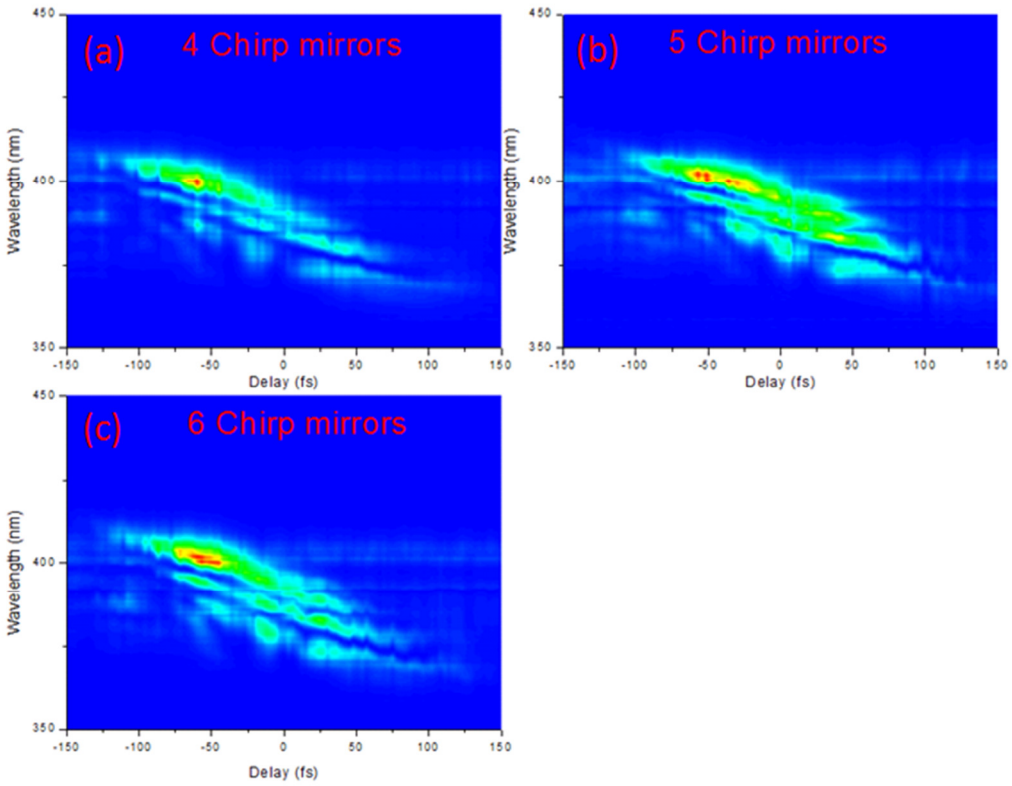

Figure 5-8 SD-FROG trace after fiber with 4, 5 and 6 chirp mirrors after fiber, 2 chirp mirrors are added after the BBO and before the fiber for pre-compensation.

References

[1] O. Dühr, E. T. J. Nibbering, G. Korn, G. Tempea and F. Krausz, "Generation of intense 8-fs pulses at 400 nm", Optics Letters, 24, 1, 34 (1999).

[2] J. Liu, Y. Kida, T. Teramoto and T. Kobayashi, "Generation of stable sub-10 fs pulses at 400 nm in a hollow fiber for UV pump-probe experiment", Optics Express, 18, 5, 4664 (2010).

[3] J. Liu, K. Okamura, Y. Kida, T. Teramoto and T. Kobayashi, "Clean sub-8-fs pulses at 400 nm generated by a hollow fiber compressor for ultraviolet ultrafast pump-probe spectroscopy", Optics Express, 18, 20, 20645(2010).

[4] Supplied by Ultra Fast Innovations Gmbh.

[5] Newport staff, "Application Note 33; Amplitude and Phase Characterization of Ultrashort Laser Pulses", Newport Corporation.

[6] D. J. Kane and R. Trebino, "Characterization of Arbitrary Femtosecond Pulses Using Frequency -Resolved Optical Gating", IEEE Journal of Quantum Electronics, 29, 2, 571 (1993).
[7] T. S. Clement, A. J. Taylor and D. J. Kane, "Single-shot measurement of the amplitude and phase of ultrashort laser pulses in the violet", Optics Letters, 20, 1, 70 (1995).
[8] Private communication with CVI Melles Griot.

Chapter 6 - Blue DOG/GDOG

In this chapter, we discuss the feasibility of PG, DOG and GDOG for extracting single attosecond pulses based on measured threshold ellipticity, which has already been discussed in Chapter 4. Since a nonlinear crystal is not available to frequency double 400 nm into 200 nm, we propose a new scheme for GDOG which can be used to extract single attosecond pulses from sub-10 fs blue pulses.

400 nm driven PG, DOG and GDOG

From the measurement of ellipticity dependence (discussed in detail in Chapter 4), $\varepsilon_{th} = 0.31$, $\varepsilon_{th} = 0.38$, $\varepsilon_{th} = 0.418$ for blue pulses in helium (I_o=7.7x10^{14} W/cm^2), neon (I_o=5.4x10^{14} W/cm^2) and argon (I_o=2.7x10^{14} W/cm^2), respectively. These are higher than that for red pulses ($\varepsilon_{th} = 0.21$, for helium). The gate width for PG, DOG and GDOG is given by

$$\delta t = \alpha \frac{\varepsilon_{th}}{\ln(2)} \frac{\tau_p^2}{T_d}, \qquad 6.1$$

where $\alpha = 1$ for PG and DOG and $\alpha = 0.5$ for GDOG and δt is the gate width which is equal to a half optical cycle for PG and full optical cycle for DOG and GDOG. The delay T_d between right and left circular pulses is given in Figure 6-1 as a function of pulse duration τ_p for PG, DOG and GDOG driven by blue pulses in helium. At 6.5 fs, the delay T_d is 28.5 fs for the PG case, which is very large compared to the pulse duration. Thus there is no overlap between the pulses in the linear gate part and hence no intensity within the gate to produce single attosecond pulses. On the other hand, for DOG and GDOG the delay T_d is 14.3 and 7.1 fs, respectively, at 6.5 fs pulse duration, which are comparable to the pulse duration and gating is possible. GDOG has a maximum intensity within the gate and hence we propose that it is suitable for optical gating to extract single attosecond pulses for sub-6.5 fs pulses. Furthermore, we present gas depletion (ionization probability) as a function of pulse duration in Figure 6-2 calculated using the ADK model[1] for DOG and GDOG in helium gas. The gas is 50% depleted at 8.5 fs in DOG and 12.8 fs in GDOG. Furthermore, gas depletion for DOG and GDOG is presented for various noble gases at the same intensity in Figure 6-3. Helium is suitable for generation of single attosecond

pulses from a pulse train driven by sub-10 fs blue pulses due to its higher ionization potential, which leads to less depletion.

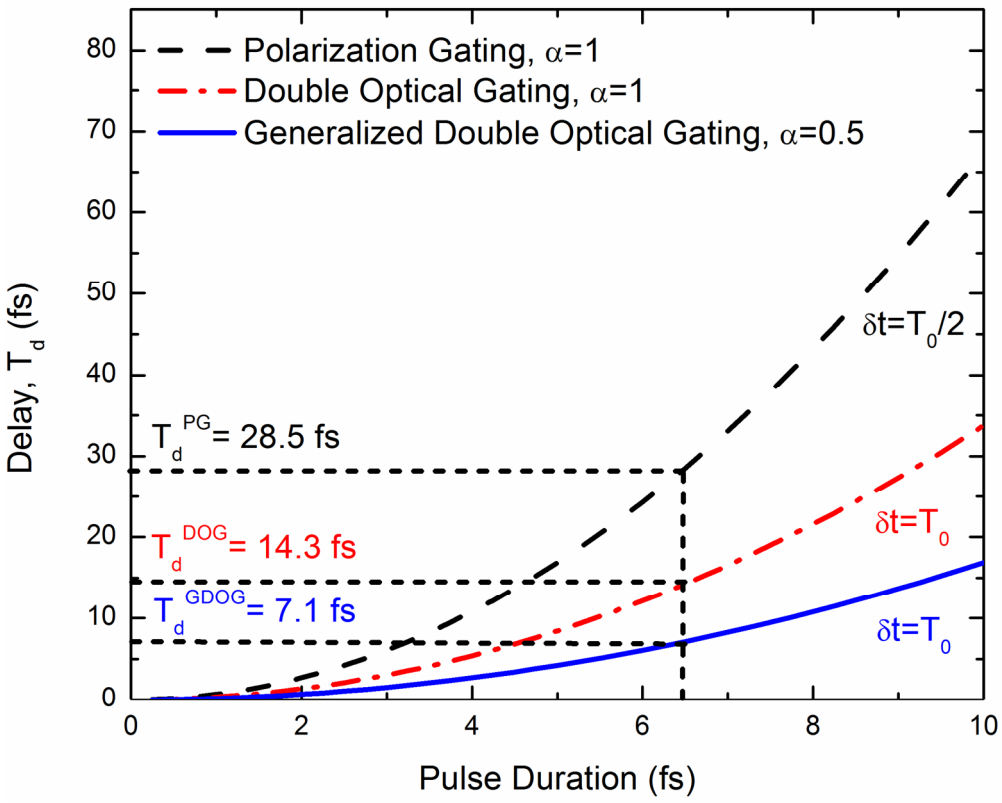

Figure 6-1 The delay between right and left circularly polarized pulses as a function of pulse duration for PG, DOG and GDOG driven by blue pulses [2].

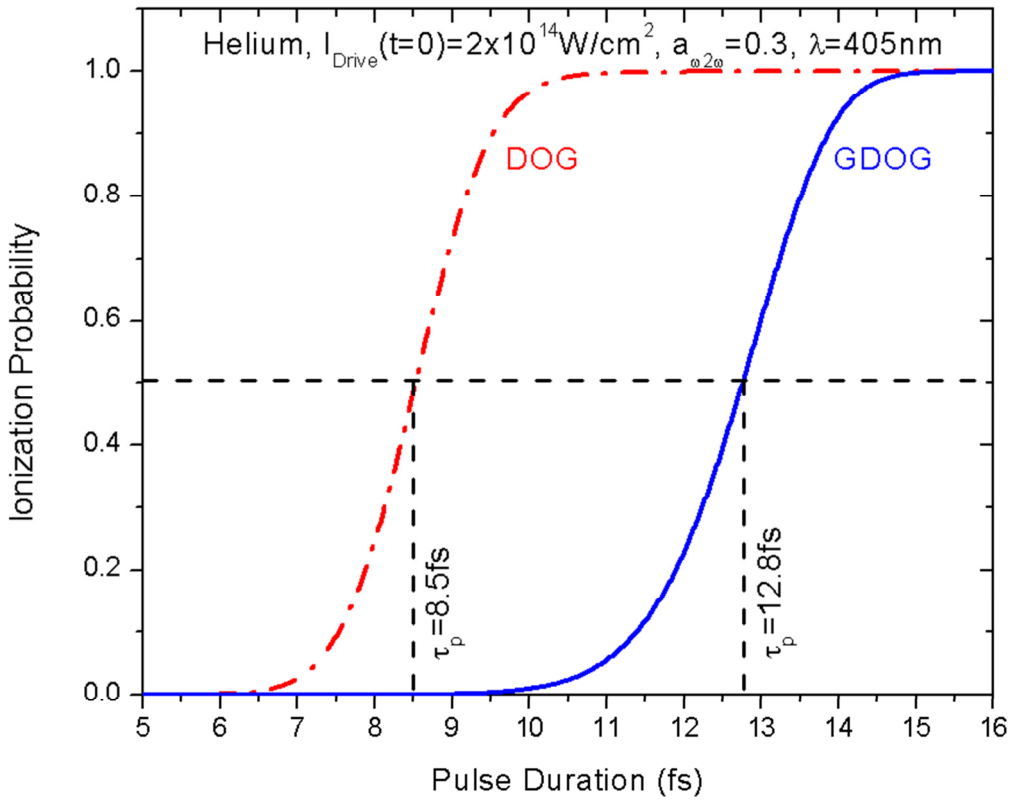

Figure 6-2 Ionization probability as a function of pulse duration calculated using the ADK model for DOG and GDOG driven by blue pulses in helium.

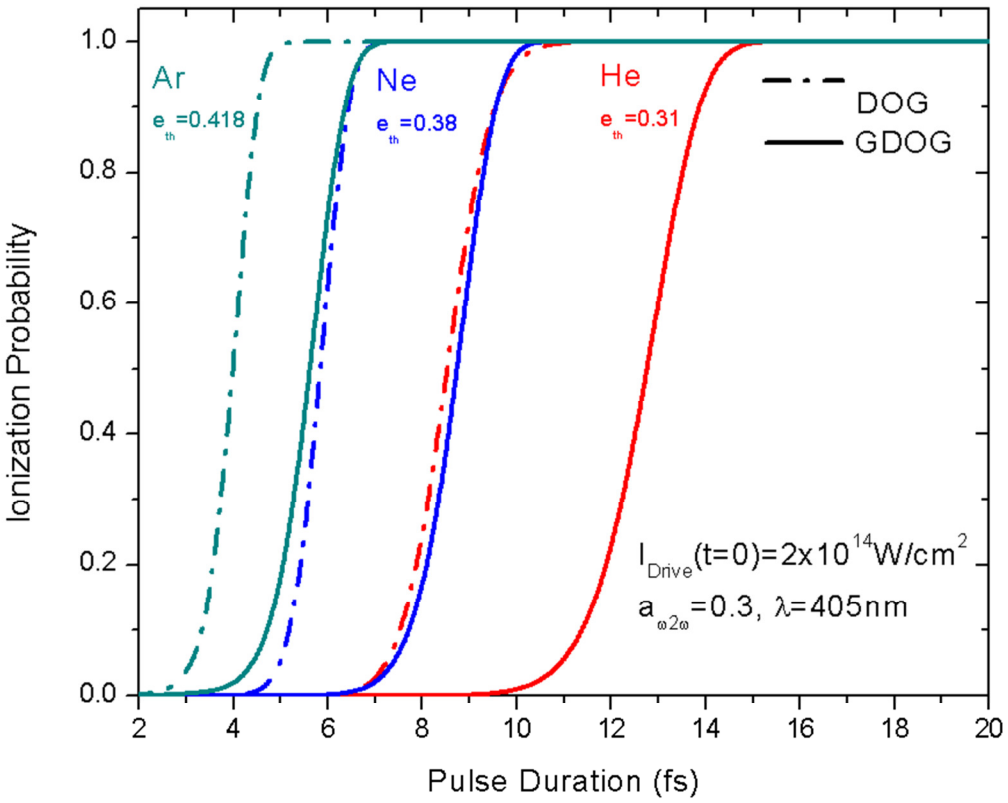

Figure 6-3 Ionization probability as a function of pulse duration calculated using the ADK model for DOG and GDOG in argon, neon and helium driven by blue pulses.

Sub-10 fs pulses have been demonstrated but with low pulse energy, and we discussed our efforts to scale it up in Chapter 5. However, it still appears to be a major technical road block towards gating. Additionally, to the best of our knowledge, no suitable non-linear crystal is available to generate weak second harmonic (200 nm) from a 400 nm fundamental and poses a bigger challenge to achieving our goal.

GDOG using blue main pulse and red weak pulse

To address the second harmonic issue, we propose to use a weak 800 nm pulse spatially and temporally overlapped to break the symmetry of the 400 nm fundamental pulse to make the two color field, which we term blue GDOG. In Figure 6-4, we show the electric field from the addition of the 400 nm electric field with 25, 50, 75 and 100% 800 nm electric field. Symmetry appears to be breaking, but it can be seen that a peak maximum is present every two optical cycles, which hints at the generation of single attosecond pulse with a gate width as large as two optical cycles.

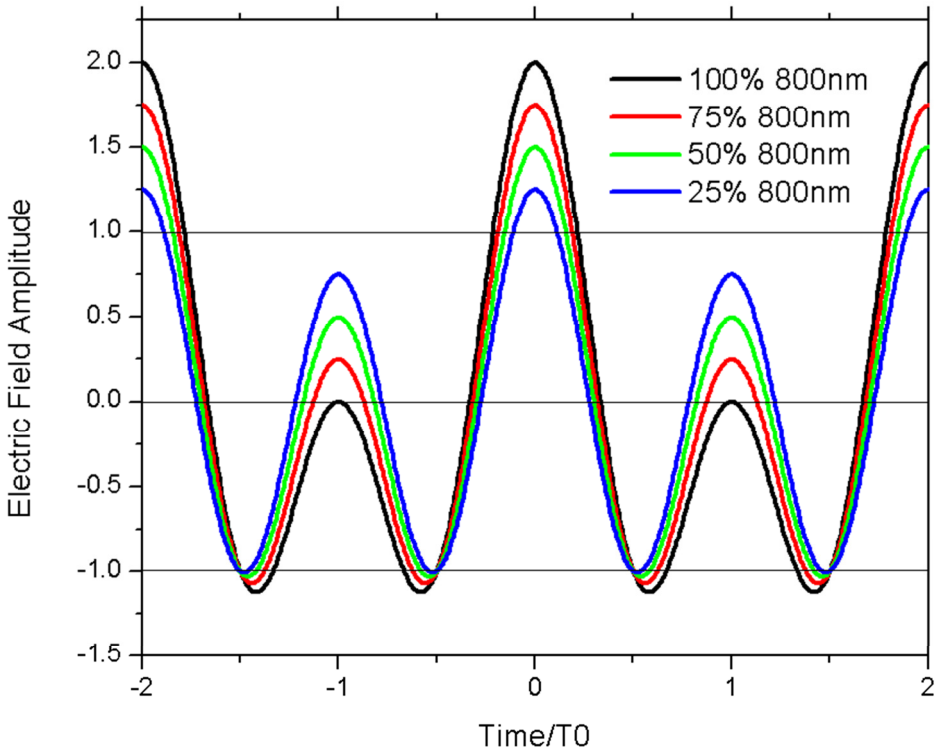

Figure 6-4 Two-color electric field made by adding red in blue. The fraction of red is indicated in the legend.

In Figure 6-5, we present delay T_d as a function of pulse duration with one and two optical cycle gate widths for the GDOG case. Two major advantages can be seen here. First, with a two optical cycle gate width the delay T_d is reduced by half leading to higher intensity within the gate, relaxing the requirement on pulse energy. Second, we estimate based on the ADK model that pulses as long as 10 fs can be used for GDOG without depletion. Thus, our blue GDOG, solves the roadblock of a 400/200 nm non-linear crystal and additionally relaxes the requirement on pulse duration and pulse energy.

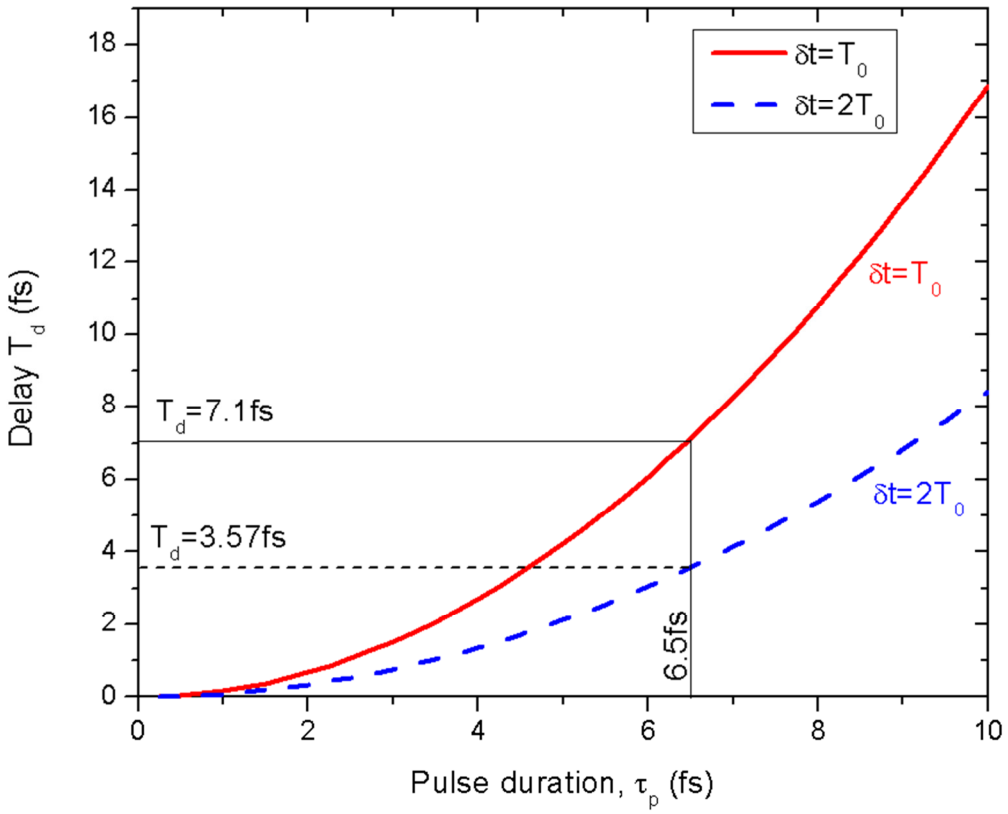

Figure 6-5 Delay between right and left circularly polarized pulses as a function of pulse duration in GDOG driven by blue for one and two cycle gate width.

Brewster window and spatial overlap

To spatially overlap 800 nm pulses with 400 nm pulses, we propose to combine 800 nm with 400 nm on the Brewster window in the GDOG setup (GDOG setup is given in Figure 2-6 in Chapter 2). In Figure 6-6, we illustrate our proposed scheme. 74.65% of the driving part of blue pulses is transmitted through the Brewster window, while the gating part sees 100% transmission and red pulses see 13.5% reflection from the window and spatially become collinear with the blue driving and gating pulses. The remaining portion of red pulses from second harmonic generation in the BBO can be used for this purpose. Experimentally, 4.7 mJ of red pulses produces 1 mJ of blue and 1.2 mJ (SHG with pump depletion) red pulses are recovered after the first dichroic mirror leading to 162 μJ of red pulses after 13.5% reflection from the brewster window, which is comparable to the blue pulse energy.

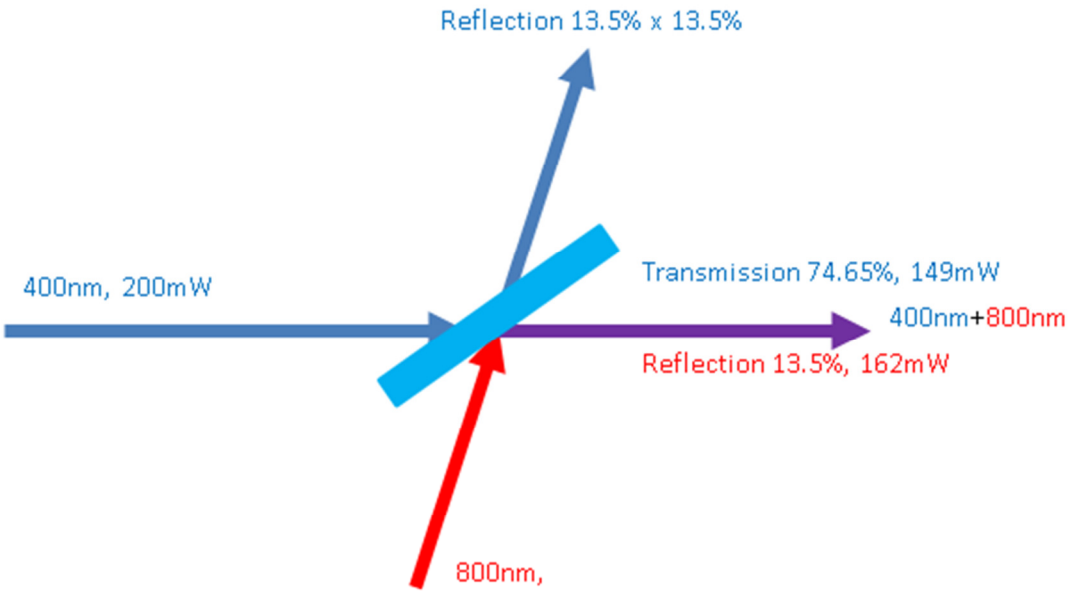

Figure 6-6 Two color field made by adding red in blue by reflecting from the brewster window.

In Figure 6-7 (a) and (b) we present the reflectivity from a fused silica surface as a function of incidence angle for 800 and 400 nm pulses, respectively. Total transmission from both surfaces of a brewster window for 400 nm pulses is given in Figure 6-8, and to summarize, we give incidence and refraction angles with transmission from both surfaces in Table 1. The brewster window is set at 55.78^{o}, with total 400 nm transmission of 74.65% from both surfaces and 800 nm reflection of 13.5% from the 2nd surface.

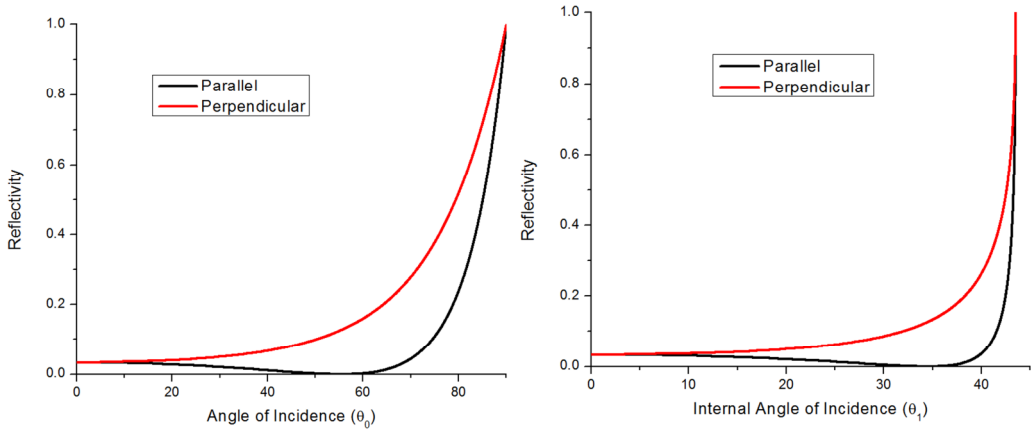

Figure 6-7 Reflectivity as a function of incidence angle for red (a) and blue (b) pulses for both polarizations.

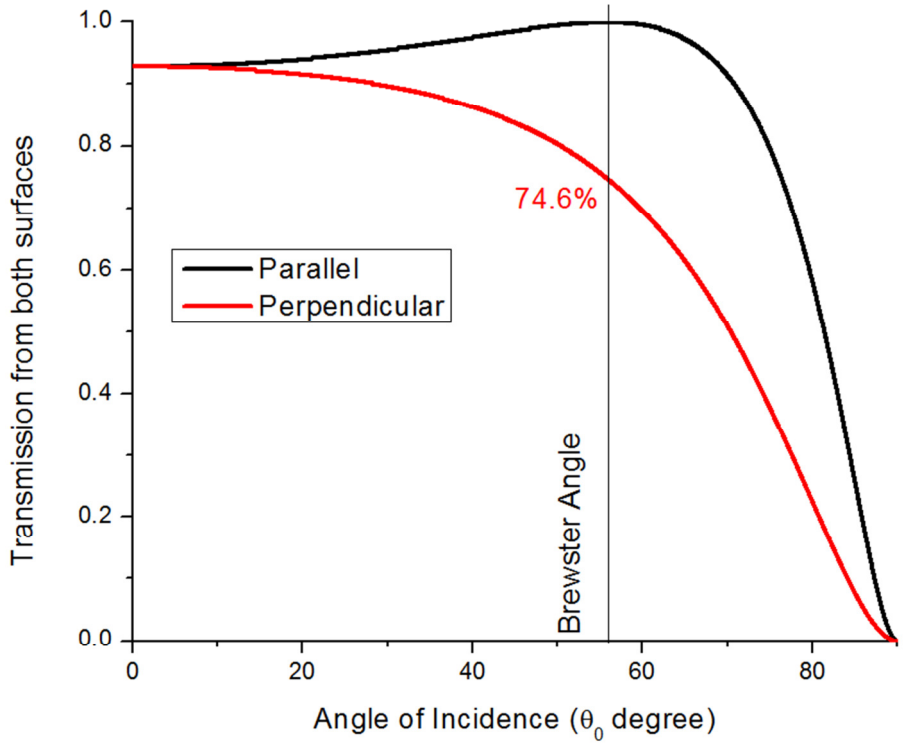

Figure 6-8 Total transmission of blue as a function of incidence angle from both surfaces, driving field has parallel polarization while gating field has perpendicular.

Table 6-1 Transmission of 800 and 400 nm from Brewster window.

	800 nm	**400 nm**
Surface 1		
Angle of Incidence	55.47°	55.78°
Angle of Refraction	34.53°	34.23°
Transmission	87.23%	86.50%
Surface 2		
Angle of Incidence	34.53°	34.23°
Angle of Refraction	55.47°	55.78°
Transmission	87.23%	86.50%
Total Transmission	76.1%	74.65%

High harmonics from two-color field

In Figure 6-9, we present the experimental setup to produce high harmonics from the linear two color field constructed by temporal and spatial overlap of long blue and red pulses, while the high-harmonic setup is given in Figure 4-11 of Chapter 4. S-polarized blue pulses are produced by second harmonic generation in 0.3 mm BBO and separated from leftover red pulses (p-polarized) by reflection from a dichroic mirror. The polarization of the red pulses is rotated to s-polarized by a zero order half wave plate, temporally overlapped with blue pulses by a moveable delay line, and spatially combined with blue pulses reflected from the brewster window. At the brewster window, both blue and red pulses are s-polarized.

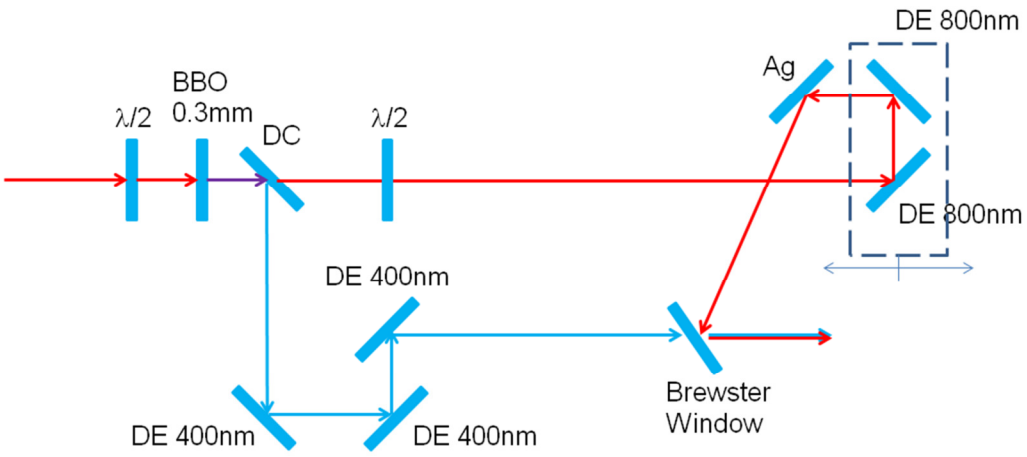

Figure 6-9 Experimental setup to generate two-color field made by adding weak red in blue to break its symmetry.

The high harmonic spectra produced from red only, blue only and both is presented in Figure 6-10 (a), (b) and (c), respectively. It is evident that the red pulses do not have enough intensity at the gas cell to produce high-harmonics, yet blue pulses do have enough intensity to produce harmonics (Remember blue driving pulses have two orders of magnitude higher conversion efficiency than red pulses). Coarse temporal overlap is obtained by inserting a 0.1 mm BBO after the brewster window producing blue pulses from red by SHG. The delay stage is scanned to get fringes between the transmitted blue pulses and the blue pulses produced from red. For fine overlap, high harmonics are produced from blue pulses and then the delay is scanned on the red pulses delay stage until odd harmonics of 800 nm are optimized. The odd harmonics of 800 nm are not produced from the red pulses as evident from Figure 6-10(a) but are

produced due to symmetry breaking of blue pulses. The 8th harmonic of 400 nm appears weaker than 800 nm odd harmonics due to the fact that the addition of weak red in blue is more complicated than addition of weak blue in red, as seen in Figure 6-4. We present harmonics from the two color field with different ratios of blue and red in Figure 6-11, and summarize the results in Figure 6-12 by plotting the fraction of 8th harmonic of 400 nm and 15th and 17th harmonics of 800 nm with respect to the 7th harmonic of 400 nm. It can be seen that red as low as 5% added to the blue is enough to break the symmetry. Additionally, the yield of harmonics due to symmetry breaking increases with 400/800 ratio up to 50%, and afterwards a saturation effect is seen. Based on these results we propose to add 50% or less red in blue to give the two color effect.

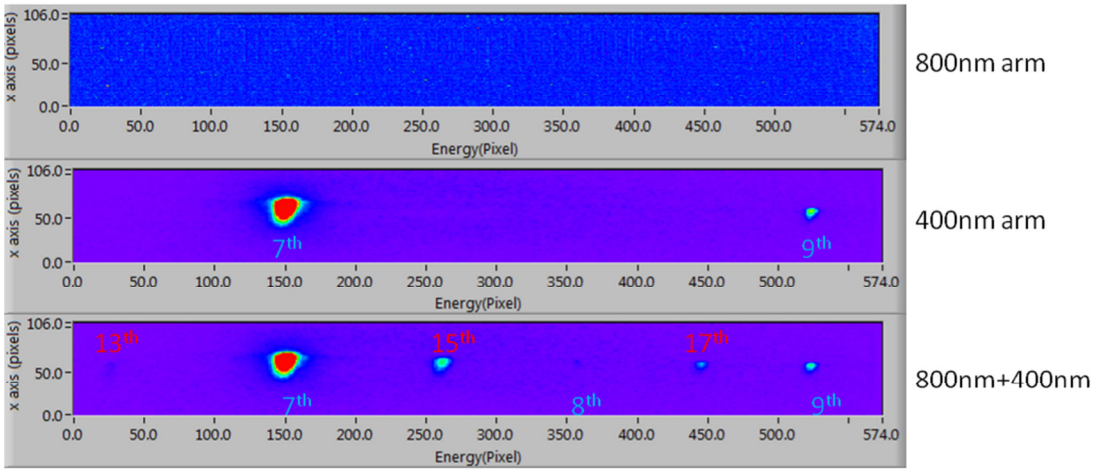

Figure 6-10 High harmonic spectra generated from 800 nm arm (a), 400 nm arm (b) and with both arms (c).

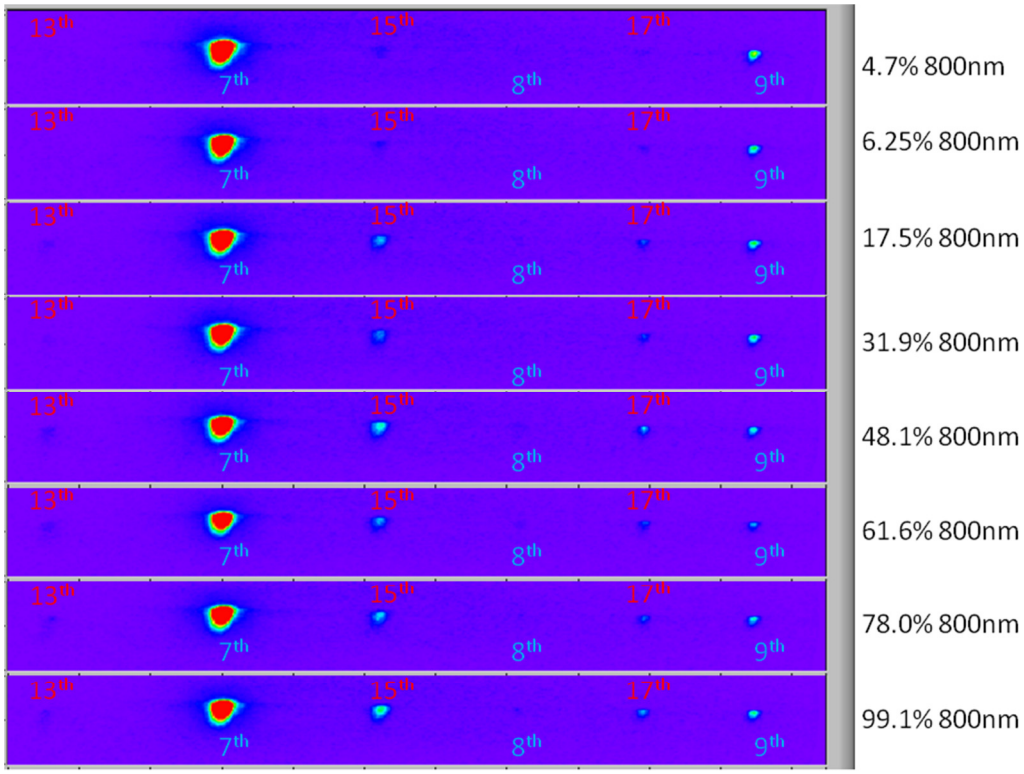

Figure 6-11 High harmonics for different fractions of red added into blue.

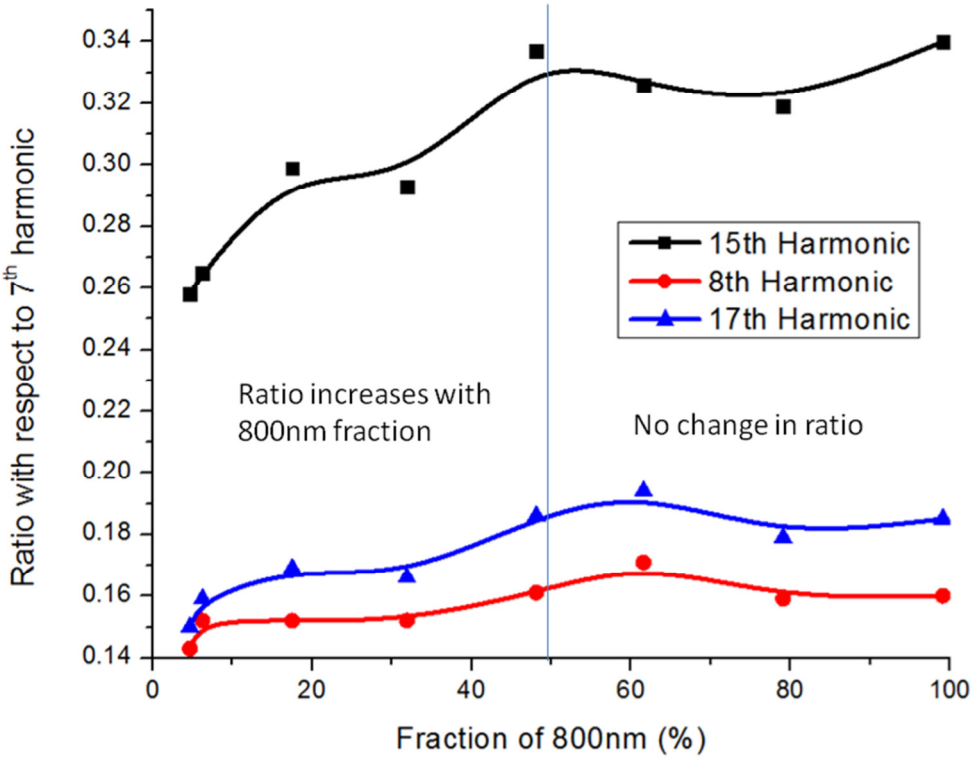

Figure 6-12 Yield of 8th harmonic from blue and 15th and 17th harmonics of red as a function of red fraction in blue.

Stabilization of temporal overlap between blue and red

Experimentally, to implement blue GDOG a neon filled hollow core fiber and chirp mirrors are needed to be inserted in the blue arm in the experimental setup in Figure 6-9. To stabilize temporal overlap between blue and red we proposed an interferometric setup given in Figure 6-13. The reflected blue pulses and transmitted red pulses from the BBO are separated by a dichroic mirror forming a Mach-Zehnder interferometer. The red pulses are frequency doubled into blue by a 0.1mm BBO and recombined by a D-shaped mirror. Once fine temporal overlap between red and blue is obtained in the setup in Figure 6-9, based on symmetry breaking in high harmonics, the delay in the Mach-Zehnder interferometer is adjusted to obtain fringes after the D-shaped mirror. This compensates for the delay between red and blue introduced by a number of optical elements in the setup. The fringes are imaged on a photodiode through a slit and a feedback signal is generated. A control signal is calculated from the feedback signal by a PID controller and fed to the PZT in the delay stage to control the delay of the red arm in the setup in Figure 6-9.

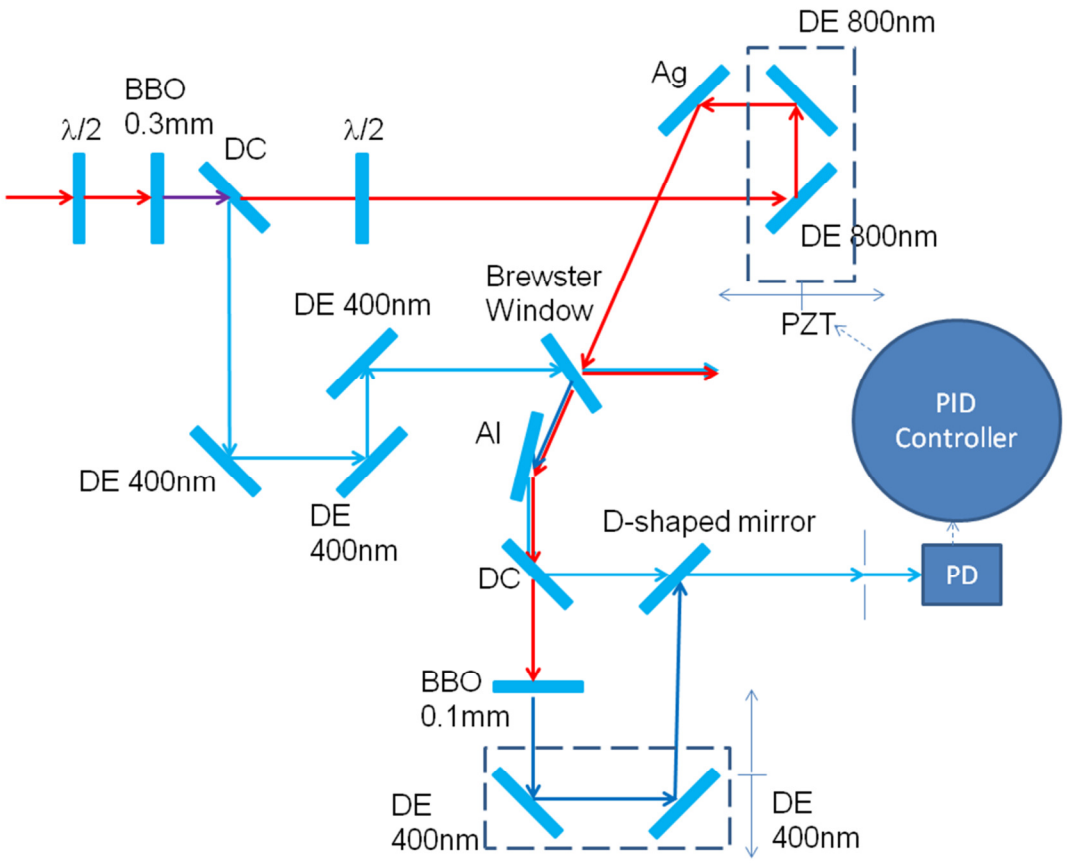

Figure 6-13 Interferometric setup to stabilize temporal overlap between red and blue.

References

[1] M. V. Ammosov, N. B. Delone and V. P. Krainov, "Tunnel ionization of complex atoms and of atomic ions in an alternating electromagnetic field", Sov. Phys. JETP 64, 1191-1196 (1986).

[2] S. D. Khan, Y. Cheng, M. Möller, K. Zhao, B. Zhao, M. Chini, G. G. Paulus and Z. Chang, "Ellipticity dependence of 400 nm-driven high harmonic generation", App. Phys. Lett., 99, 161106 (2011).

Chapter 7 - Conclusion and outlook

In this work I have focused on two areas, firstly to generate and measure short single attosecond pulses and secondly to scale up the photon flux of the attosecond pulses to increase their intensity.

We have developed an attosecond streak camera to measure single attosecond pulses. The shortest pulse we have measured is 107.5 as, which is close to the bandwidth of the Mo/Si mirror, the main bottleneck. To improve this, we have already developed another setup at the University of Central Florida (UCF) using a gold mirror at glancing incidence instead of a Mo/Si mirror at normal incidence and have also improved the resolution of the time-of-flight detector by switching to a magnetic bottle design. With this new setup our group was able to demonstrate 77 as pulses which ties the current world record of 80 as. Additionally, to retrieve attosecond pulses from a spectrogram obtained from the attosecond streak camera, we have developed FROG-CRAB and later the PROOF algorithms. We have demonstrated theoretically that PROOF can characterize attosecond pulses as short as 1 atomic unit (24.2 as), which is currently state-of-the-art.

In an effort to generate single attosecond pulses from high power lasers, which are usually without CE-phase lock, we have demonstrated that short single attosecond pulses can be produced from multi-cycle lasers using GDOG with a narrow gate width without locking the CE-phase. To extend this, our team is developing a 100-200 mJ 10 Hz laser at UCF and plans to generate micro-joule level single attosecond pulses in the coming days and study electron dynamics using attosecond pump-attosecond probe experiments.

In another effort to scale up the photon flux of attosecond pulses, we have generated a ~9.5 times more intense attosecond pulse train using laser ablated carbon plasma instead of argon and have also demonstrated continuum generation from such plasmas by using DOG. This hints at the extraction of a single attosecond pulse, but the attosecond streak camera could not be used to measure pulse duration as the harmonics were only stable for a few minutes, and it typically takes several hours for one streaking trace.

Furthermore, in yet another effort to scale up photon flux, we switched the driving laser wavelength from red (800 nm) to blue (400 nm) and demonstrated 2 orders of magnitude enhancement in the photon flux of attosecond pulse trains. In an attempt to design an optical

gating for blue driving lasers, we made the first experimental measurement of ellipticity dependence of blue driving pulses in argon, neon and helium. Based on the ellipticity dependence, we propose to use GDOG to extract single attosecond pulses. Generation of intense (>200 μJ) and short (<10 fs) blue pulses and the lack of a non-linear crystal to frequency double 400 nm into 200 nm were two major roadblocks towards the implementation of optical gating. We demonstrated ~250 μJ (highest energy from 400nm hollow core fiber) short blue pulses by self-phase modulation in a neon filled hollow fiber and chirp mirrors and characterized them with a home-made self-diffraction FROG. The bandwidth can support <7 fs pulses, however, phase compensation with chirp mirrors is still a technical challenge and a major hurdle. For the second issue, we propose a new gating technique termed blue GDOG in which weak red pulses are added into short blue pulses to break the symmetry. Currently, the only hurdle to generate single attosecond pulses from blue pulses is phase compensation of short blue pulses after the hollow core fiber. Additionally, we produced pulse trains with a blue driving laser in laser ablated carbon plasmas and the harmonics were stable over longer periods of time. However, conversion efficiency was comparable to that of argon driven by blue pulses.

We plan to continue work on blue GDOG at UCF and try it using a 100-200 mJ 10 Hz laser, demonstrating non-linear attosecond science by two photon ionization of helium (I_p=24.587 eV). We propose to use a diamond or ion beam sputtered silicon carbide mirror with an indium or tin filter to remove the spectrum after 24.587 eV to prevent single photon ionization. We estimate that at least 10 nJ attosecond photon flux is required to carry out such an experiment. Currently, with red driving pulses the highest photon flux is ~1 nJ in our attosecond streak camera, while the highest reported flux is 2.6 nJ by the Italian group. Fullerene (C_{60}) is also a promising candidate for a two photon ionization experiment due to surface plasmon resonance. However more synchrotron experiments are needed to measure one and two photon cross-section of fullerene. At the same time, our collaborators at ALLS, INRS are trying to extend conversion efficiency from carbon plasmas driven by blue pulses based on the results we obtained during this work.

In a nutshell, we developed an attosecond streak camera to characterize single attosecond pulses generated by DOG and GDOG, software algorithms to process these streaking traces and pursued several directions to scale up attosecond photon flux. Based on these findings, several experiments are in mature stages with higher power lasers at UCF and ALLS, INRS.

Publications

1. Steve Gilbertson, Hiroki Mashiko, Chengquan Li, **Sabih D. Khan**, Mahendra M. Shakya, Eric Moon, and Zenghu Chang, "A low-loss, robust setup for double optical gating of high harmonic generation", Appl. Phys. Lett. **92**, 071109 (2008).
2. Hiroki Mashiko, Steve Gilbertson, Chengquan Li, **Sabih D. Khan**, Mahendra M. Shakya, Eric Moon, and Zenghu Chang, "Double Optical Gating of High-Order Harmonic Generation with Carrier-Envelope Phase Stabilized Lasers", Phys. Rev. Lett. **100**, 103906 (2008).
3. Steve Gilbertson, Ximao Feng, **Sabih Khan**, Michael Chini, He Wang, Hiroki Mashiko, and Zenghu Chang, "Direct measurement of an electric field in femtosecond Bessel-Gaussian beams", Optics Letters, **34**, 16, 2390 (2009).
4. Mashiko H, Gilbertson S, Chini M, Feng X, Yun C, Wang H, **Khan Sabih D,** Chen S, Chang Z., "Extreme ultraviolet supercontinua supporting pulse durations of less than one atomic unit of time", Opt Lett., **34**, 21, 3337 (2009).
5. Ximao Feng, Steve Gilbertson, Hiroki Mashiko, He Wang, **Sabih D. Khan**, Michael Chini, Yi Wu, Kun Zhao, and Zenghu Chang, "Generation of Isolated Attosecond Pulses with 20 to 28 Femtosecond Lasers", Phys. Rev. Lett. **103**, 183901 (2009).
6. He Wang, Michael Chini, **Sabih D Khan**, Shouyuan Chen, Steve Gilbertson, Ximao Feng, Hiroki Mashiko and Zenghu Chang, "Practical issues of retrieving isolated attosecond pulses", J. Phys. B: At. Mol. Opt. Phys., **42**, 134007 (2009).
7. Michael Chini, He Wang, **Sabih D. Khan**, Shouyuan Chen, and Zenghu Chang, "Retrieval of satellite pulses of single isolated attosecond pulses", Appl. Phys. Lett. **94**, 161112 (2009).
8. Feng X, Gilbertson S, **Khan Sabih D**, Chini M, Wu Y, Carnes K, Chang Z., "Calibration of electron spectrometer resolution in attosecond streak camera", Opt Express., **18**, 2, 1316 (2010).
9. Michael Chini, Steve Gilbertson, **Sabih D. Khan**, and Zenghu Chang, "Characterizing ultrabroadband attosecond lasers", Optics Express, **18**, 12, 13006 (2010).

10. Steve Gilbertson, Michael Chini, Ximao Feng, **Sabih Khan**, Yi Wu, and Zenghu Chang, "Monitoring and Controlling the Electron Dynamics in Helium with Isolated Attosecond Pulses", Phys. Rev. Lett. **105**, 263003 (2010).
11. Steve Gilbertson, Yi Wu, **Sabih D. Khan**, Michael Chini, Kun Zhao, Ximao Feng, and Zenghu Chang, "Isolated attosecond pulse generation using multicycle pulses directly from a laser amplifier", Phys. Rev. A **81**, 043810 (2010).
12. **Sabih D. Khan**, Yan Cheng, Max Möller, Kun Zhao, Baozhen Zhao, Michael Chini, Gerhard. G. Paulus, and Zenghu Chang, "Ellipticity dependence of 400 nm-driven high harmonic generation", Appl. Phys. Lett. **99**, 161106 (2011).
13. Max Möller, **Sabih. D. Khan**, Yan Cheng, Baozhen Zhao, Kun Zhao, Michael Chini, Gerhard G. Paulus and Zenghu Chang, "Dependence of high harmonic generation yield on driving-laser ellipticity", Phys. Rev. A (submitted).
14. Yoann Pertot, Shouyuan Chen, **Sabih D. Khan**, Luc Bertrand Elouga Bom, Tsuneyuki Ozaki and Zenghu Chang, "Generation of Continuum High-Order Harmonics from Carbon Plasma using Double Optical Gating", J. Phys. B (accepted).

Conference Talks and Proccedings

1. **Sabih D. Khan**, Michael Chini, Steve Gilbertson, and Zenghu Chang, "Characterization of Isolated Attosecond Pulses with Ultrabroad Bandwidth", Proceeding of the International Conference on Ultrafast Phenomena, ME26 (2010).
2. **Sabih D. Khan**, He Wang, Ximao Feng, Michael Chini, and Zenghu Chang, "Practical Issues of Retrieving Isolated Attosecond Pulse from CRAB", Procedings of CLEO/QELS, Pulse Measurement II, CThDD (2009).
3. **Khan, Sabih D**; Cheng, Yan; Zhao, Kun; Chini, Michael; Zhao, Baozhen; Chang, Zenghu, "Ellipticity dependence of high harmonics from 400 nm driving pulses", Proceedings of CLEO/QELS, JWA88 (2011).
4. Mashiko, Hiroki; Gilbertson, Steve; Li, Chengquan; **Khan, Sabih**; Shakya, Mahendra; Moon, Eric; Chang, Zenghu, "Double Optical Gating of High Harmonic Generation", Proceedings of CLEO/QELS, CTuO3 (2008).

5. Gilbertson, Steve; Feng, Ximao; Mashiko, Hiroki; Wang, He; **Khan, Sabih**; Chini, Michael; Chang, Zenghu, "Characterization of Isolated Attosecond Pulses from Multi-Cycle Lasers", Proceedings of CLEO/QELS, JThB3 (2009).
6. Zhao, Kun; Zhang, Qi; Gilbertson, Steve; Chini, Michael; **Khan, Sabih**; Chang, Zenghu, "Magnetic-Bottle Electron Spectrometer for Measuring Isolated 25 as Pulses", Proceedings of Laser Science (LS), LWK2 (2010).
7. Chini, Michael; Gilbertson, Steve; **Khan, Sabih D**; Chang, Zenghu, "Characterizing isolated atomic unit attosecond pulses", Proceedings of CLEO/QELS, JThB43 (2011).
8. Chini, Michael; Gilbertson, Steve; **Khan, Sabih D**; Chang, Zenghu, "Characterizing isolated atomic unit attosecond pulses", Proceedings of CLEO/QELS, JThB43 (2011).
9. Wu, Yi; Khan, **Sabih D**; Gilbertson, Steve; Chini, Michael; Chang, Zenghu, "Single attosecond pulse generation using GDOG without the need to stabilize Carrier-Envelope phase", Proceedings of CLEO/QELS, QMC2 (2011).
10. Zhang, Qi; Zhao, Kun; Chini, Michael; Gilbertson, Steve; **Khan, Sabih D**; Chang, Zenghu, "Characterization of isolated 80 as XUV Pulses with PROOF", Proceedings of CLEO/QELS, QMC3 (2011).
11. Pertot, Yoann; Elouga Bom, Luc; Chen, Shouyuan; **Khan, Sabih D**; Chang, Zenghu; Ozaki, Tsuneyuki, "Direct comparison of high-order harmonics generated in gas and in carbon plasma", Proceedings of CLEO/QELS, QThI5 (2011).
12. Gilbertson, Steve; Feng, Ximao; **Khan, Sabih**; Chini, Michael; Wang, He; Chang, Zenghu, "Probing Laser Disturbed Doubly Excited States with Isolated Attosecond Pulses", Proceedings of CLEO/QELS, IPDA8 (2009).
13. Gilbertson, Steve; Feng, Ximao; Mashiko, Hiroki; Wang, He; **Khan, Sabih**; Chini, Michael; Chang, Zenghu, "Characterization of Isolated Attosecond Pulses from Multi-Cycle Lasers", Proceedings of CLEO/QELS, JThB3 (2009).
14. Wu, Yi; Gilbertson, Steve; **Khan, Sabih**; Chini, Michael; Zhao, Kun; Feng, Ximao; Chang, Zenghu,"Isolated Attosecond Pulses Generated Directly from Femtosecond Chirped Pulse Amplifier", Proceedings of CLEO/QELS, JThA1 (2010).
15. Gilbertson, Steve; Chini, Michael; **Khan, Sabih**; Wu, Yi; Feng, Ximao; Chang, Zenghu, "Control of Electron Dynamics of Doubly Excited States from Isolated Attosecond Pulses", Proceedings of CLEO/QELS, JThA5, (2010).

Book Chapters

1. Shouyuan Chen, Steve Gilbertson, He Wang, Michael Chini, Kun Zhao, **Sabih Khan**, Yi Wu, and Zenghu Chang, Chapter 4, Attosecond Pulse Generation, Characterization and Application, ADVANCES IN MULTI-PHOTON PROCESSES AND SPECTROSCOPY
2. Ximao Feng, Steve Gilbertson, Hiroki Mashiko, **Sabih Khan**, He Wang, Michael Chini, Yi Wu, and Zenghu Chang, Chapter5, Single Isolated Attosecond Pulses Generation with Double Optical Gating, Progress in Ultrafast Intense Laser Science VI